Numerical simulation of the impact of unsteady flows around impervious buildings

Master's Thesis

Anna Louka

Date of submission 2022

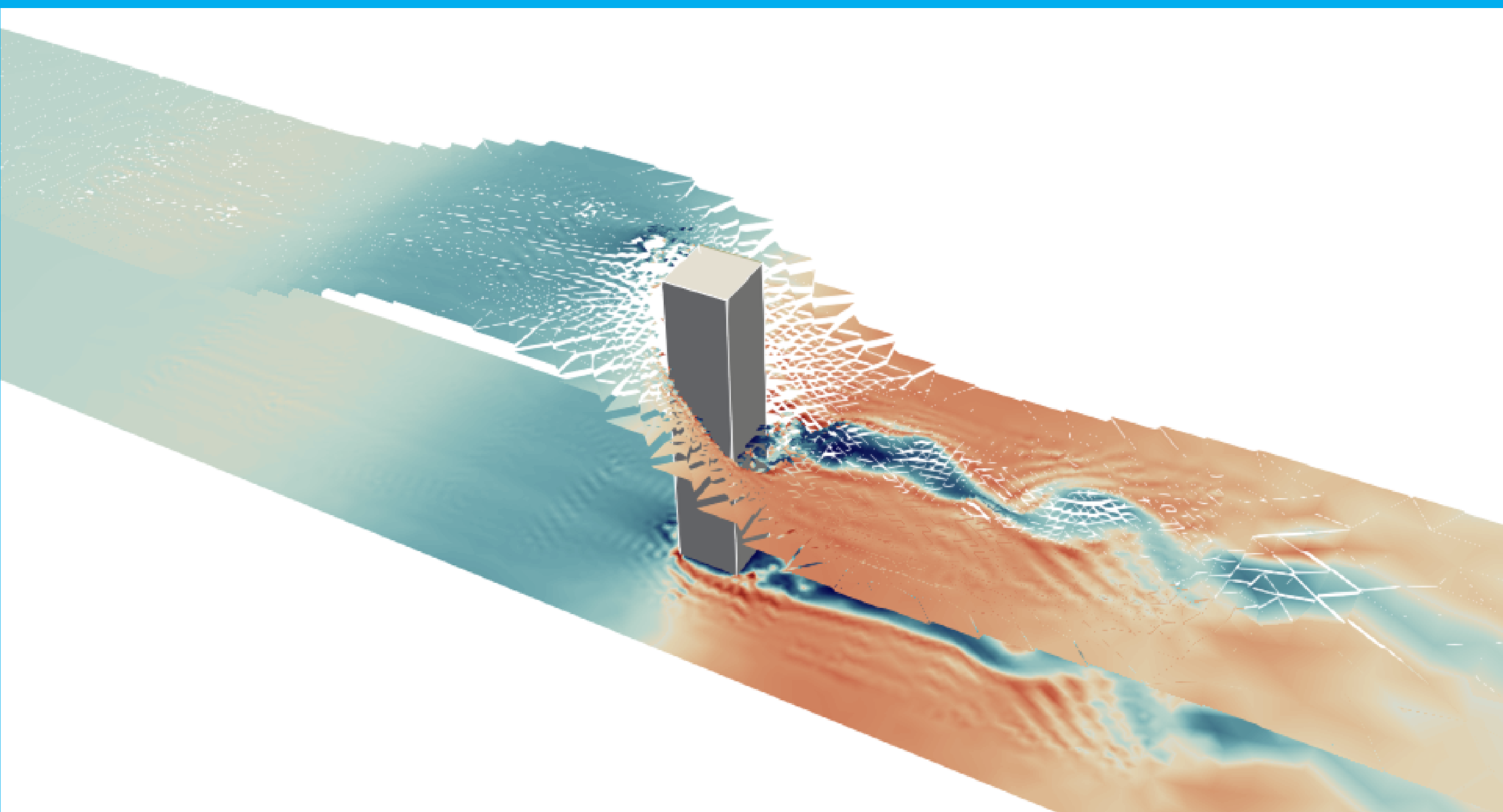

Numerical simulation of the impact of unsteady flows around impervious buildings

Master's Thesis

by

Anna Louka

student number: 5163188

Master thesis submitted to Delft University of Technology

in partial fulfilment of the requirements for the degree of

MASTER OF SCIENCE

in **Hydraulic Engineering**

Faculty of Technology, Policy and Management

To be defended in public on September 2022

Graduation Committee

Chairperson:	Dr. ir. D. Wüthrich,	TU Delft
First supervisor:	Dr. ir. O. J. Colomés Gené,	TU Delft
Second supervisor:	Ir. C. Ylla Arbos,	TU Delft

TU Delft

Preface

This thesis was written as the final step of my Master of Science degree in Hydraulic Engineering at the Delft University of Technology. At this point, I would like to express my gratitude to all the people that helped me, advised me, and supported me.

First and foremost, I am greatly indebted to my committee members: Dr. Ir. Davide Wüthrich, Dr. Ir. Oriol J. Colomés Gené, and C. Ylla Arbos, for their guidance and their patience, during the whole period I was working on this project. This endeavor would not have been possible without their contribution. Especially, I would like to express my appreciation to my chair professor Dr. Davide Wüthrich, not only for his constructive suggestions and encouragement but also for introducing me to the topic of unsteady flows around structures. It was a great opportunity for me to deal with such a challenging topic that is at the heart of current affairs and meets my scientific interests. Secondly, I am also thankful to Dr. Oriol J. Colomés Gené for all the knowledge and motivation that he provided me during these months, especially for the programming skills I acquired from my thesis project. I started without coding background, and due to his guidance, I managed to accomplish successfully the scope of my thesis. Thirdly, I am also thankful for C. Ylla Arbos completing a round team to pursue this research.

I would like to finish this acknowledgment by giving a special shout-out to my family and friends for their support, encouragement, and unconditional love they have shown me in every difficulty I faced and in every effort I made throughout these years. They were fellow travelers on my educational journey, a journey which changed my way of thinking, not only as an engineer but also as a person, through the experiences and knowledge that provided me.

Anna Louka
Delft, July 2022

Abstract

In the last few years, the climate crisis has been accelerating at a dizzying pace and poses an emergency threat to our planet. Rainfalls have transformed into intense downpours, and flash flooding, combined with the sea level rise, leads to a higher risk of inundation of densely populated coastal cities. Moreover, the melting of the permafrost can lead to significant landslides, triggering the generation of mega-tsunami waves. The latter can have a catastrophic impact, not only on the infrastructure but also on human life. Man-induced climate change is responsible for the increase in frequency and intensity of extreme natural events, such as tsunamis, floods, and storm surges. Recent research indicates that almost one-fourth of the world population lives at high-risk locations to at least 0.15m of inundation depths with a return period of 1 in 100 years. Therefore, the urge of implementing protection measures against unsteady flows is imperative.

Undoubtedly, the involvement of engineers can play a pivotal role in order to analyze these flows in the built environment and provide sufficient coastal and building plans to ensure safety and reduce reconstruction costs. The behavior of the unsteady flow around a structure is not a well-understood topic and results in a lack of accuracy and reliability. More insights are required into the fluid-structure interactions to come up with a safe building design.

In the present study, unsteady flows are generated using the dam-break technique in line with previous research. The Thesis aims to model, validate, and implement a simplified approach to analyze the complexity of the hydrodynamic behavior of unsteady flows around impervious buildings, with different orientations and blockage ratios. To do so, the research introduces a numerical simulation method of a dam-break wave, using the two-dimensional, and non-rotational shallow water equations. The Galerkin finite-element model is applied for the discretization of the solution on a limited domain.

Initially, the flow of the dam-break wave was validated in the absence of the structure, using a dam-break experimental work for comparison. Then, in order to insert a structure in the domain, a second experiment with a structure is used, which generates tsunami-like waves using the vertical release technique. The gate, which represents the dam, is located at x=0 and opens instantaneously at t=0s. Behind the gate, the reservoir maintains an amount of water that flows, after the opening of the gate, into the channel generating the shock wave. At the channel downstream of the gate, initial water levels are considered and the behavior of a bore propagation is simulated. The building is located on the downstream side and different impervious building configurations were studied in terms of orientation and shape to investigate the impact of the unsteady flow. To analyze the complex hydrodynamic processes of flooding, four fixed points around the structure are set to measure the action of the bore on different impervious building configurations. The water elevations and the averaged velocity profiles in time were derived at each point. Moreover, the horizontal forces in the x and y directions are calculated by the model, integrating the stresses over the wet surface of the buildings.

The general behavior of the fluid-structure interactions is captured well, especially upstream of the building, and insights are gained regarding the behavior of the fluid around the structure and the parameters of influence. Results showed that orientation changes completely the impact on the building configurations. The separation of the flow and the blockage ratio are the main parameters that are influenced by the angle of rotation and change the behavior of the loading process at the initial impulsive phase, when the wave arrives at the structure, and at the hydrodynamic phase, where the flow has a quasi-steady behavior. Overall, a good agreement is achieved with the experimental data, although the numerical model overestimates the loads acting on the different building configurations. Results proved that the orientation of the building with respect to the flow facilitates the flow around the structure and contributes to lower water levels, and to a better distribution of the horizontal loads on the surface. The best results were achieved for an angle of rotation of 45°, where symmetrical separation of the flow is also playing an important role.

Contents

List of Figures

List of Tables

List of Abbreviations

$1D$	One-dimensional
$1DSV$	One-Dimensional Saint-Venant model
$2D$	Two-dimensional
$3D$	Three-dimensional
$ASCE$	American Society of Civil Engineers
BC	Boundary conditions
CFD	Computational Fluid Dynamics
DG	Discontinuous Galerkin
DNS	Direct Numerical Simulation
$EPFL$	Ecole Polytechnique Fédérale de Lausanne
FEM	Finite element method
FVM	Finite-volume method
FSI	Fluid structure interactions
$IPCC$	Intergovernmental Panel on Climate Change
LES	Large eddy simulation
LHS	Left-hand-side
$RANSE$	Reynolds-averaged Navier-Stokes equations
RHS	Right-hand-side
SI	International System of units
SLR	Sea level rise
SPH	Smoothed Particles Hydrodynamics
SWE	Shallow water equations
TU	Technical university
$V\&V$	Verification and Validation

List of Symbols

Γ_s	The boundary of the latteral side-walls of the domain
Γ_w	The boundary of the building's walls in the domain
Γ_{out}	The outflow boundary
Q	The discharge
u	The velocity in x direction
v	The velocity in y direction
U	The depth-averaged velocity in x direction
V	The depth-averaged velocity in y direction
$u(x,y,t)$	The depth-averaged velocity field
u_c	The wave front celerity
$\parallel u \parallel$	Euclidean norm
t	time
dt	Time step
T	Duration
h	the water depth
d_0	Initial impoundment water depth at the reservoir
h_0	Initial water depth at the channel downstream of the gate-dam
$h_p = h(x,y,t)$	The free surface perturbation
H	Free surface perturbation
$\overline{h}$	Free surface as the sum of the mean free surface depth and the free surface perturbation
$h_{aver.}$	Averaged water depth
R	Hydraulic gradient
Re	Reynolds number
c_f	friction coefficient
ν_t	kinematic viscosity
n	The Manning's coefficient
$\vec{n}$	The outward-oriented unit normal vector
τ_s	The friction stress at the surface per unit mass
τ_b	The bottom shear stress per unit mass
p_α	The atmospheric pressure field at the air-water interface
C_D	The drag coefficient between free-surface and air
C	The Chezy coefficient
W_x, W_y	The velocities of the air in the x and y directions respectively
$\vec{T}$	The eddy viscosity term
$\mathbb{1}$	The identity tensor
F	force
θ	angle of the rotated structure in degrees
ρ	density of the water
g	gravitational constant
f	Coriolis coefficient
∇	Nabla orerator
$\nabla\cdot$	The divergence of a vector

1

Introduction

1.1. Natural Hazards

Natural hazards are extreme weather and climate events with significant losses in the built environment and human lives. These types of disasters are included in the Table 1.1, and they occur around the globe at different times and intensities. Some regions appear to be more vulnerable to specific hazards than others. Therefore, vulnerability is closely related to the exposure to natural hazards, to the sensitivity, and to the adaptive capacity of the system [48]. Their potentially destructive character is one point worthy of geological, hydrological, meteorological, social, political, and environmental interest. The context of this MSc thesis is the natural hazards related to unsteady flows that can affect and damage inhabited areas. The ultimate goal from the engineer's perspective is to better understand the fluid-structure interactions during these events and design new methodologies for improving the structural response of the exposed infrastructure to such disastrous phenomena.

Natural hazards	Description
Floods & flash floods	Heavy rain can potentially cause floods in any part of the world. Areas after a long dry period are particularly vulnerable to flooding as the water cannot be penetrated easily by hard ground. Floods can occur during heavy rainfalls, tropical cyclones, monsoons, river swollen by exceptionally high tides, melting snow, ice jams, or dams breaking.
Tropical storms	These tropical climate phenomena (like cyclones and hurricanes) can induce very violent wind and storm surges leading to dangerous coastal flooding.
Tsunamis	Tsunamis are a series of waves produced by undersea earthquakes or by landslides, or volcanic eruptions.
Landslides	Landslides are local events that can be triggered by heavy rainfall or ice melt or loose material on steep slopes, resulting in large amounts of earth flowing. They can reach a speed of over 50km/hr leaving no time for response.
Avalanches	Avalanche is a mass of snow, ice, and debris sliding down a mountainside at speeds in excess of 150km/hr.
Thermal extremes	Heat waves during warmer months of the year, mainly in mid-latitude regions, and extremely cold spells during the winter.
Droughts	Long periods of below-average precipitations. More intense and longer droughts are already recorded in the last years in southern Europe and West Africa, [55]. Massive and devastating fires can be triggered during and after periods of drought.

Table 1.1: Different types of natural hazards, (World Meteorological Organization).

1.2. Unsteady flows

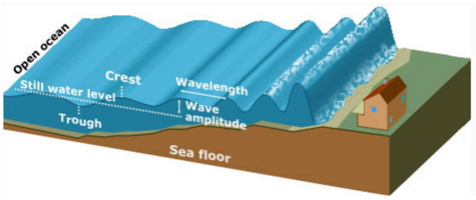

Figure 1.1: An example of the propagation of a tsunami wave under the shoaling effect [53].

Figure 1.2: Examples of long waves acting on urban environments: a & b) During and after flooding, West Germany 2021, precipitation of 15cm/24hrs (the amount corresponds to over 2 months of rain). c) Pakistan flooding, Indus river, 2010. d) Flash flooding, Mandra, Greece, 2017. e) Japan, tsunami 2011. f) Sulawesi, Indonesia, tsunami 2018.

Nowadays, the distinction between natural, man-made, and man-accelerated hazards is quite difficult to draw. Scientists predict that climate change seems to play a crucial role in enhancing both the frequency and the magnitude of several of these phenomena (such as flashing floods, mega-tsunamis due to landslides, and heatwaves) [55]. The Intergovernmental Panel on Climate Change (IPCC report) ventures that more prominent fluctuation and precipitation force will increase flooding risk in numerous territories on account of environmental change in the near future [39].

Extreme natural phenomena are favored by climate change. If the global warming and emission rates continue to the current grade, they would not only threaten the coastal areas due to the Sea Level Rise but also would increase the risk of intense flooding. These unsteady flows, generated by natural hazards, encompass different wave types with different origins and dynamics, the so-called long-wave phenomena (the depth is very small compared to the typical wavelength) [6]. Waves that can be classified as long-period waves are tsunamis, flood waves, dam-break waves and they are some of the most destructive natural hazards. Rapidly changing conditions characterize them, which leave little time for authorities to respond and take action. Long waves have the potential to cause catastrophic flow, during the shoaling process and their propagation inland. According to Green's law, as these waves enter waters of decreasing depths, the littoral, coastal zone (shoaling zone) and start feeling the sea bottom, the wavelength shortens, the wave height increases, hence the wave steepness rises up rapidly, possibly up to the point of breaking [72]. The change of total energy of the tsunami remains constant, hence due to shoaling effect the speed decreases while the wave height rises [53]. In Figure 1.1 a schematization of a tsunami wave under the shoaling effect is presented. These waves produce the power to overflow low-lying coastal areas within some minutes, causing both material damage and casualties [6]. Cities that are confronted with these extreme natural events have to deal with uncontrolled flows and extreme loading on infrastructure, with examples presented in Figure 1.2. Under these flow conditions, not only severe economic impact is expected, but also an escalating number of fatalities on a large scale.

This year, a new study about the global estimation of the number of people exposed to high flooding risks was conducted by Jun Rentschler (The World Bank), in collaboration with Bramka Arga Jafino (Deltares) and Melda Salhab (UCL / The World Bank) [69]. The research shows that almost one-fourth of the world population (1.81 billion people) live at exposed locations to at least 0.15m of inundation depths with a return period of flood event 1 in 100 years. In Figure 1.3, it is clear that exposure to flood risk is substantial, especially in low and middle-income countries such as East and South Asia and Middle East Africa. Regional exposure is mainly driven by single countries (e.g., China, India, Egypt). The top 10 countries regarding the exposed population are presented in figure 1.4. Large population groups are concentrated along rivers (e.g., Bangladesh, Egypt, Vietnam) or in coastal regions (e.g., Netherlands, Indonesia, Japan). This recent research underlines the significance of flood mitigation strategies to prevent the impacts on both life and livelihoods.

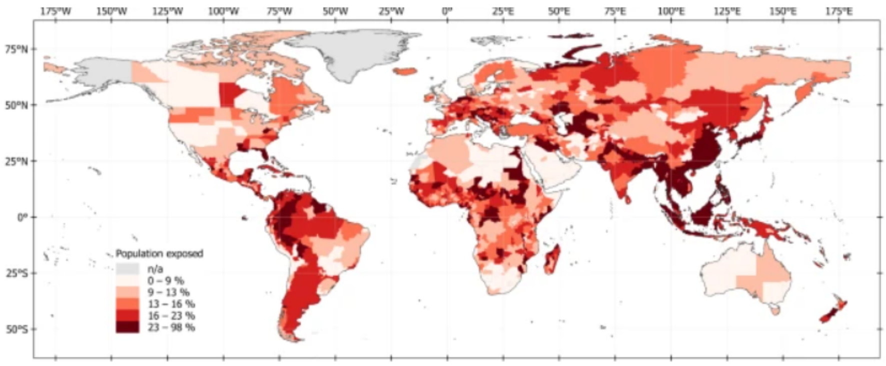

Figure 1.3: Exposed population to floods [69].

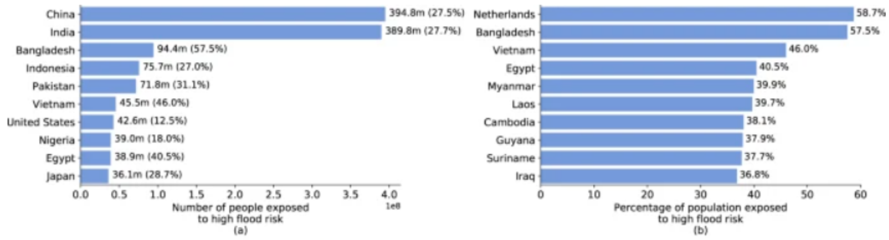

Figure 1.4: Statistical data of exposed population to floods at a country level [69].

Three typical examples that happened only in the last months around the globe are presented in this paragraph, and they strongly support the claim of the scientists that more intense and frequent floods are expected to happen. Firstly, the recent heavy rain and flooding that battered the eastern coast of South Africa on 13 April 2022, with at least 306 deaths, damaged roads, and destroyed properties [26]. It is stated that the heavy rainfall that has descended these few days has wreaked untold havoc and unleashed massive damage to lives and infrastructure [26]. In southeastern Africa, a warming of 2 degrees is projected to bring an increase in the frequency and intensity of heavy rain, strong tropical cyclones, and flooding [26]. Another recent example that has been recorded on 28/5/2022, is the heavy downpour in Brazil, causing the death of 34 people, during 24 hours, in the Recife region, the capital of northeastern Pernambuco state. Climate change and La Nina led to flooding and landslide, resulting in an equivalent amount of rain of 70 % of the forecast for the whole month of May in the city [33]. Lastly, lightning strikes and landslides triggered by severe monsoon storms in India and Bangladesh led to the inundation of vast swathes of the Bangladesh northeast region and deteriorated by runoff from the heavy rainfalls across the mountains of India on 20/06/2022 [95]. At least 84 people have died and more than 9 millions were stranded by raging torrents [95]. Environmentalists have caused alarm about the intensity of these phenomena and the risk appears to be particularly high for countries that are low-lying and densely populated.

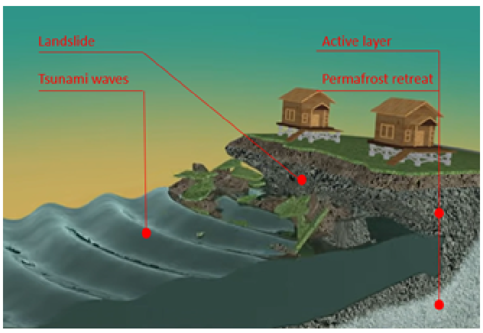

Figure 1.5: Landslide from the melt of the Permafrost.

Moreover, pole areas are even more affected by global warming. Arctic summers are longer and warmer, and the active layer (top layer of soil that thaws during the summer and freezes again during the autumn) penetrates deeper into the ground, affecting the permafrost (thick subsurface layer of soil that remains below freezing point throughout the year in polar regions). The latter one has already started melting and can trigger massive landslides, Figure 1.5, causing mega-tsunamis with wave heights in the order of magnitude of hundreds of meters. An example of this type of wave was the 524 m in Alaska's Lituya Bay in 1958, the most significant mega-tsunami in modern times.

Undoubtedly, the flow due to these phenomena can lead to structural failure. In addition, sea levels are anticipated to rise over 30cm by 2050 for the low emission scenario, and more areas would be exposed to uncontrolled flows [49]. Hence, both the land shortage and the reinforcement of natural hazards create the need to update the design guidelines for the infrastructure since preparation for such events could highly reduce damages and reconstruction costs. It is imperative to understand the inland propagation of unsteady flows to minimize their disastrous effects on the infrastructure. Enhanced resilience allows for better anticipation of disasters and excelled planning to reduce the losses, rather than waiting for an event to occur [83]. Studying the flow-structure interactions induced by unsteady flows, multiple causes can lead to a failure mechanism of the building, such as run-up, drawdown (buildings pushed seaward), or scouring due to high velocities around the structure [92]. In order to better understand these phenomena and inspect the structural response and the failure patterns, a simulation of the flow around the buildings is necessary, as well as the study of the influence of the building's geometric configurations on the exerted loads.

1.3. Dam-break wave

The analytical results of the dam-break wave were validated successfully by experimental results and proved to be a simple tool to predict tsunami surge and dam break wave propagation [17]. As the dam break flow is often used for the generation of the unsteady flow around a building, a more detailed description of the generated waves is presented in this section. A sudden release of stored water in reservoirs is called a dam-break flood wave and can cause severe damage to the adjacent residential areas [78]. More specifically, dam-break flood waves are unsteady, open-channel flows triggered by the failure of a dam. When a dam fails, a large amount of water is instantaneously released and propagates rapidly downstream of the dam. This is mainly justified, due to the significant water level difference upstream of the dam (reservoir) and downstream of it. A large release of a mass of fluid leads to the generation of long waves and disastrous situations can occur proportionally to the size of the dam, and the volume of water that is impounded behind the dam.

Dam break waves have been responsible for numerous disasters escorted by losses of life. An example is depicted in Figure 1.6 for the Teton Dam failure. It is an earthen dam on the Teton River in Idaho, United States. The collapse of it resulted in the deaths of 11 people and 16,000 livestock [59]. There have been around 200 notable dam and reservoir failures in the 20^{th} century worldwide [44].

Figure 1.6: Teton Dam: Catastrophic failure on June 5, 1976 [59]

Dam failures motivate extensive studies for the generation of unsteady flows. It is scientifically proven that is a good representation of these types of flows, such as tsunami-like waves, regarding the research [3, 17, 57, 87, 88] among others. Augus Ritter (1892) [70] was the first one to investigate the dam break and his analytical solution is a milestone contribution to the current studies of unsteady flows. Specifically, the Ritter solution was derived for the ideal case of an initial dry bed downstream of the dam, a horizontal, rectangular, and frictionless channel [70]. On the side of the channel behind the dam, the reservoir is infinitely long and contains water with a depth of h_0. The ideal Ritter's solution for the instantaneous failure of the dam calculates the water elevation h, and the time-averaged velocities as follows:

$$h = \frac{1}{9g} \cdot \left(2 \cdot (g h_0)^{\frac{1}{2}} - \frac{x}{t}\right)^2 \tag{1.1}$$

$$u = \frac{2}{3} \cdot \left(\frac{x}{t} + (g h_0)^{\frac{1}{2}}\right) \tag{1.2}$$

Where h_0 is the initial water depth at the reservoir just before the dam collapses. The dam axis is located at $x = 0$. The ideal solution is widely used to check numerical solutions. The analytical solution involves a positive wavefront propagating at a speed of $c = 2(gh_0)^{\frac{1}{2}}$, for any $x > 0$ and $t > 0$, and a negative translatory wave propagating upstream, $x < 0$ and $t > 0$, at a speed of $c = -(gh_0)^{\frac{1}{2}}$ over the still water. The propagation speed of the positive wave is particularly significant for the assessment of the arrival of the flooding to the populated areas in order to organize the evacuation plan. However, the prediction regarding Ritter's approach is not accurate due to the ideal conditions that are assumed. Specifically, near the front of the positive wave, the friction is dominant, and hence the positive front wave propagation is much slower than the predicted ones by Ritter's theory [14]. A qualitative representation of the comparison between the analytical solution of Ritter (1892), and the real response of the wave structure according to experimental observations is depicted in Figure 1.7. The effect of the hydraulic resistance, which provided the solution to the aforementioned overestimation, was addressed by Whitham (1955) [85]. Theoretical studies have limited applicability and therefore, physical and numerical models are required for evaluating the flood hazards of dam failures with higher accuracy.

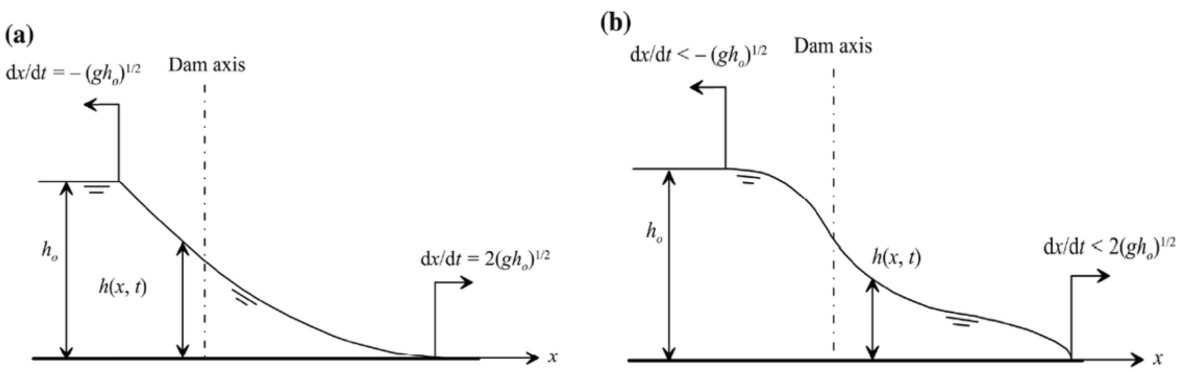

Figure 1.7: (a) Ritter's ideal wave propagation of a dam failure, (b) real representation of the wave structure regarding experiments, [14].

Laboratory experiments were conducted to specify the flow and derive water depth and velocity relationships involving, among other things, obstacles or irregular topography, [46, 76, 82]. Physical models proved that a surge on a channel with a dry bed appears different hydraulic behavior than a bore propagating on a wet bed that is covered by an initial, still water level downstream of the dam of h_f (Figure 1.8). As it is stated in the experimental research [87] a dry bed surge (which represents the first incoming flood wave) propagates faster and with a milder increase in water depth than the wet bed bores, which appear a sudden increase in water depth for the same initial conditions. The wet bed bore results in slower celerities which are associated with the additional resistance due to the presence of the initial still water level in the channel.

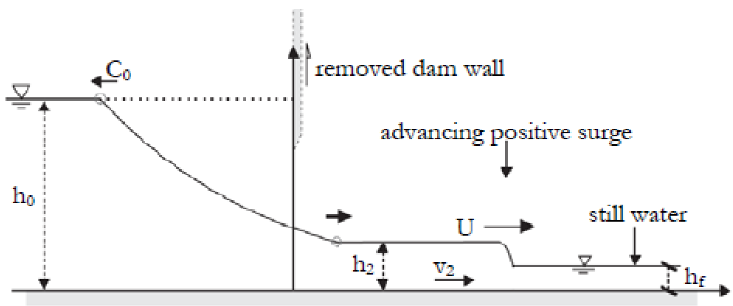

Figure 1.8: Ideal dam break wave with an initial water depth h_0 and h_f at the reservoir and the channel, respectively, [15].

High-quality experimental datasets provide a reliable benchmark for the calibration of numerical models [76]. Two-dimensional depth-averaged modeling is widely used for the further investigation of dam-break flows. Efforts have been made for three-dimensional models, however, the application is computationally expensive and has not proved to be much more accurate than the 2D shallow water models.

1.4. Problem Statement

For the scope of this research, a numerical simulation of a dam-break wave hitting a rigid impervious building is built up using a 2D shallow-water equation model. Due to the rare occurrence of these extreme phenomena, the current research in this field is limited. Despite the studies carried out so far, the impact of the unsteady flows on buildings with different orientations to the flow direction is a poorly understood subject. Therefore, a further focus needs to be done on wave-induced loads on different geometric configurations of the building, to come up with a safer and more reliable infrastructure. In particular, a combination of both experimental data and a numerical model, called the hybrid approach, is necessary to address the solution with the optimum level of simplifications and deal with the physical phenomena and interactions. The purpose of hybrid modeling is to combine aspects of both physical and numerical approaches to overcome the difficulties and the limitations that each method confronts and derive results, closer to reality.

1.5. Objectives and Research Questions

This research introduces a numerical method simulating a dam failure by using shallow water equations. The first objective of the Master Thesis is to build up a Finite Element Method for shallow water equations simulating physical experiments of unsteady flows. The model, then, can be validated using the measured data of physical models that have been already verified by previous laboratory research. This will enable the determination of the hydraulic loads acting on a building and set the foundation for the optimization of the building design to provide safe vertical shelter.

Based on the introduction and the problem statement, the main question to be answered in this study is presented below:

"How can the numerical tools be used to model, validate and implement our current knowledge on the loading process of unsteady flows acting on a rigid structure with different geometric configurations?"

To answer the main research question a list of sub-questions/tasks are addressed below, pointing out:

- **Numerical model development:**
  How can the shallow water equations be modeled to generate a dam-break wave?
  For the setup of the simulation, several elements need to be considered and studied for the optimum approximation of the fluid-structure interactions with a moderate computational cost.
  - Mathematical formulations and numerical method to solve the shallow water equations
  - Development of a FEM simulation: domain definition according to the experimental setup, identification of the mesh, space, and time discretization, set of initial and boundary conditions, implementation of the turbulence model, and stabilized parameters ensuring the functionality of the solution.
- **Validation of the numerical model:**
  Does the comparison between numerical results and physical data ensure the accuracy, reliability, and validity of the simulated dam break flow?
  Model validity is a mandatory step to evaluate whether the obtained results are reliable for further investigation.
- **Impact of dam-break flow on the building:**
  How does the structure experience the horizontal loads that are generated by the unsteady flow of the dam-break wave?
- **Effect of building's orientation:**
  How does the orientation of the structure affect the loading process?
  The effect of building orientation with respect to the wave propagation direction is investigated. The results are analyzed and the numerical model can be used to extend the range of the model.

1.6. Thesis outline

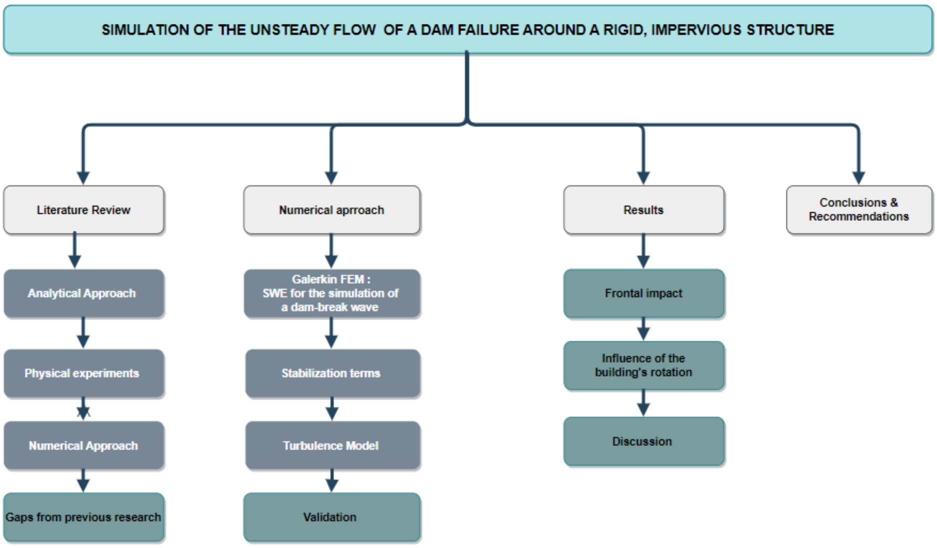

Figure 1.9: Flow of the outline of the Master Thesis.

The structure and the outline of the Thesis project are presented in Figure 1.9, including a schematization graph.

In the second chapter, a literature review was performed for unsteady flows around structures, caused mainly by dam failure or tsunami-like waves. Special attention was given to the gaps from the previous studies, and analytical, physical, and numerical approaches were taken into consideration.

In the third chapter, the numerical approach is presented together with the generation of the code. The dam-break numerical model is based on the Galerkin Finite Element Method of shallow water equations. The boundary and initial conditions are set, as well as the additional stabilized terms to consider turbulence and to normalize any discontinuities.

In the fourth chapter, the validation of the numerical simulation proceeds regarding two different experimental studies. Initially, the data of a dam break wave experiment are used without including a structure. The physical model is conducted in the water lab of the Technical University of Delft. In this way, the induced flow of the dam-break model in the two-dimensional finite domain is validated. Afterward, the study by Wüthrich (2018) [86] is used for further validation of the flow around the structure.

In the fifth chapter, the second validated experiment is used for further investigation into the loading process of different geometric configurations of the impervious building. Water elevations and averaged velocities are derived at fixed points around the structure and the horizontal forces acting on the building boundaries.

In the last chapter, a discussion is performed about the results and the approach that is used. The conclusions of the study are summarized, including recommendations for future research.

2

Literature Review

2.1. Existing Design Codes

Catastrophic events, caused by flooding, affect flood-prone areas worldwide. On the one hand, the scarcity of the appearance of the unsteady flows in the built environment leads to a significant lack of databases, which has an aggravating impact on scientific research. On the other hand, their increased frequency in the last decades due to climate change and the disastrous effects on structures steer the attention of politicians and engineers towards the need for assessment of unsteady flows and their impact on the infrastructure. Significant effort has been made in Flood Risk Analysis and Mapping including flood-mapping of riverine and coastal zones (FEMA 2016, FEMA 2021). However, a comprehensive methodology for risk assessment of the dynamic loading on buildings during a flood event is still missing.

Tsunamis are the first long-period wave loads considered for risk mitigation, in the design codes of countries at the edges of tectonic plates, where the lurking danger of a tsunami is likely to affect the coastal areas. Design codes, like the American Society of Civil Engineers (ASCE 7 – 16), and the Coastal Construction Manual of the Federal Emergency Management Agency, focused on the best practices in hazard identification, planning, design, and construction, that can be used to maintain sustainable and livable coastal communities [42]. Many coastal areas are subject to natural hazards from flooding, earthquakes, and tsunamis, which are infrequent, but inherently destructive [19]. The need for resilience - the ability to prepare, plan, absorb, recover and more successfully adapt to adverse events - leads to the consideration of these types of loads and their effects on the infrastructure. ASCE Tsunami Design Provisions apply only to the States and territories with quantifiable probabilistic hazards: Alaska, Washington, Oregon, California, Hawaii, Guam, American Samoa, and Puerto Rico, and for buildings and structures Risk Category III and IV, and Risk Category II for buildings higher than 65 ft (19.81 m). Regarding ASCE regulations, the special considerations for tsunami design are listed below:

- Local tsunami inundation mapping of hydrodynamic loading parameters, based on the probabilistic regional offshore tsunami heights.
- Flow acceleration in urban landscapes. Analyze the key loading phases of depth and velocity in momentum flux pairs.
- Scour depth at the perimeter of the building which can be equal to the flow depth.

The Japanese government has conducted extensive tsunami simulations using improved scientific data and methods and considering inundated areas from recent and historical tsunami events. The above provides rational tsunami hazard maps that are of primary help for earthquake and tsunami disaster mitigation planning. The tsunami evacuation buildings are primarily required to have the capacity to resist anticipated tsunami loads, without collapse, overturning, or lateral movement for the life safety of evacuees [54]. Breakaway components are allowed to fail under a specific tsunami load without causing damage to the building system [54]. The following Figure 2.1 presents the specific guidelines of the basic flow of the structural design procedure.

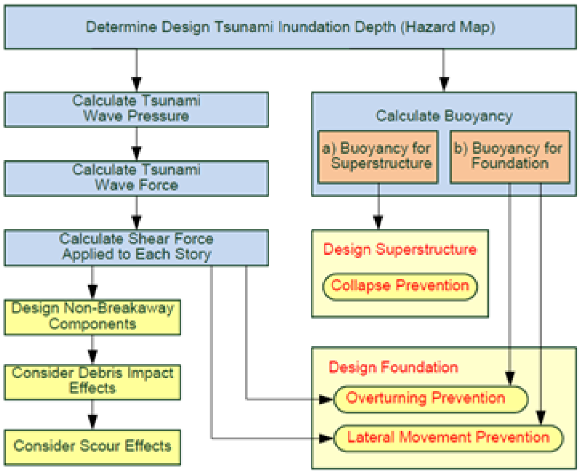

Figure 2.1: General design structure procedure according to the Japanese guidelines [54].

Moreover, the Japanese structural design guidelines (SMBTR) calculate the design horizontal force based on the hydrostatic pressure distribution, and by using three times the incident wave height in the equation 2.1 [90]:

$$F_{x,D} = \frac{1}{2} \cdot \rho \cdot g \cdot B \cdot (3 \cdot h_{max})^2 \tag{2.1}$$

Where, ρ is the water density, g the gravity constant, B the building's width, and h_{max} the maximum incident wave height. The same equation was used by the guidelines CCH. However, the equation overestimates the actual value of the load.

The formulas are uncertain, and applicability is sometimes questionable. Design issues remain to be examined and described more quantitatively, such as the pressure distribution and the impact of unsteady flows acting on structures.

2.2. Previous research

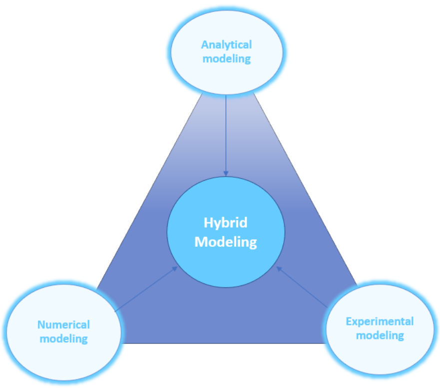

Figure 2.2: Schematization of hybrid modelling.

The flow around buildings that occurs due to these unsteady flows is mainly three-dimensional, and the multiple parameters that affect the flow conditions make the present research very challenging. In order to better understand and optimize complex processes, numerical techniques provide a useful tool for obtaining approximated solutions [51]. Analytical solutions are based on the simplification of the physical process, and so the actual phenomena are not described accurately. A balance between the level of accuracy and simplifications should be achieved, and the optimum way to approach this is by hybrid modeling [51]. This suggests a combination of verified laboratory results and a numerical simulation in order to validate the mathematical model, as well as to deepen the understanding of the physical processes, Figure 2.2.

It follows a literature review focusing mainly on dam-break waves since it is the simulated case for this thesis. The previous studies are subdivided into three main categories: analytical, physical, and numerical approaches. In the end, an overview of the gaps arising from the previous studies is conducted. Analytical approaches, laboratory experiments, and numerical models seek to comprehend the onshore propagation of unsteady flows.

2.2.1. Analytical Approach

Analytical studies were the first attempts to investigate the propagation of dam-break waves and they represent ideal dam-break waves. Ritter (1892) [70] yielded a simple analytical solution of a dam break wave on a horizontal, dry and frictionless channel, Whitham (1995) [85] and Dressel (1952) [31] included both the effect of bed resistance in their analytical approximation with different approaches. Chanson (2005) [16] focuses on a simple solution of a dam break wave using Saint-Venant equations and the method of characteristics. The effect of a slopping channel, with turbulent motion and an initially dry bed, was studied by Chanson (2009) [18]. As previously stated, these ideal analytical approaches are not sufficient to describe more complicated cases, which include the interaction between the flow and buildings.

2.2.2. Experimental Modelling

Several experimental studies of unsteady flows were carried out in the laboratories. Some of the main focuses were the time history of the water elevations, the velocities, as well as the impact loads generated by highly unsteady flows. The dam failure technique was used for the generation of other unsteady flows, such as tsunami-like waves and it is proved to be an optimal way to reproduce them. Several researchers have used the dam-break approach to generate tsunami-bore fronts, including Arnason (2005) [3], Chason (2006) [17], Nouri et al. (2010)[57], Wüthrich et al. [87, 88] among others. The dry bed surges represent the first incoming tsunami-like wave, and the wet bed bore the following waves after the passage of the first one, where inundation depth needs to be taken into account [87]. The frontal impact on impervious buildings was investigated by several studies, to introduce formulas for the calculation of the wave-induced loads [3, 57, 74, 87, 88, 91].

Arnason (2005) [3] focused on tsunami bore propagation around free-standing, impervious buildings of simple shapes. Measurements included water elevations, velocities, and the forces acting on the buildings. In terms of orientation, the 45° angle of the impervious square building was studied. Soares-Frazao and Zech (2007) [76] generated the dam-break flow against a single, rectangular building experimentally. The water elevation and the velocities are recorded at different locations.

Figure 2.3: City layout for the experimental research [82]

Flooding of an idealized urban district model was studied in the laboratory by Testa et al. (2007) [82]. The experimental layout is depicted in Figure 2.3. A formation of a strong hydraulic jump upstream of the buildings was noted, but as the flow progressed further downstream, the friction and the reflection dampens the wave pattern, and the flow is more uniform [82]. Hence, the largest impact occurs at the front buildings, and these present the highest study interest.

Moreover, Shafiei et al. (2016) [74] investigated the role of the orientation of the building (4 different orientations were tested with respect to the original alignment of the front wall: 0°, 30°, 45°, 60°) to the velocities, bore wave heights, and to the pressure distribution. Overall, the drawn conclusion from the research was that the pressure distribution depends on the orientation of the structure with respect to the flow direction. an increase in the building's orientation relative to the flow direction decreased the pressure, and the drag coefficient.

Physical experiments were undertaken to study the performance of an isolated building in dam-break flow by Liu L. et al. (2018) [46]. Both orientation and openings were considered. The maximum forces occurred for the orientation of the building perpendicular to the flow and without openings. Experiments by Qi et al.

(2014)[65], Wüthrich et al. [87, 88, 91], and Arbos et al. (2018)[94] were also studied the effect of orientation. The results showed that post-peak steady flows can be well represented by the sub-critical, choked regime, as the Froude number is approximately 1 for tsunami flows propagating inland. Thus, the loading process of buildings was investigated under steady flow conditions, with different degrees of orientation, and with or without openings. In terms of orientation, the rotated impermeable building increases the blockage ratio, leading to an increase in horizontal forces. Although the forces are applied at lower cantilever arms, leading to a reduction of the moments [91, 93].

2.2.3. Numerical Modeling

Physical modeling has been fundamental for the study of processes related to long-period waves interacting with structures. However, they face several problems and limitations. In the last few decades, considerable research has been devoted to the development of numerical models. The objective was to identify the simplest model which could replicate the behavior of interest with adequate accuracy [7]. However, due to the complexity of the water motion, the lack of observation data, and the simplifications of the numerical scheme, the validation is still ongoing, [11].

The numerical simulation of a dam-break flow was investigated using many different approaches, without considering a structure. Tan (2009) [80] simulated the dam-break flood wave using the One-Dimensional Saint-Venant (1DSV) model. In the last decades, it is a common practice to simulate unsteady flows with dam-break flood waves with CFD (Computational Fluid Dynamics) or SPH models (Smoothed Particles Hydrodynamics). Liang D. (2010) [45] applied both methods to compare the results with measurements and assess them. The SPH method proved to be more accurate, but the shallow water equation model has the advantage of solving very fast compared to the SPH one. Oscar Castro-Orgaz O. and Chanson H. (2017) [14] approached accurate solutions of the viscous dam break wave propagating over a dry-bed using the MUSCL-Hancock finite-volume method and the discontinuous Galerkin finite-element method.

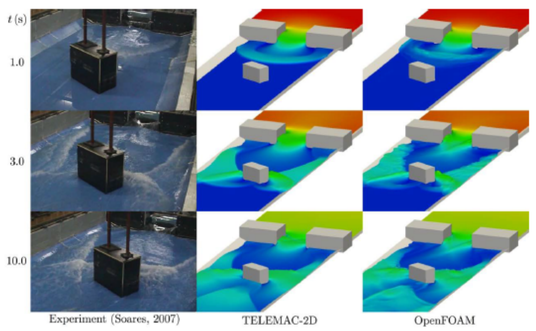

Figure 2.4: Visuzlization of the free-surface elevation (blue: 0m, red: 0.4m) at times 1s, 3s, and 10s [71]

Later studies include obstacles inside the domain to reproduce flow-structure interactions. Jacobs and Piggott (2015) [40] used shallow water equations, and a dam failure was used to validate their model. Then they simulate the flow around a square cylinder, including the Smagorinsky LES model [75] as the turbulence model. Robb and Vasquez [71] investigated the capability of three different numerical models to simulate sudden dam-break flows in the presence of an obstacle. The selected models are (a) the free and open-source code TELEMAC-2D, (b) the commercially-available CFD software package FLOW-3D, and (c) the free and open-source CFD code OpenFOAM, concluding that OpenFOAM provides one of the best results derived so far. However, the hydrodynamic forces were not computed in this research.

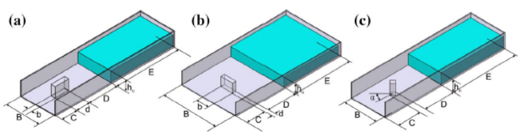

Figure 2.5: Structural geometry variation (a) elongated column, (b) rectangular wall, (c) rotated square column, E = 8.6m, D = 4.75m, C = 2.5 m, AR = b/d, α = 0°, 22.5°, 45°, [4].

Asadollahi et al. (2018) [4] investigated, numerically, the impact of tsunami bores on structures with different aspect ratios and orientations with respect to the direction of the tsunami-like bores using Open-FOAM. The study provided an in-depth investigation of the drag coefficients for elongated and rotating structures. The case of square columns, with a rotation of 45°, resulted in the lowest value of the drag coefficient.

Numerical studies, based on the experimental data on tsunami-like wave impact acting on buildings, were carried out using SPH simulation by Wüthrich et al. (2019) [89] and Nishiuraa et al. (2019) [56]. The results were compared to large-scale experimental data for dry bed surges and wet bed bores, impacting free-standing buildings with and without openings. The visual results of the SPH numerical approach were able to well reproduce the key features of the flow during and after the impact on the impervious building for both dry bed surge, and wet bed bore, as shown in Figure 2.6. Furthermore, Figure 2.7 presents the sequence of the complex flow through a porous building. From the derived results, inconsistencies were noticed compared to the experimental tests, and higher spatial resolution is required in order to avoid some computational instabilities. For the case of the dry surge, the neglect of channel floor roughness plays a significant role in the deviations in the results. Moreover, the effect of turbulence and air entrainment, in the case of the wet bed bore, needs to be taken into account. However, with SPH numerical simulation, the aeration process cannot be considered. In the case of the wet bed bore, channel floor roughness can be assumed negligible.

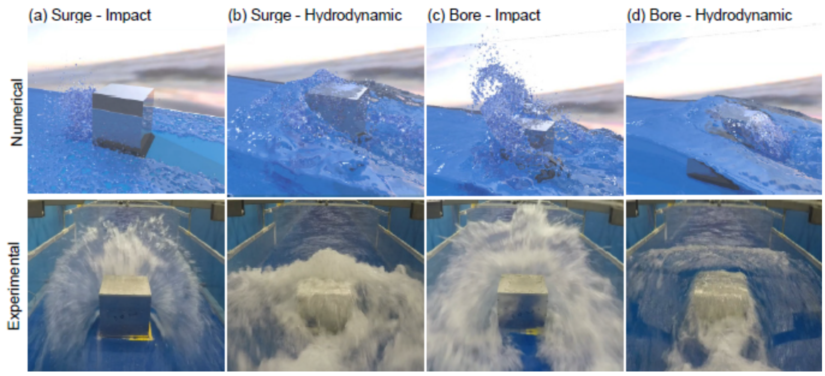

Figure 2.6: Comparison of numerical and experimental tests during wave impact of dry bed surge $d_0 = 0.63m$, and wet bed bore $d_0 = 0.63m$, $h_0 = 0.05m$, impervious building, [89].

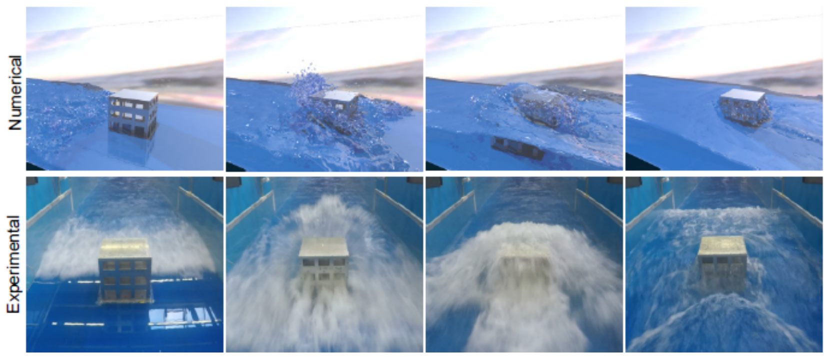

Figure 2.7: Comparison of numerical flow simulations with the experimental tests for a wet bed bore $d_0 = 0.63m$, $h_0 = 0.05m$ impacting on a porous building, [89].

Prasetyo et al. (2019) [63] conducted a physical and numerical analysis to investigate the inundation process in a complex coastal city. The data that were used for the validation of two numerical models are from the Tohoku tsunami (2011). Numerical modeling (in 2D) uses bore conditions, and it is in agreement with the experimental results, in terms of maximum water level and arrival time. These results are more reliable compared to the ones derived for a solitary wave (3D modeling). Nevertheless, errors are included due to the difficulty of modeling the bottom roughness and topographical conditions in shallow water regimes. The topography elevation variation and the presence of macro-roughness elements (such as buildings and houses) negatively affect the accuracy of the results. Another research relative to urban planning is conducted by Hien and Van Chien (2021) [37] who investigated the ability to simulate flood waves in the presence of an isolated building or building array in an inundated area. Two different numerical models was checked: a 2D numerical model, which was based on the finite-volume method (FVM) to solve 2D shallow-water equations (2D-SWEs) on structured mesh, and the 3D commercially available CFD software package. Both models were quite accurate in deriving the forces. Different conditions, such as different geometric configurations, should be implemented in the future.

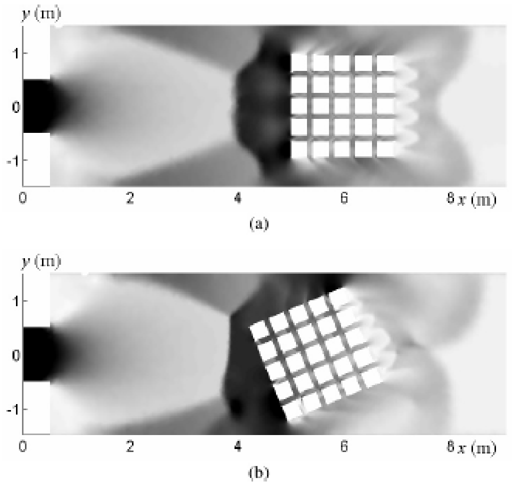

Figure 2.8: Visualization of the water depth at t=10 s for Case 1 and Case 2 [77].

Soares-Frazão and Zech [77] simulated the dam-break flow through an idealized city to investigate the effects of the flow depth and velocities, for two different cases. **Case 1**: a square city layout of 5×5 buildings aligned with the flow direction, and **Case 2**: a square city layout of 5×5 buildings not aligned with the flow direction, Figure 2.8. Using a two-dimensional Finite Volume scheme to solve the shallow water equations, the water elevations and velocities were compared to the experimental measurements giving an accurate representation of the flow. However, further analysis should be done regarding different orientations, impact on the walls, irregular layouts of the streets, etc.

Most recently, Pringgana et al. (2021) [64] explored the influence of orientation and arrangement of structures on tsunami impact forces using SPH method. The meshless formulation of the SPH method allows for a better simulation of the bore and tsunami-structure interactions. It is clear that structure S3, in Figure 2.9 faces a higher impact force compared to the front structures S1 and S2, due to the flow-focusing effect, while S4 and S5 are influenced much less by the bore flow due to the sheltering effect. This led to the conclusion that the positioning of the structure can significantly reduce the tsunami force acting on it. The comparison between experiments and numerical simulations shows that areas where the flow depth and velocity drop significantly appear at the lee side of the building. This can be useful for the placement of shelter buildings behind another study structure. This would reduce the cost and increase the safety of the structure, by reducing the acting loads, and enhancing the stability.

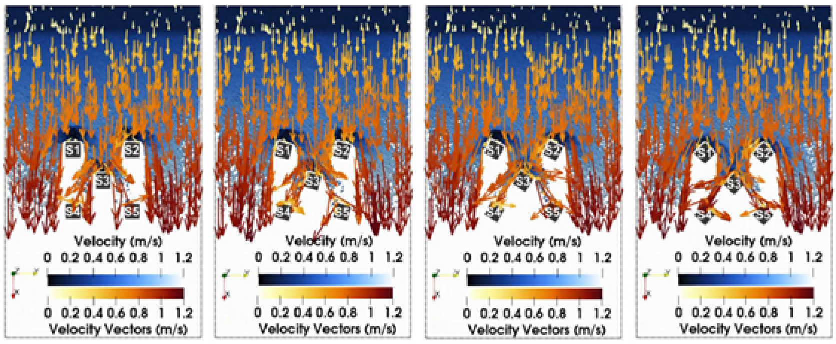

Figure 2.9: SPH simulation with building angle of: a) $R = 0°$; b) R=15; c) $R = 30°$; and d) $R = 45°$, at t =19.3 s, [64].

2.3. Summary

The results from the previous research, although promising, are still lacking accuracy and reliability to provide clear insight into the fluid-structure interactions. To support a safe design for the critical infrastructures further investigation is therefore required. Previous literature reviews showed that long waves acting on structures is a relatively new research field with high complexity, and hence, several research gaps have been observed. Both physical and numerical modeling proved that little focus was given to the loading process of buildings with different orientations, and recent research has shown that pressures are reduced with the rotated configuration of the building with respect to the flow direction. Moreover, the estimation of flood velocities in coastal flood hazard areas are subjected to uncertainties [29]. Hence, research lacks knowledge in estimating inundation depths, flow-induced forces, and moments.

Gaps and limitations concern both physical and numerical approaches. The physical modeling uncertainties have mainly to do with limitations of currently available instruments, associated with the unsteadiness of the phenomena. Changing all the governing parameters, one by one in a laboratory experiment is time-consuming and economically unfavorable. Moreover, experimental modeling has to deal with problems such as scale effects, duration of tests, and model effects.

Therefore, numerical techniques can provide a useful tool for obtaining approximate solutions. Numerical modeling applies to complex geometries and deals with different parameters at the same time, limiting the total duration of the simulation, the cost, and the complexity of the interactions between fluid, structure, and coast, which can be more easily and more accurately managed and studied. Despite the great development in numerical simulations, models, simulating unsteady flows, such as dam-break waves, remain insufficient regarding the validation of the flow and the interactions with the built environment. Simulations are based on simplifications that insert errors, as the flow around the building is complex (3-dimensional) with multiple parameters affecting the physical phenomena. The accuracy can be improved using higher spatial and temporal resolution and a turbulence model to deal with the turbulent secondary flows and the discontinuities of the unsteady flows. However, this increases the solving time and therefore can be computationally expensive. The numerical uncertainties make necessary the use of the experimental data for the validation of the numerical results.

Regarding the above, a hybrid approach constitutes the ideal solution to analyze, and better comprehend the fluid-structure interactions caused by the unsteady flows. The numerical model will be developed guided by physical experiments, which will be used for the validation of the numerical simulation.

3
Numerical Approach

The analysis of the surface water flows is of critical importance in obtaining more insight into the unsteady flows and predicting a wide range of hydraulic engineering issues. It has been generally proven that the non-linear shallow water equations are valid for the representation of the detailed flow of tsunamis or other long-period waves around hydraulic structures [62]. Dam failure problems are commonly used to test the performance of shallow water models. The simulation of this particular study employs a dam-break system for the generation of the incompressible, turbulent flow.

Over the past four decades, finite elements were used, in different ways, to obtain the numerical solution of the shallow water equations [1, 2, 43, 73]. Among the different approaches, the discontinuous Galerkin Finite Element Method (DG FEM) is used for this research to simulate numerically the depth-averaged shallow water equations, combined with a turbulence model. The DG FEM uses stabilization terms, for capturing the large eddies of the flow, as well as the discontinuities that are produced by shock waves [23]. It is a well-suited approach for complicated geometries and deforming meshes (which is the case for flooding simulations to capture shocks or sharp fronts), for using different polynomial orders of approximation in different parts of the domain [43]. It is based on the idea to approximate the solution by piecewise polynomial functions over a FE mesh without any requirement on inter-element continuity [30]. It is proven to be valid for the modeling of time-dependent flows Ambati and Bokhove [2]. Through the stated method, the free-surface flow and the depth-averaged velocities of a dam-break wave are approximated on a limited domain.

Initially, the methodology of the research is presented paired with the assumptions that are considered to estimate the impact of unsteady flows on impervious buildings. Then, the governing equations (strong formulas) are derived. The problem definition is set up, and the schemes are introduced with the boundary and initial conditions. The strong formulas are transformed into the weak ones by applying the FEM. At the end of this chapter, the additional terms and the turbulence model are presented to deal with the discontinuities and the different scale phenomena that unsteady flows evoke.

3.1. Methodology

This study uses numerical modeling for two-dimensional, non-linear, and non-rotational shallow water equations, based on the Finite Element Method (FEM) to reproduce the flow around a building. The equations are a depth-averaged horizontal set that models the dynamics of a free surface and an associated depth-averaged velocity field. Moreover, the Fluid-Structure interfaces are modeled in the two-dimensional domain Ω, considering the rigid and impervious structure as a non-slip boundary for the flow. A schematization of the methodology is presented in Figure 3.1.

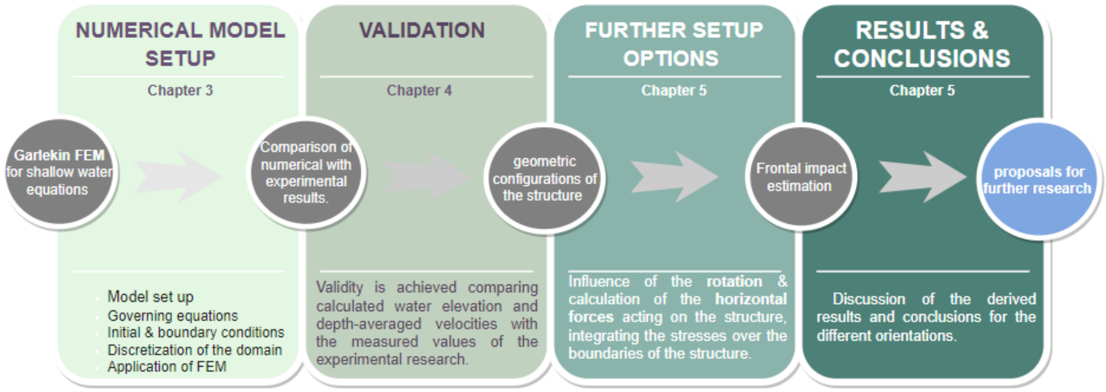

Figure 3.1: A schematization of the methodology

In order to compute the frontal impact, the stresses acting on the examined building configuration are derived and then integrated over the wet building's boundaries to estimate the total horizontal forces in x and y directions.

3.1.1. Assumptions

Numerical models approximate the solution by using simplifications to reduce computational time and cost. The following assumptions are made to simplify the numerical approximation, regarding the flow's behavior in shallow water:

- The fluid is considered incompressible. Density-invariant in time and space.
- Due to shallow water, a relatively uniform distribution of the horizontal velocity over the vertical is obtained, and depth-averaged velocities are to be used, assuming that the vertical velocity is zero. The three-dimensional flow can be simplified into a plane flow by integrating the horizontal velocities over the vertical to obtain depth-averaged values (2D representation of the flow), equations (3.7) and (3.8).
- The properties of the fluid are temperature-independent.
- The flow is unsteady. Large scale flows (vortices) are captured by the model but smaller vortices can be considered as a secondary flow imposed on the main flow.
- The bottom of the channel is considered horizontal and not limited by the formulation, smooth, and impermeable.
- The structure is considered impermeable, undamaged, and thus, fixed and rigid during inundation.
- The structure is considered sufficiently rigid to neglect all deformations.

In terms of forces, only the horizontal forces are considered for the two-dimensional, horizontal model, and the following are excluded from the computations:

- Coriolis inertial force.
- Uplift and the load of buoyancy, which results from the displacement of a given volume of flood water, is not considered for this thesis, as the two-dimensional representation of the flow does not include the vertical dimension, and consequently, the vertical loads are all excluded from the results.
- The astronomical tide is exerted by the gravitational pull of the moon and the sun.
- Debris or other features that can act as obstacles or as additional loading are not taken into account in numerical modeling.
- Wind stresses over the water surface.

3.2. Considered loads

- Hydrostatic loads
  Standing water or slow-moving water can exert a hydrostatic pressure normal to any contacting surface. These stresses on the surfaces can induce hydrostatic forces against the structure, in case the water levels are not equal on the different sides of the structure. The hydrostatic forces act laterally or vertically. The first ones are generally not sufficient enough to cause deflection or displacement of the building as a whole or to its components, although the vertical ones have quite a high impact on the structures [29].

- Hydrodynamic loads
  Hydrodynamic forces, called also drag forces, are exerted by flows with high velocities around the structure and they have the same direction as the flow. Total drag is formally defined as the force corresponding to the rate of decrease in momentum in the direction of the undisturbed external flow around the body [38]. Drag forces are undesirable as high-velocity flows are capable of destroying single elements and even dislodging buildings with a pour foundation [29].

  Drag forces are caused by two different types of stresses which act on the surface of the object of interest, deviatoric stresses, and volumetric stresses. First, the wall shear stresses, or deviatoric stresses, which are acting parallel to the object's surface, induce the skin-friction drag. This component is more significant in case a large surface of the object is aligned with the direction of the flow. This traction is due to viscosity and acts tangentially at all points on the body surface [38]. Moreover, pressure stresses are acting perpendicular to the object's surface and are caused by how pressure is distributed around the object.

3.3. Software

In the upcoming Figure 3.2, a schematization of the software that is used is presented in a graph and then, each of them are described analytically with respect to their contribution to the present research.

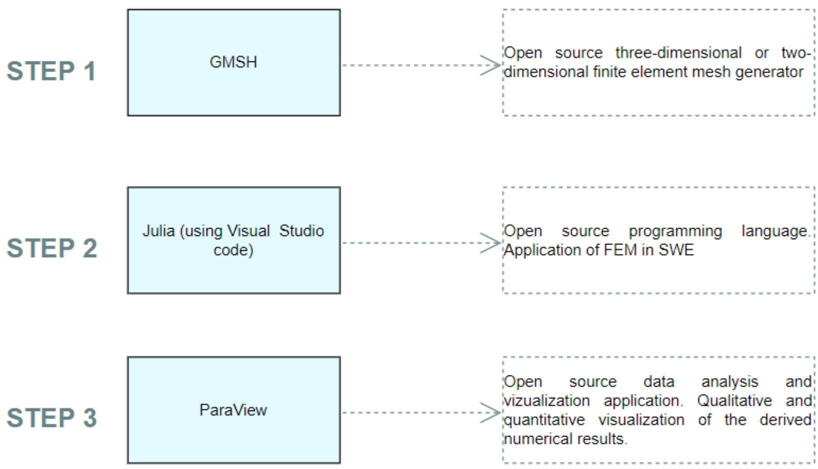

Figure 3.2: Used software

GMSH: Gmsh is a finite element mesh generator with 4 different modules: geometry description, meshing, solving, and post-processing [35]. Each examined case of this research has an explicit ".geo" file which is generated using Gmsh open source. The "geo" files can be processed as text files. Using Julia these files are converted to JSON files,".json", and then, the code can read them to derive the numerical results.

Julia: The numerical method proceeds using Julia as the programming language in the environment of the Visual Studio Code using the library Gridap [47]. Julia is a high-level, dynamic programming language that is used for numerical analysis [8]. Several development tools support coding in Julia and the environment of Visual Studio Code is used. Visual Studio Code is a streamlined code editor supporting development operations like debugging.

ParaView: ParaView is an open-source, multi-platform data analysis and visualization application, where users can quickly build visualizations to analyze their data using qualitative and quantitative techniques [60]. The visualization of the flow is achieved through the generation of ".vtk" files that can be used in ParaView for a qualitative representation of the results and for further processing.

3.4. Shallow Water Equations

The model of this Thesis describes the non-linear, non-rotational shallow water equations. A set of depth-averaged equations describes the free surface elevation and the depth-averaged velocity field. The 2D model for the free surface flow is usually enforced by a horizontal scale much larger than the vertical one, and by a velocity field that is quasi-homogeneous over the water depth [28]. The two-dimensional shallow water equations are obtained by depth averaging the three-dimensional, incompressible Navier-Stokes equations. The 2D solution is a good approximation for long-period waves. The general characteristic of long waves is that the horizontal wave-length scale is much larger than the depth $L >> d$, fulfilling the condition for the shallow water approximation. Hence the vertical acceleration is negligible compared to the gravity and the vertical velocities compared to the horizontal ones respectively [66]. This means that the horizontal motion of water mass is relatively uniform in the vertical direction (bottom to the free surface).

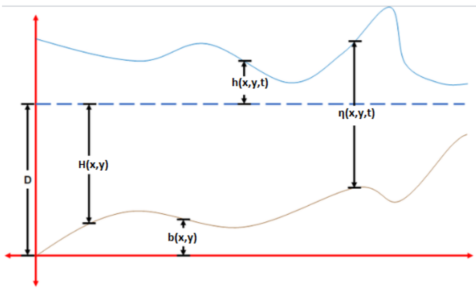

Figure 3.3: Depth notation for 2D shallow water.

The governing equations consist of the continuity and the momentum equations, where u and v the unknown field of the horizontal,two-dimensional depth-averaged velocities in x and y directions respectively, and free surface $\overline{h} = \eta(x,t) = H(x) + h(x,t)$ are sought. The velocity is approximated by the depth-averaged flow velocity, which is denoted by u(x,y,t). The free surface is separated into a mean free surface depth component $H = H(x,y)$ and a free surface perturbation component $h_p = h(x,y,t)$ as illustrated in Figure 3.3. The topographical height from a reference D=0 is considered to be horizontal, therefore it is not taken into account for the depth calculation, b(x,y)=0. The equations (strong form) governing mass and momentum conservation can be written in the tensor notation for their implementation in the numerical simulation as follows.

The continuity equation in the 2D domain, where ρ is the density of the fluid.:

$$\frac{\partial h}{\partial t} + \frac{\partial(u(h+H))}{\partial x} + \frac{\partial(v(h+H))}{\partial y} = 0 => \frac{\partial h}{\partial t} + \nabla u(H+h) = 0 \tag{3.1}$$

The momentum equation, under the assumptions of homogeneous, incompressible, viscous flow:

$$\frac{\partial u}{\partial t} + u\frac{\partial u}{\partial x} + v\frac{\partial u}{\partial y} + g\frac{\partial \eta}{\partial x} = -\frac{\cancelto{0}{fv}}{\rho} + \frac{\tau_{s,x}}{\rho h} - \frac{\tau_{b,x}}{\rho h} - \frac{h}{\rho}\frac{\partial \cancelto{0}{p_a}}{\partial x} + \frac{1}{\rho}\frac{\partial(T_{xx})}{\partial x} + \frac{1}{\rho}\frac{\partial(T_{xy})}{\partial y} \tag{3.2}$$

$$\frac{\partial v}{\partial t} + u\frac{\partial v}{\partial x} + v\frac{\partial v}{\partial y} + g\frac{\partial \eta}{\partial y} = -\frac{\cancelto{0}{fu}}{\rho} + \frac{\tau_{s,y}}{\rho h} - \frac{\tau_{b,y}}{\rho h} - \frac{h}{\rho}\frac{\partial \cancelto{0}{p_a}}{\partial x} + \frac{1}{\rho}\frac{\partial(T_{yx})}{\partial x} + \frac{1}{\rho}\frac{\partial(T_{yy})}{\partial y} \tag{3.3}$$

$$\rightarrow \frac{\partial u}{\partial t} + u\nabla u + g\nabla h = -c_f \frac{\| u \| u}{h+H} + + \frac{1}{\rho}\nabla \cdot \mathbb{T} \tag{3.4}$$

In which h is the water depth, g the gravitational acceleration, f the Coriolis coefficient associated with the Coriolis force, τ_s the friction stress at the surface per unit mass, τ_b the components of the bottom shear stress per unit mass, p_α the atmospheric pressure field at the air-water interface, which is neglected, $\vec{T}$ the eddy viscosity term, which diffuses sharp discontinuities, $\| u \|$ the Euclidean norm, ∇ the derivative in x and y direction, and $\nabla \cdot u$ the divergence of the velocity vector.

- The acceleration term $\frac{du}{dt}$, describes the acceleration of a fluid particle.
- Gravity term $g \cdot \nabla h$.
- Pressure gradient term $\frac{h}{\rho} \cdot \frac{dp}{dx}$. The assumption of long waves implies that the vertical accelerations are neglected, thus the piezometric head is uniform in the vertical and the vertical pressure distribution is hydrostatic. The horizontal variations of the atmospheric pressure are neglected.
- Coriolis term $\frac{f \cdot u}{\rho}$ can be neglected for long waves.
- Bottom friction terms are related to the depth-averaged velocity vector. In shallow water, resistance plays an important role and cannot be neglected. For the bottom friction, the Chezy-Manning formulation is used, [9]:

$$\tau_{bx} = \frac{\rho g}{C^2} U\sqrt{U^2+V^2} = \frac{n^2 \rho g}{h^{1/3}} U\sqrt{U^2+V^2} \tag{3.5}$$

$$\tau_{by} = \frac{\rho g}{C^2} V\sqrt{U^2+V^2} = \frac{n^2 \rho g}{h^{1/3}} v\sqrt{U^2+V^2} \tag{3.6}$$

Where C is the Chezy coefficient, n the Manning coefficient, which defines the resistance of the flow due to bottom roughness and is determined empirically, U and V are the depth-averaged velocities that are defined as follows:

$$U = \frac{1}{h}\int_{z_b}^{h+z_b} u\,dz \tag{3.7}$$

$$V = \frac{1}{h}\int_{z_b}^{h+z_b} v\,dz \tag{3.8}$$

- The free-surface friction terms are described as:

$$\tau_{s,x} = C_D \cdot \rho_\alpha \cdot W_x \cdot \sqrt{(W_x)^2 + (W_y)^2} \tag{3.9}$$

$$\tau_{s,y} = C_D \cdot \rho_\alpha \cdot W_y \cdot \sqrt{(W_x)^2 + (W_y)^2} \tag{3.10}$$

Where C_D is the drag coefficient between free-surface and air, ρ_α the density of air, W_x, W_y velocities of the air in the x and y directions respectively. The wind effect is ignored for the simulation since they are unlikely to be observable on the time and length scale of a long-period wave. Therefore, the surface friction terms can be ignored in this research.

- For the eddy-viscosity terms, the Boussinesq concept is applied. The turbulent kinematic viscosity is represented by the term ν_t. The stress Tensor $\mathbb{T}$ is given by the following equation, where $\mathbb{1}$ is the identity tensor [40]:

$$\mathbb{T} = \rho\nu_t \left(\nabla u + \nabla(u)^T - \frac{2}{3}(\nabla \cdot u)\mathbb{1}\right) \tag{3.11}$$

3.5. Numerical setup

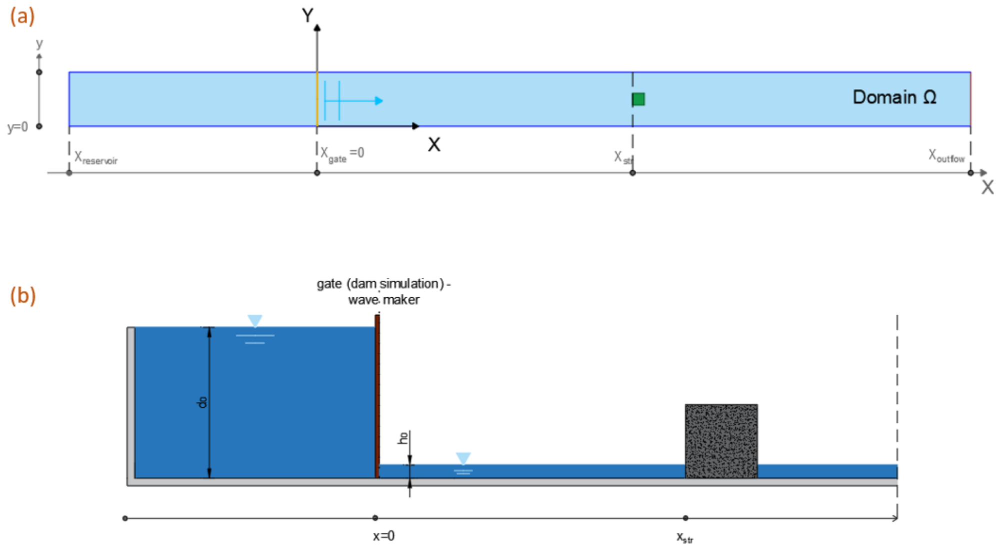

Figure 3.4: Numerical setup for a dam-break wave interacting with a square, impervious building. (a) Upper panel: top view, (b) lower panel: front view.

The described problem is called the dam-break problem as it models the situation where a dam, which separates two different water levels, bursts at $t = 0s$. The hydraulic phenomenon is basically the same occurring in canals during the sudden gate operation [41]. Therefore the dam is represented by a gate in the numerical code. A gate is placed at $x = 0$ and represents the dam. Initially, $t = 0s$, the velocities are zero, both on the left and right sides of the gate, and at $t = 0s$ the gate opens instantaneously to simulate the dam-break wave. Concerning the construction of the model, the initial distribution of water depth is considered piecewise-constant, $H(x \leq 0) = d_0$ and $H(x > 0) = h_0$, where d_0 is the initial water level stored at the reservoir upstream of the gate, and h_0 is the impounded water level at the channel. The general setup of the numerical model is depicted in Figure 3.4. The geometric characteristics of the domain are defined with respect to the experiments that are tested in the upcoming chapters. Similarly, the values of the prescribed initial water levels are set regarding the water level differences in the laboratory setup.

3.5.1. Initial & Boundary conditions

In two-dimensional shallow water models, the nature and number of boundary conditions depend on the flow regime. Local projections of the flow equations in the direction orthogonal to the boundary and multidimensional characteristic analysis of the flow equations indicate that three boundary conditions are needed for the supercritical inflow, two boundary conditions are needed for a sub-critical inflow, one condition is required for a sub-critical outflow, and none is needed for supercritical outflow [36, 50].

The computational domain corresponds to the experimental setup. The x-direction zero coordinate is set at the edge of the gate, and the y-direction zero coordinate is placed at the bottom of the canal. The gate is initially inserted to separate the artificial reservoir (upstream of the gate) and the ambient water (downstream of the gate). The initial water levels are set regarding the experimental cases that are used for the study, and the fluid is assumed to be initially at rest, $u(x, t = 0) = 0$.

Experimental modeling showed that the sub-critical conditions are dominant with the Froude number varying from 0.3 to 0.6. Hence, the Dirichlet boundary condition is going to be implemented at the lateral sides of the domain, at the walls of the structure as well as for the water depth at the outflow, where the water depth is prescribed. Specifically, the boundary conditions are set as follows and they are depicted in Figure 3.5:

- At the right-hand side edge of the domain, at the lateral boundaries, and in general at the solid boundaries (such as the walls of the structure), slip or non-slip conditions can be imposed.
  - The slip boundary condition is imposed at the side walls of the domain, and no boundary condition is required. In this case, it is assumed that the side walls of the domain have no effect on the fluid velocity in planes parallel and close to the walls, the slip velocity depends on the shear stress. Moreover, there is no water penetration, thus the normal velocity is zero at the boundary, $u \cdot \vec{n} = 0$ on Γ_s . Where n denotes the outward-oriented unit normal vector, and Γ_s is the boundary of the side-walls of the domain.
  - The non-slip condition for viscous fluids assumes that at a solid boundary, the fluid has zero velocity relative to the boundary, and no tangential motion (Dirichlet boundary condition) [27]. For the boundaries of the structure, impermeable wall boundary and no-slip conditions are implemented, which are typical for analyzing flooding around buildings in urban areas. Both normal and tangential velocities are zero, $u = 0$ and $u \cdot n = 0$ on Γ_w.Where Γ_w is the boundary of the structure's walls in the domain.
- Inflow and outflow boundaries:
  - Inflow ($x = x_{in}$): Constant discharge is prescribed, controlled by the volume of water.
  - The outflow boundary condition at the right-hand side: a sub-critical flow regime water depth is assumed to be prescribed: $h = h_{out} = h_{uniform}$, on Γ_{out} For the calculation of the outflow depth, it is assumed that the channel is infinitely long, for the examined duration of T=20s, to avoid the reflection effect in the domain. Therefore, a value of 0.001m was used for the outflow boundary, and the results showed a good agreement.

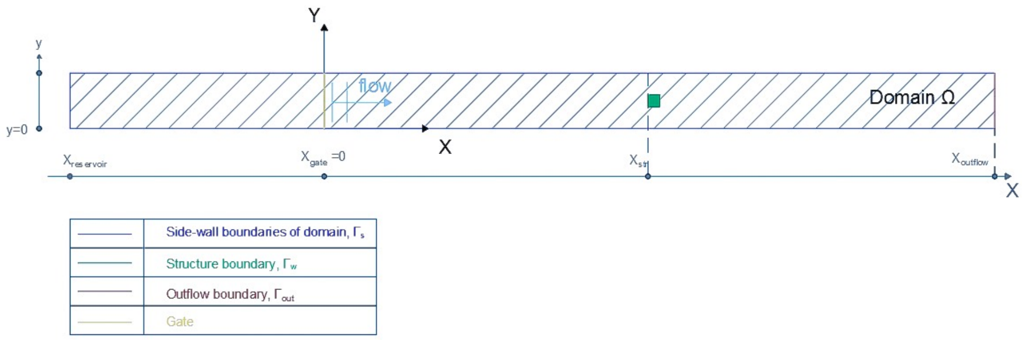

Figure 3.5: Indication of the boundary lines in the two-dimensional domain Ω.

3.6. Finite Element Method

The Finite Element Method is arising in engineering modeling for numerically solving differential equations such as fluid flows. It is particularly suitable for complex geometries and fluid-structure interactions (FSI) are one of these cases. Applying FEM, a subdivision of the whole domain is achieved into simpler parts that are represented by a set of elements [67]. In this way, different material properties can be included, and captivation of local effects would not be easy to be captured with a different approach. Then, all the sets of element equations are recombined into a global system of equations for the final calculation of the solution [67].

More specifically, the Galerkin finite-element method (FEM) is employed for the space discretization of the two-dimensional, shallow-water equations, which approximates the solution in a finite-dimensional subspace. The discrete approximation converts a continuous operator problem (such as the differential equations) to weak formulations, by applying basis functions over a given element [32]. The subdivision of the domain into elements is developed by the mesh generator. In each element, several nodal points are chosen,

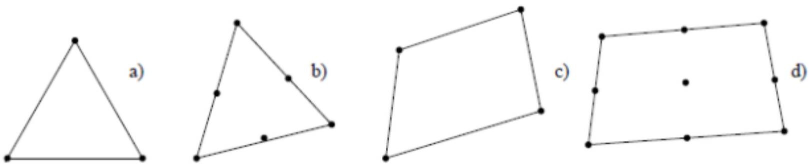

Figure 3.6: Elements in a 2D domain: a) linear triangle, b) quadratic triangle c)bi-linear quadrilateral d) bi-quadratic quadrilateral, [13].

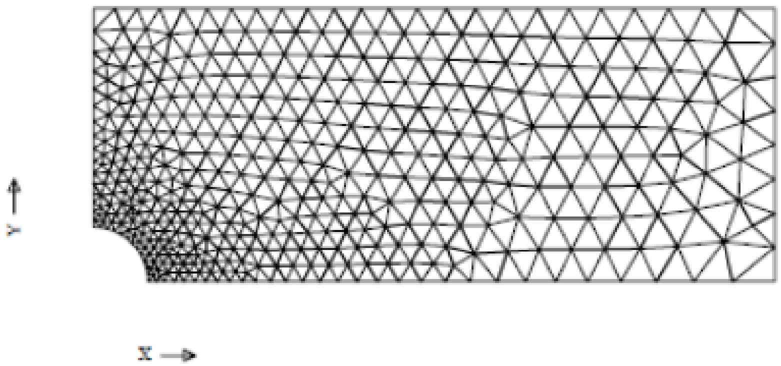

Figure 3.7: A typical depiction of a 2-Dimensional FE mesh generator [13].

and the unknown function is approximated by a polynomial. Figure 3.6 depicts the possible ways of introducing the elements in a two-dimensional domain and Figure 3.7 shows a typical example of a two-dimensional Finite Element mesh of triangular elements.

Spatial coordinates specify the location of a point in space. Both Lagrangian and Eulerian frame of reference is applicable to describe the flow field. At the Lagrangian specification of the flow field, the observer follows an individual fluid parcel as it moves through time and space, while the Eulerian specification of the flow field focuses on specific locations in space, through which the fluid flows, as time passes (the observer is watching the water passes the fixed locations) [5]. Eulerian mesh is used for the description of the water flow and a fixed grid is used to calculate the mass and momentum fluxes. The field is represented as a function of position x and time t. On the one hand, there is no mesh distortion as the mesh is fixed in space, but on the other hand, the water flows through the mesh and the nodes remained fixed, meaning that the boundary nodes and the material boundary may not coincide. Therefore, interface and boundary conditions present application difficulties in terms of accuracy [5].

The implementation of the Galerkin Finite Element Method follows the following steps [21]:

Step 1: Modeling of the flow by dividing the system into an equivalent one of many finite elements.

Step 2: Discretization of the domain Ω: n_e the elements at Ω_k for $k = 1, ... n_e$ and n_n the nodes.

Step 3: Approximation of the solution by piece-wise polynomials. Shape functions $N_i(x)$ of elements S_i. The shape function is 1 at $x = x_i$ and 0 otherwise. The solution is interpolated with the shape functions at the nodes.

$$u_h(x) \approx \sum_{i=1}^{n_n} N_i(x, y) \cdot u_i \tag{3.12}$$

The finite element method has the benefit of being able to formulate methods for basis functions of different orders. Higher orders for the basis functions give higher-order, accurate methods, which have the important benefit of being able to improve the accuracy for a given mesh.

Step 4: Weak form at each element k for the governing equations. The strong forms of the continuity and momentum equations are multiplied by virtual displacement and then they are integrated over the domain Ω_k. The procedure is described analytically in the next paragraph.

Step 5: Introduction of stabilized parameters and turbulence model to filter the turbulence phenomena, and normalize the discontinuities that are generated by unsteady flows of a shock wave, such as the dam-break wave, that is studied in the current research. Small-scale effects and discontinuities force the simulation to crash, and the above terms proved necessary for the functionality of the code and the reliable representation of the flow.

Step 6: Construction of global algebraic system for all the elemental contributions.

3.6.1. Weak form & Spatial discretization

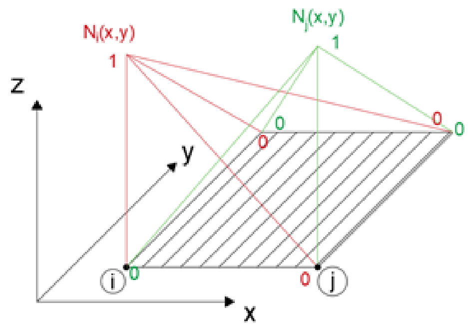

Figure 3.8: Indication of linear shape functions of an element of the mesh. Red line: the shape function of node i, and green lines: for node j.

The first step for the application of the FEM to solve the equations under the boundary conditions, is the discretization of the 2D domain Ω in n_e elements $\in \Omega_k$ for $k = 1,...,n_e$ and n_n number of nodes [21]. For spatial discretization, the discontinuous Galerkin Finite Element Method is employed, using weighting and shape functions for the triangulation of the domain Ω. Triangulation is a family of admissible and shape-regular triangulations of the domain [24]. The essence of the Galerkin method involves taking the weak form of the governing and finding the best solution to the problem given [84]. The weak forms of the model equations are required with the associated boundary and initial conditions to be discretized both temporally and spatially [40]. To do this, the strong forms, equations 3.1 and 3.4, in the form of vectors (continuity and momentum equations) are multiplied by a weight/test function, v and w, and integrated by parts over the domain for their transformation to weak forms ([13].

Finite element shape functions, $N_i(x)$, are typically piecewise continuous polynomial functions and they are associated with a node, i, Figure 3.8. The shape function is only non-zero on elements to which it is attached, [21]. In two dimensions, each of the unknown fields, velocities in the x, and y directions and the free surface perturbation field h, are interpolated using the polynomial shape functions and the value of the function at the specific node, [21].

$$u(x,y) \approx \sum_{i=1}^{n_n} N_i(x,y) \cdot u_i \tag{3.13}$$

$$v(x,y) \approx \sum_{i=1}^{n_n} N_i(x,y) \cdot v_i \tag{3.14}$$

$$h(x,y) \approx \sum_{i=1}^{n_n} \phi_i(x,y) \cdot v_i \tag{3.15}$$

Once the displacement field and its derivatives can be expressed, the weak forms at each element k can be derived by multiplying the strong forms (continuity equation and momentum equation) with the virtual displacement and then integrating over the domain Ω_k. The last step is the construction of the algebraic system for all the elemental contributions in order to solve for the unknown terms [21].

To proceed with the application of the method, test functions, namely w and v in the domain Ω are set for the unknown fields of h and u, respectively. The unit normal vector $\vec{n}$ of the boundary Γ is used for the integration by parts. For the Finite Element space, the order of the velocity field is set to one, meaning that the shape function is linear, while for the water elevation is assumed to be constant. This introduces a discontinuity in the system and the gradient of the water elevation ∇h will be zero since it is a constant function in time. In order to avoid this issue, integration by parts is implemented as follows:

- The continuity equation can be represented by the weak form:

$$\int_\Omega \left(\frac{\partial h}{\partial t} + \nabla \cdot (h+H) \right) w \, d\Omega = 0 \tag{3.16}$$

Applying integration by parts and multiplied by the weight function w, the weak form of the continuity equation is derived. The boundary integral Γ which appears after integration by parts should be understood as the boundary of all the elements (such as walls of the domain, walls of the structure, etc.).

$$=> \int_\Omega \frac{\partial h}{\partial t} w \, d\Omega - \int_\Omega (\nabla w \cdot (h+H) \cdot u) \, d\Omega + \int_\Gamma w \cdot (h+H) \cdot u \cdot n\Gamma) \, d\Gamma = 0 \tag{3.17}$$

Using the weight function v, the weak form of the equations of motion is also obtained:

$$\begin{aligned} &\int_\Omega \left(\frac{\partial u}{\partial t} + \nabla(u)' \cdot u + c_f \cdot \left(\frac{\| u \| u}{h+H} \right) \right) v - gh\nabla(v) \\ &+ v \cdot \left(\left(\nabla(u) + \nabla(u)' \right) - \frac{2}{3} \cdot \left(\nabla(u) \right) \cdot \mathbb{I} \right) : \nabla(v) \, d\Omega + \int_\Gamma gh \left(v \cdot n\Gamma \right) \, d\Gamma = 0 \end{aligned} \tag{3.18}$$

3.6.2. Discontinuity conditions for the wave height function

The water elevation is assumed to be a constant function in time and therefore, jumps will appear, which is an additional difficulty in resolving the code. The derivative of a constant value is zero, and to manage this problem integration by parts was proceeded. To deal with the jumps at each time step, the Λ triangulation is introduced as the edge in between two elements to enforce the continuity of fluid water elevation. The mathematical model is edited as below:

$$\begin{aligned} &\int_\Omega \frac{\partial h}{\partial t} w \, d\Omega - \int_\Omega (\nabla w \cdot (h+H) \cdot u) \, d\Omega + \int_\Gamma w \cdot (h+H) \cdot u \cdot n\Gamma) \, d\Gamma \\ &+ \int_\Lambda \left(mean(H+h) \cdot u \right) \cdot jump(w \cdot n\Lambda) + \gamma \cdot jump(h \cdot n\Lambda) \cdot jump(w \cdot n\Lambda) + mean(g \cdot h) \cdot jump(v \cdot n \cdot \Lambda) \, d\Lambda = 0 \end{aligned} \tag{3.19}$$

The above additional terms in the continuity equations were derived following the mathematical procedure that is presented below, assuming two different elements, a and b. In practice, it has a compensated effect as a penalty term, which introduces a smooth approximation to the Dirac delta function of the water elevation. A penalty method replaces a constrained optimization problem with a series of unconstrained problems whose solutions ideally converge to the solution of the original constrained problem. The following mathematical calculus was followed to deal with the discontinuities of the water elevation:

$$\begin{aligned} \sum_K \int \left(\nabla a \cdot b \, dK \right) &= \sum_K \left(- \int \left(\alpha \cdot \nabla b \right) dK + \int \left(\alpha \cdot b \cdot n \right) d\partial K \right) \\ &= - \int \left(\alpha \cdot \nabla b \right) dK1 + \int \left(\alpha \cdot b \cdot n_1 \right) dE - \int \left(\alpha \cdot \nabla b \right) dK2 + \int \left(\alpha \cdot b \cdot n_2 \right) dE \\ = - \int \left(\alpha \cdot \nabla b \right) dK1 - \int \left(\alpha \cdot \nabla b \right) dK2 &+ \int \left(\alpha^+ \cdot b^+ \cdot n^+ + \right) + \left(\alpha^- \cdot b^- \cdot n^- + \right) d\partial E \int \left(\alpha^+ \cdot b^+ \cdot n^+ + \right) + \left(\alpha^- \cdot b^- \cdot n^- + \right) d\partial E \end{aligned} \tag{3.20}$$

$$\int \left(\alpha^+ \cdot n^+ + \alpha^- \cdot n^- \right) \cdot \frac{1}{2} \cdot \left(b^- + b^+ \right) + \left(b + \cdot n^+ + b^- \cdot n^- \right) \cdot \frac{1}{2} \cdot \left(a^- + a^+ \right) \tag{3.21}$$

Where:

Jump of various α:	$[\![\alpha]\!]$	$= (\alpha^+ \cdot n^+ + \alpha^- \cdot n^-)$
Mean of various α:	$< \alpha >$	$= 1/2 \cdot (\alpha^- + \alpha^+)$
Jump of various b:	$[\![b]\!]$	$= (b^+ \cdot n^+ + b^- \cdot n^-)$
Mean of various b:	$< b >$	$= 1/2 \cdot (b^- + b^+)$

The above procedure is considered just for the discontinuities at the water elevation. Nevertheless, the terms do not act as a turbulence model and stabilized parameters need to be added to the numerical equations, too, in order to deal with the turbulent phenomena of the unsteady flow and with the fictitious oscillations that appear around discontinuities, jumps, or sharp gradients of the solution.

3.6.3. Turbulence Model

Simulation of the non-linear shallow water equations for turbulent, incompressible flow is highly challenging to be accurately solved due to the inherent difficulty to describe not only the flow but also its multi-scale nature (spatial and temporal scales) [20]. The model faces difficulty to deal with the stagnation points near walls. The velocity gradients are high close to the walls, which results in an error, and hence, unrealistic flow behavior. To avoid wall functions non-slip boundary condition is applied at the walls of the domain (zero velocity). Moreover, fictitious oscillations appear in the vicinity of discontinuities, jumps, or sharp gradients of the solutions of the weak formulation. Specifically for the dam break wave simulation, the impulse load of the instantaneous water release, which is comparable to a shock wave, is translated to a discontinuity in the initial condition. For problems that solutions have steep gradients and discontinuous solutions (like shock waves), higher-order schemes are generated called the "Gibbs effect" [58]. Therefore, discretized models of viscous fluids require a turbulent shock-capturing model to generate a stable behavior of the flow.

The stability of the standard Galerkin method is not ensured from a computational point of view. The simulation of the flow faces numerical stability problems for two main reasons. Firstly, instabilities related to singular perturbations require extremely fine meshes, unaffordable expensive for a computational procedure, leading to convergence as the resolution of the mesh is not fine enough to capture the turbulence effect [20]. Secondly, the existence of multiple variables of different natures needs to satisfy the compatibility conditions of the interpolation, which require significantly fine meshes, as well [20].

The common numerical methods to simulate the turbulence fluid flow are presented in the upcoming Figure 3.9. The three different ways are described as follows [10]:

- **Direct Numerical Simulation (DNS):** three-dimensional and time-dependent solution of the Navier-Stokes equations. The range of spatial and temporal scales of turbulence has to be resolved without any assumptions. For the simulation of turbulence in a flow, the eddy viscosity models are the most common to use since they can provide good results at a relatively low computational cost. However, full resolution direct numerical simulations (DNS) that capture the smallest scales in the flow are unaffordable for large Reynolds numbers (turbulent flow) [25].

- **Large eddy simulations (LES):** require a coarser grid than DNS and simulate only large eddies by removing small-scale occurrences with the help of filters. These turbulence models are well applied for transient solutions.

- **Reynolds-averaged Navier-Stokes equations (RANSE):** allow simulations at relatively low computational cost, receiving more general and averaged results of the flow. It is well-suited with steady-state solutions or slowly varying in time.

Practically, the space and time resolution can capture the main flow features. However, unsteady flows are paired with secondary flow phenomena leading to multi-scale water behavior. To incorporate these types of motions on the large scale and to control the undesired oscillations in the simulation, a turbulence model is introduced to add the molecular dissipation at the unresolved smallest scales of the flow and normalize the results, effectively [20]. A large-eddy simulation (LES) turbulence model is used. The turbulence model introduces terms, named stabilization terms, to filter the equations and making possible to ignore the smallest length scales which are the most computationally expensive to resolve [25]. In this way, the large eddy

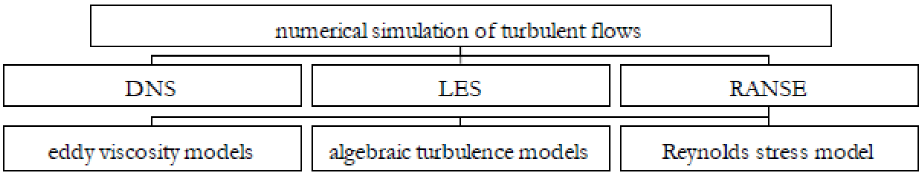

Figure 3.9: Simulation techniques of turbulent flows [10].

phenomena are captured by the simulation, the small-scale information is effectively removed, and hence, a stable solution can be obtained.

A combination of linear and non-linear stabilization techniques is used. The non-linear terms are active around shocks or discontinuities, where the order of accuracy needs to be sacrificed to improve the stability [20]. On the other hand, linear terms are effective for smooth areas. The terms that are added to the momentum and balance equations to stabilize the wave height and the velocity field are presented analytically in Appendix A, and they significantly improve the accuracy of the two-dimensional, viscous flow into the domain.

4

Validation of the Numerical Simulation

Careful verification and validation (V & V) are required before implementing model codes to study physical processes to assure that the numerical code fulfills is a true representation of reality [79]. Verification can be referred to as the process of determining whether the computational model represents the underlying mathematical model and its solutions, while validation is the process of determining the degree to which the model is an accurate representation of the real world [34]. The validation of the present simulation would give information concerning the accuracy of the unsteady flow using the Shallow Water Equations for the generation of a dam-break wave.

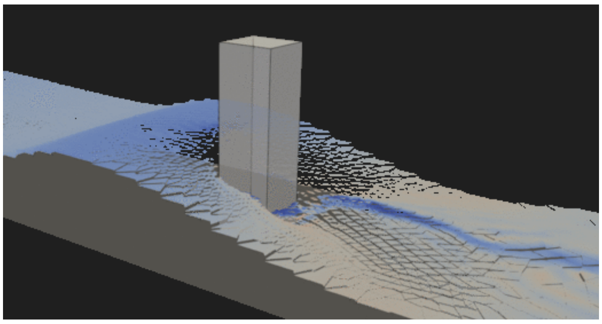

Figure 4.1: Validation of the flow around the impermeable structure

Specifically, in this chapter, the validation of the numerical solution is executed to verify that the chosen approach has the ability to simulate both the unsteady flow of the dam-break wave in the channel and the FSI with the isolated building. To validate the computation core for the two-dimensional dynamic flow, experimental data is needed to compare them with the calculated results of the simulation. The model is tested for its ability to replicate flood propagation (dam-break flow) over a wet and smooth bed surface. Two different experimental research, suitable for the declaration and the evaluation of the numerical shallow water model, are tested in the following sections. Initially, for the first experiment, the validation concerns the realistic generation of the dam-break flow without considering a structure. The time history of the bore surface elevation, derived from the numerical model, is compared to the experimental ones, at the different points of measurement (wave gauges locations). Afterward, the model is used for the simulation of the second physical experiment, which generates tsunami-like waves with the vertical-release technique. The time history of numerical and experimental water surface elevations and some averaged velocities in time are compared for validation. The second experiment is the main object of the current research. After verifying that the simulation can accurately replicate the experiment conducted in the absence of a building, an impervious structure was inserted to capture information about the behavior of the dam-break wave interacting with an impervious building. A detailed description of the validation is presented in the upcoming sections, containing the compared results and the conclusions drawn from them.

4.1. Setup of the first Validation Simulation

As a first case, the experimental research of dam-break waves is used, which is conducted by Buitelaar (2022) [12] at the Hydraulic Engineering Laboratory of the Technical University of Delft during his MSc Thesis. The study generated dam-break waves through a lift-gate and a reservoir with a depth $d_0 = 0.4m$. The measurements of the water levels over time were taken downstream of the gate in the channel, where the induced wave propagates, Figure 4.3. A representation of the generated dam-break wave, after the sudden release of the stored water, is depicted in Figure 4.2.

Figure 4.2: A qualitative indication of the wave propagation downstream and upstream, when the gate is removed ($t > 0$).

For the validation of the numerical code, only a smooth, horizontal bed and a wet bed downstream of the dam-gate for different initial water depths were considered. In Figure 4.3, the test's setup is illustrated, paired with the indication of the six different gauging points (ADMs), that were used at the laboratory to measure the water depths in time. These were then ensemble-averaged over multiple repetitions. The coordinates of the measuring points are listed in Table 4.1. The data for the ensemble-averaged water depths over time was used for the numerical validation at the stations ADM4, ADM5, and ADM6.

Gauges	X (m)	Y (m)
ADM1	0.2	0.2
ADM2	1.5	0.2
ADM3	2.9	0.2
ADM4	4.0	0.2
ADM5	5.0	0.2
ADM6	6.0	0.2

Table 4.1: Positioning of the gauges from the gate ($x = 0$) for the experimental dam-break flow.

The physical tests were conducted on the flume in the Water Lab of TU Delft with a total length of 14.30m, a width of 0.40m, and a height of 0.40m. The water flows from left to right in a wedge that expands from the dam location, $x = 0$, and downstream. At the right edge of this wedge, the initial volume of water is $1.295m^3$. Hence, the geometrical characteristics of the simulation upstream of the gate are considered with a length of 8.094m, a width of 0.40m, and an impounded depth of 0.40m. Mention should be made about the different lengths of the reservoir compared to experiment one, at the right-hand side (RHS) of the gate/dam. The noted difference in the length upstream of the gate is relevant to the geometrical characteristics. The walls of the flume at the laboratory are inclined upstream of the gate. The lateral walls of the numerical simulation are considered parallel to the flow and therefore, a larger upstream length is required to store the same volume of water and mimic accurately the experiment. Moreover, due to the concrete plywood layer of 0.06 m downstream of the gate, the initial water depth upstream is considered $\Delta h = 0.40 - 0.06 = 0.34m$ for the simulation. Finally, a downstream length of 30m from the gate, instead of 7.8 m of the real flume, was used to avoid modeling errors due to the reflection effect.

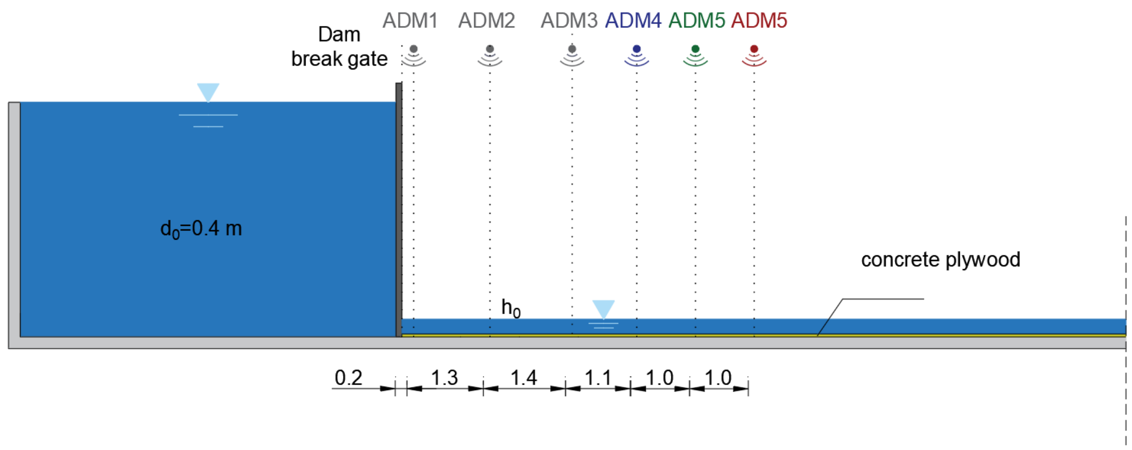

Figure 4.3: The numerical setup of the experiment at $t = 0s$, where the gate is closed, separating the stored water at the reservoir from the downstream canal.

4.1.1. Test cases & Domain discretization

Three different cases of initial water depth downstream of the gate were considered for validation, and the data were extracted at the measuring points of ADM4, ADM5, and ADM6. The measured water levels at the mentioned stations are compared with the numerical results for the 3 different initial depths at the channel:

(I) $h_0 = 0.035m$

(II) $h_0 = 0.025m$

(III) $h_0 = 0.050m$

The computational domain is discretized using GMSH in both horizontal directions, and the triangulation of the domain is depicted in Figure 4.4. The grid size is defined according to the followings:

- Y-direction: n_y is the number in which the y-direction of the domain is subdivided.
- X-direction: $n_x = a \cdot n_y$, the parameter α was set equal to the ratio of the horizontal length of the domain in the x direction, devided by the width of the domain in the y direction: $\alpha = \frac{36.5}{0.4} = 91.25$.

Convergence analysis for the variables is performed in order to simulate the flow motion as accurately as possible and to verify the correctness of the model. The domain is divided into different elements to identify the optimum solution. Trials for different grid sizes for both directions x, y are tested: 0.2, 0,1 and 0.05 m. Between the grid size of 0.1 and 0.05m, the results are identical, at least for the examined time scale. Therefore, the grid size of $\Delta x = \Delta y = 0.1m$ is considered sufficient for validity. The sensitivity analysis is presented in Appendix B.

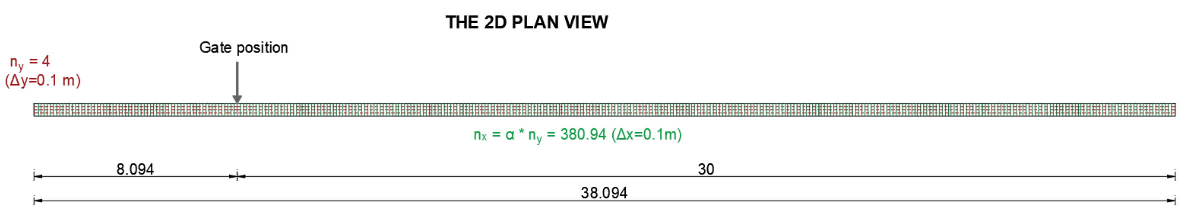

Figure 4.4: Plan view of the 2D domain, and discretization with a grid size of $\Delta x = \Delta y = 0.14$ m for the 2D.

4.1.2. Initial water depth of 35 mm at the channel

A total of 11 dam-break waves tests were conducted in the laboratory for these specific configurations. The initial conditions include a wet bed with an initial water depth of 0.035m and an impoundment water level of 0.4m in the reservoir, downstream of the gate. The experimental results are presented for the 3 measuring points ADM4, ADM5, and ADM6 with blue, green, and red lines, respectively. The water surface profiles are derived, and they are synchronized to one start time. The average interval time between ADM4 and ADM5 is $0.504s$ while the average time from ADM5 to ADM6 is $0.522s$. The results are comparable until the moment that reflection is noticeable in the experimental results. The moment of reflection for each case is distinct by the sharp increase in the water elevation and the sudden deviation from the downward trend of the curve. The reflection is avoided in the simulation by the extension of the domain. Therefore, when the water depth evolution in time is affected by the influence of the reflected wave, the results are not comparable anymore.

The variables that influence the behavior of the wave height evolution in time are listed below:

- The resistance factor c_f, regarding the material of the bottom of the canal,
- the kinematic viscosity ν_t, depending on the type of liquid,
- the geometrical characteristics of the domain, which are set according to the experimental setup.

The two first parameters, namely the resistance factor and the kinematic viscosity, contribute to the sensitivity of the model, as the determination of their values involves high uncertainty. The numerical results of the model were derived assuming constant values of the friction factor and the kinematic viscosity for the whole domain.

A) Dimensionless resistance factor c_f

Flow friction is a key component of studying water flows, and is one of the most important research topics in hydraulic engineering. The shear stress on the bed is given by the following quadratic friction term, for a depth-averaged turbulent flow, [72].

$$\tau = c_f \cdot \rho \cdot U^2 \tag{4.1}$$

The resistance coefficient c_f can be computed with three different formulas:

- The Chezy formula:

$$c_f = \frac{g}{C^2} \tag{4.2}$$

Where C is the Chezy's coefficient $[m^{1/2}/s]$

- The Manning formulation. The roughness coefficient in the Manning formula represents friction applied by the channel and changes in the geometry of the cross-section, water level, and flow velocity:

$$c_f = \frac{g \cdot n^2}{R^{1/3}} \tag{4.3}$$

Where n is the Manning coefficient $[m^{1/3}/s]$, and R, is the hydraulic radius. The values of Manning's coefficient vary from 0.01 to 0.05 for a very smooth bed (concrete) to a rough bed (rocks), [52].:

$$C = \sqrt{\frac{g}{c_f}} = 18 \cdot \log(\frac{12 \cdot R}{k_s}) \tag{4.4}$$

Where k_s is the Nikuradse roughness length $[m]$

For the quadratic friction law to be valid, the flow should be turbulent. The Reynolds number indicates if the flow is turbulent or laminar. The flow is turbulent if the Reynolds number is larger than 1,000 to 2,000. Otherwise, it is laminar, and the equation (4.1) can not be used. Reynolds numbers will be calculated for all the tested cases. The dam-break wave is an unsteady flow with a lot of turbulence and this is proven by the high estimated Reynolds numbers for all the cases. For this specific case:

$$Re = \frac{u_m \cdot R}{\nu_t} = \frac{1.52 \cdot 0.16}{10^{-6}} = 243,200 > 2,000 \rightarrow \text{turbulent flow} \tag{4.5}$$

Where u_m, is the depth-averaged profile velocity, R is the hydraulic radius that can be replaced by the water depth, and ν_t is the kinematic viscosity of water. The velocity can be computed by Stokes' formula (1957) as follows:

$$u = \frac{dx}{dt} \cdot \left(1 - \frac{h_0}{h_1}\right) = 1.95 \cdot \left(1 - \frac{0.035}{0.16}\right) => u_m = 1.52 m/s \tag{4.6}$$

Where, the average interval time between the stations ADM4-ADM5 is calculated equal to $0.5043s$ and from ADM5 to ADM6 is $0.522s$. The distance between them is $2m$, thus, $\frac{dx}{dt} = 1.95 m/s$. The initial water depth $h_0 = 0.035m$ is with zero initial velocity and h_1 is the height of the bore from the measured water depths.

The Manning formula is used to calculate the resistance factor. The friction formula is empirically based on simplifications, which contributes to an error in the replication of the real conditions. Manning's equation is accurate for straight or slowly varying channels, although it does not calculate energy losses.

Thus, Manning value, n, is set equal to $0.015 s/m^{1/3}$ according to for [68] a relatively smooth bottom material of concrete plywood plates (wooden forms) used at the physical experiment, (Manning values for different materials are provided in Table of the Appendix E. The numerical results were derived by using this calculated bottom friction value for the total domain.

$$c_f = g \cdot \frac{n^2}{R^{1/3}} = 9.81 \cdot \frac{0.015^2}{0.03^{1/3}} => c_f = 0.0071 \tag{4.7}$$

A sensitivity analysis was performed, using different values, Appendix C.

B) <u>Kinematic viscosity ν_t</u>

Kinematic viscosity $\nu_t = \frac{\mu}{\rho}$, is given as the dynamic viscosity, μ, per unit density of the fluid and it has units m^2/s in SI. It is a measure of a fluid's internal resistance to flow under gravitational forces (Machinery Lubrication 2021). The kinematic viscosity of water at 20°C is $10^{-6} m^2/s$. The calculations will proceed with this value.

The evolution of the water depth in time was used for the validation of the numerical simulation. The results were analyzed and compared at the 3 different locations ADM4, ADM5, and ADM6 with a distance of 4m, 5m, and 6m respectively, from the gate. Additionally, for the computation of the numerical results, the grid size in the x and y direction is prescribed, dx and dy, as well as the time step, dt, and the total duration of the simulation T, regarding Appendix B. The calculated friction coefficient c_f, and the kinematic viscosity of water ν_t are also inserted in the code. The values of the aforementioned inputs, that are used in the simulation, are presented in Table 4.2:

dx [m]	dy [m]	dt [s]	T [s]	c_f	ν_t $[m^2/s]$
0.1	0.1	0.05	20	0.0071	10^{-6}

Table 4.2: Input for the computation of the numerical results for the wet bed of 35 mm initial water level.

The time history of the water elevation is compared with the experimental data in Figure 4.5 below.

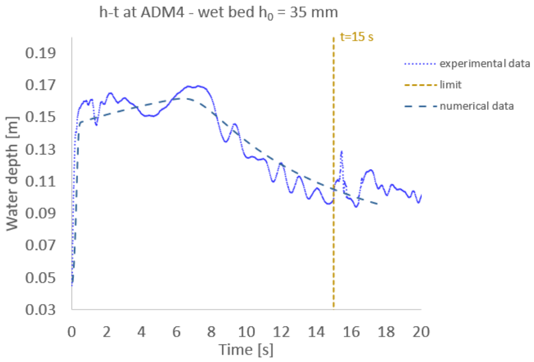

(a) ADM4

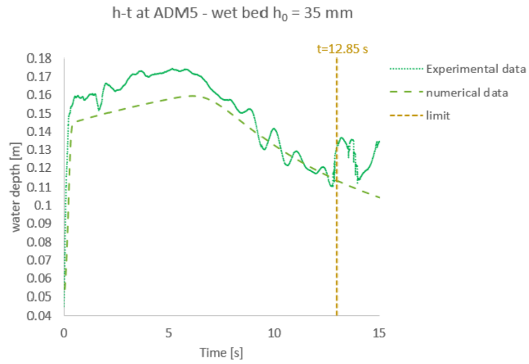

(b) ADM5

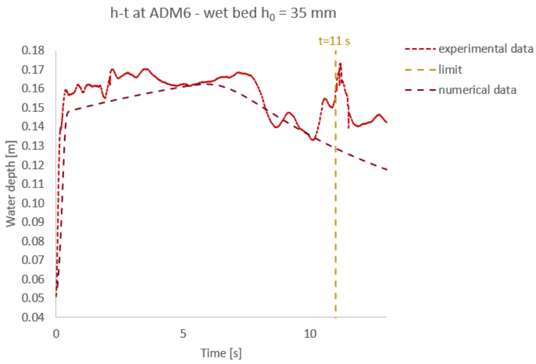

(c) ADM6

Figure 4.5: Comparison of the evolution of the water depth in time of numerical data with the experimental data for an initial water depth of 35mm downstream of the gate, at the three different measuring points ADM4, ADM5, and ADM6, respectively.

4.1.3. Initial water depth of 25 mm at the channel

dx [m]	dy [m]	dt [s]	T [s]	c_f	ν_t $[m^2/s]$
0.1	0.1	0.05	20	0.0079	10^{-6}

Table 4.3: Input for the computation of the numerical results for the wet bed of 25 mm initial water level.

In this subsection, the case of a wet bed with an initial water depth of 0.025m and an impoundment water level of 0.4m is examined. The domain is discretized in time and space and the values are presented in Table 4.3. For the validation, once again the water levels at the three measuring points ADM4, ADM5, and ADM6 are derived from the numerical code and compared to the experimental data. The calculation of the required parameters and the friction coefficient for this specific case is computed, similarly to the previous case, considering the new geometric characteristic. The calculations were repeated and the results are presented in the Table 4.4.

variables	notations	values
velocity	u	1.61 m/s
Reynolds number	Re	209,300
Hydraulic radius	R	0.022 m
friction coefficient	c_f	0.0079

Table 4.4: Calculated variables for 25mm initial water depth.

Inserting the different values into the model, the simulation is running again for the case of the smallest initial water depth, 25mm, in the channel. After deriving the numerical results of the water surface elevation in time, they are plotted, and paired with the experimental ones for the three different points of interest: (a) ADM4, (b) ADM5, and (c) ADM6, see Figure 4.6

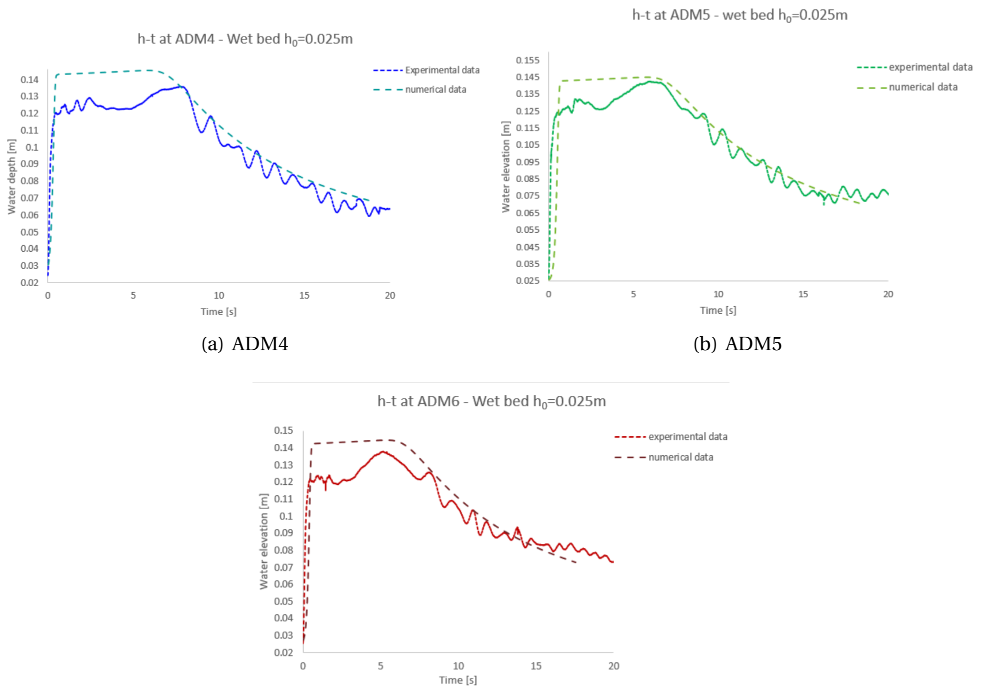

(a) ADM4
(b) ADM5
(c) ADM6

Figure 4.6: Comparison of the water depth in time at the three different measuring points ADM4, ADM5, and ADM6, respectively.

4.1.4. Initial water depth of 50 mm

The last validation test for this physical experiment was done for the case of a wet bed with an initial water depth of 0.05m, and an impoundment water level of 0.4m as in all tested cases for this experiment. The analysis was conducted again for the comparison of the water elevation in time, at the 3 different measuring points. The input values of the numerical simulation are given in Table 4.5. Additionally, the calculation for the friction coefficient is repeated and the results are presented in the Table 4.6.

dx [m]	**dy [m]**	**dt [s]**	**T [s]**	c_f	$\nu_t\ [m^2/s]$
0.1	0.1	0.05	20	0.00645	10^{-6}

Table 4.5: Input values for the wet bed with an initial water depth of $h_0 = 50mm$.

variables	notations	values
Velocity	u	1.32 m/s
Reynolds number	Re	197,984
hydraulic radius	R	0.04 m
Friction coefficient	c_f	0.00645

Table 4.6: Calculation of variables for the wet bed of 50mm initial water depth.

The numerical solution, that is used for the comparison with the experimental data, is presented in the next graphs at the three different points of interest, (a) ADM4, (b) ADM5, and (c) ADM6, Figure 4.7. The results are comparable with the experimental data until the limit line which indicates the moment that reflection affects the water elevation. For $t > t_{limit}$ curves cannot be compared anymore:

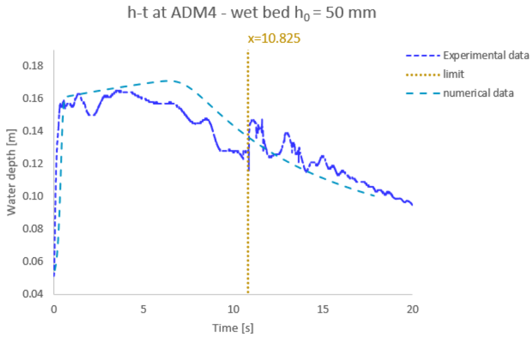

(a) ADM4

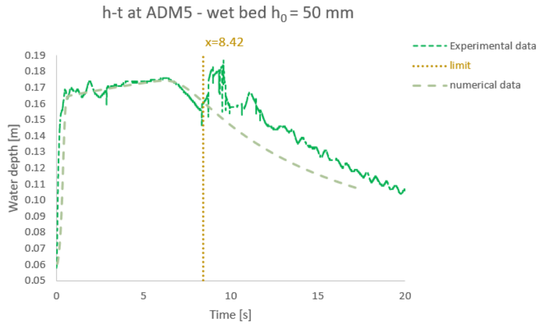

(b) ADM5

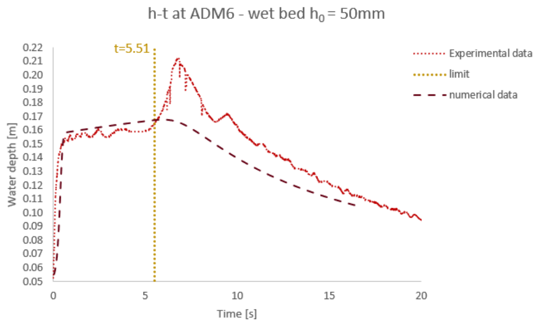

(c) ADM6

Figure 4.7: Comparison of the evolution of the water depth in time of numerical data with the experimental data, at the three different measuring points ADM4, ADM5, and ADM6, respectively, for an initial water depth of 50mm downstream of the gate.

4.1.5. Remark of the results of the first test

The results derived by the numerical approach represent quite well the experimental data, and the flow is simulated considerably accurately. Although numerical results agree fairly well with the experimental ones, some discrepancies appear in the tested gauges. First and foremost, some general conclusions are presented regarding the overall comparison of the results. For all the gauges and the different initial water depths in the channel, there is no delay in the propagation of the wavefront. The wave celerity is computed accurately with the one derived from the experimental work, for all the different cases.

Checking the wet-bed cases separately, the following conclusions can be drawn:
For the initial water depth of 35mm there is a good agreement between numerical and experimental results for all three gauges that were checked. The initial shocks and their arrival times are captured accurately, and the averaged water depths correspond well to the experimental values. The validity of the measurements is ensured for this case.

For the initial water depth of 25mm, the water elevation profiles captured well the propagation speed of the wave. Nevertheless, there is a general overestimation of the water depth values. The discrepancies in the water elevation could be caused by the relatively low initial water depth in the channel. The lowest the initial water depth in the channel, the closest the water depth to zero, and therefore, to the dry bed case, which cannot be well reproduced by the numerical simulation.

For the initial water depth of 50mm, which is the last tested case, the results showed significant accuracy with the experimental data. The comparison is valid by the time reflection appears on the experiment results. The numerical domain is extended to avoid reflection for a duration of 20s. Therefore, results after reflection of the recorded values from the laboratory are not comparable anymore.

4.2. Setup of the second Validation Simulation

The second validation test for the numerical simulation is the model that will be used further, for the study of the impact of wet bed bores on impervious structures. The experimental study, which was carried out by Wüthrich (2018) [86] at Ecole Polytechnique Fédérale de Lausanne (EPFL) in Switzerland, focused on the generation of both surges and bores by the vertical release of a stored water volume [87–89]. The laboratory research generated tsunami-like waves by the vertical release technique on a scale of 1:30. The aim was to simulate an unsteady flow at a channel $15.5m$ long, $1.4m$ wide, frictionless, and rectangular. Thus, the numerical domain is set accordingly: $\Omega = (0.0, 15.5m) \times (0.0, 1.4m)$ with a scaling of Froude similitude of 1:30. Seven Ultrasonic distance Sensors (US) were used to investigate the profiles of the propagating waves and the run-up height. The setup of the experiment and the location of the sensors are depicted in Figure 4.8. A set of wet bed bores will be tested in the upcoming sections and the results are validated with and without considering a structure.

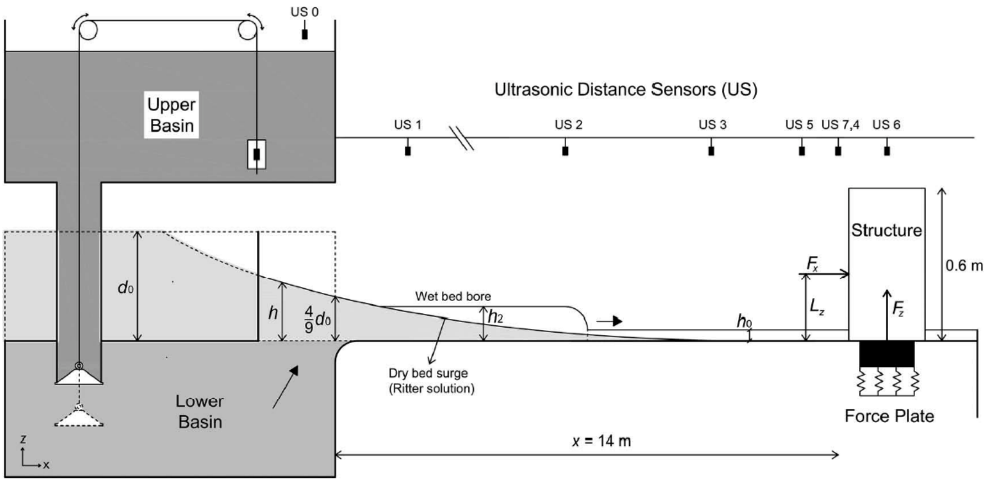

Figure 4.8: Experimental set-up for the generation of tsunami-like waves through the vertical release technique [89]

In the following table, the coordinates of the locations of the instruments from the flume inlet are given, for all the 7 sensors, 4.7. The main measuring points that are used for the research are the US4, US5, and US7.

Gauges	X (m)	Y (m)
US1	2.0	0.7
US2	10.10	0.7
US3	12.10	0.7
US4	14.15	1.125
US5	13.35	0.7
US6	14.15	0.7 (top of the building)
US7	13.85	0.7

Table 4.7: Positioning of the gauges from the flume inlet, for the experimental vertical release technique.

A total of 45 tests were conducted for 12 standard waves, according to the experimental methodology. The vertical release of $7m^3$ volume from an upper reservoir into a lower basin generated both wet bed bores and dry bed surges in the downstream channel, Figure 4.8. The experimental results showed that the behavior of these induced unsteady flows was similar to dam-break waves.

For the validation of the present research, four of the total wet bed cases, that are included in the red box in Table 4.8, are checked with the numerical simulation, to ensure whether the numerical flow, without considering a structure yet, does replicate well the measurements. After the validation, an impervious, rigid structure is introduced to focus on the flow around it and to study the load impact of the dam-break wave on the boundaries of the structure.

4.2.1. Validation for the case without structure

For the case with an absence of a building into the domain, the hydrodynamic properties, measured during the experiment, are presented in Table 4.8 and the numerical simulation will focus on the cases included in the red box. For this experiment different initial volumes are used on the upstream side of the dam. And for each impounded water depth, d_0, two different initial water depths, h_0, are tested. The inserted parameters for the numerical simulation are the kinematic viscosity, which is set equal to the kinematic viscosity of water $v_t = 10^{-6} m^2/s$, and the friction coefficient, which is computed for each case and is assumed to be constant over the total domain. The material of the bottom is made of wood, and the pieces are connected with joints providing extra roughness to the system. The normal value of Manning's coefficient for wood material is $n = 0.012 s \cdot m^{-1/3}$, and due to the additional roughness, the maximum value of Manning's coefficient for wood is chosen from the Table in the Appendix E. Thus, Manning's coefficient is defined as equal to $n = 0.02 s \cdot m^{-1/3}$ over the domain. The computation of the friction coefficient c_f is a function of water depth and therefore it is computed for each tested case separately since the initial water depths of the channel differ. For each case respectively, the variables are specified in tables, and the experimental data are plotted together with the numerical ones for comparison.

Bed type -	Impounded depth $d_0[m]$	Initial water depth $h_0[m]$	Front celerity $u[m/s]$	Max wave height $h_{max}[m]$	Repetitions -
Wet	0.82	0.03	2.81	0.232	5
Wet	0.82	0.05	2.75	0.260	7
Wet	0.63	0.03	2.52	0.206	3
Wet	0.63	0.05	2.44	0.224	3
Wet	0.40	0.03	1.97	0.162	3
Wet	0.40	0.05	1.93	0.260	

Table 4.8: Hydrodynamic properties of the experimental tested waves without the presence of the building [87].

4.2.2. Impoundment water depth of 0.82 m

For the numerical simulation, the case of impounded water depth of 0.82m (upstream of the gate) and initial water depth of 30mm and 50mm in the channel downstream of the gate are studied. The experimental data were derived at the points of measurement listed below, for the initial water of $d_0 = 30mm$:

(a) US2(10.10, 0.7)

(b) S3(12.10, 0.7)

(c) US5(13.35, 0.7)

(d) US7(13.85, 0.7)

For the rest of the study cases, the results are derived and compared with the experimental data at the most distant point from the gate, US7(x=13.85, y=0.7). This point is of greatest interest because the structure will be inserted close to this location. Comparison between the results will be accomplished with and without considering the impervious building to study the effect of the building on the flow. Moreover, the focus closer to the structure will be more efficient and time-saving.

(i) **Initial water depth of 30mm in the channel**

At point US7(x=13.85, y=0.07), additionally to the water elevation, the data from the time history of the depth-averaged velocity profile are available and are used for the validation. The input values in the simulation and the calculated parameters are presented in the Tables 4.9 and 4.10, respectively. The final results for the initial water depth of 0.03m in the channel, are presented in Figure 4.9.

dx [m]	dy [m]	dt [s]	T [s]	c_f	ν_t [m^2/s]
0.14	0.14	0.05	20	0.0127	10^{-6}

Table 4.9: Input values for the wet bed with an initial water depth of $h_0 = 50mm$.

variables	notations	values
averaged velocity	u	2.09 m/s
averaged water depth	$h_{av.}$	0.213 m
wavefront celerity	u_c	2.81 m/s
Reynolds number	Re	60,610
Hydraulic radius	R	0.029 m
friction coefficient	c_f	0.0127

Table 4.10: Calculated variables for the wet bed of impounded depth of $d_0 = 0.82m$ and initial water depth $h_0 = 30mm$.

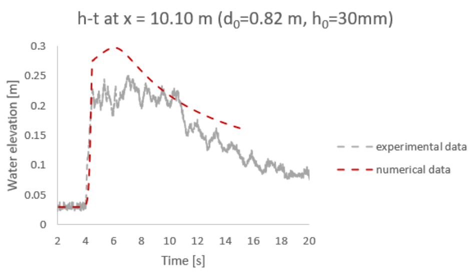

(a) height vs. time at 10.10 m

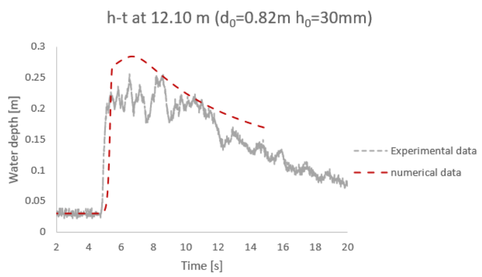

(b) height vs. time at 12.10 m

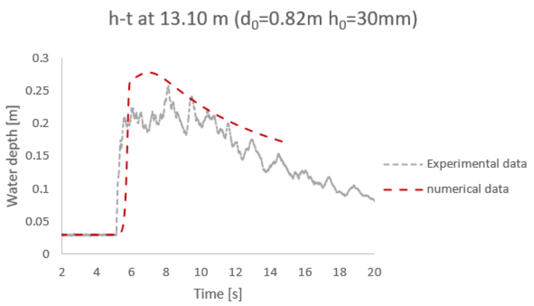

(c) height vs. time at 13.10 m

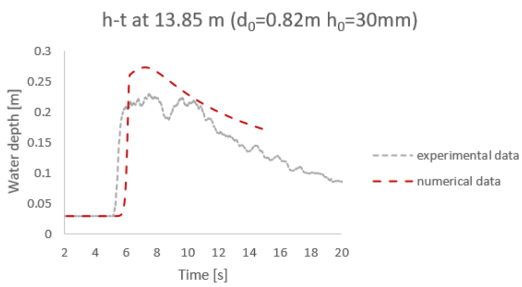

(d) height vs. time at 13.85 m

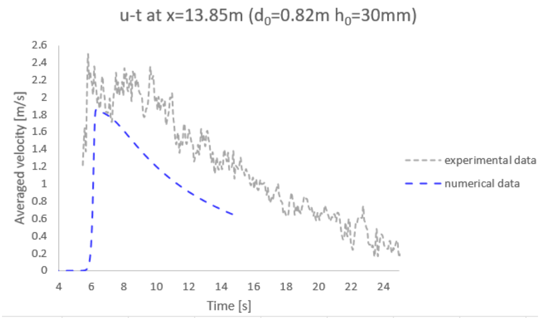

(e) velocity vs. time at 13.85 m

Figure 4.9: Comparison of numerical results with the experimental data for the initial case of $d_0 = 0.82m$ and $h_0 = 30mm$.

(ii) **Initial water depth of 50mm in the channel**

The input values in the code are presented in the Tables 4.12 and 4.11, respectively. The results for the initial water depth of 0.05m in the channel, are presented in Figure 4.10.

dx [m]	dy [m]	dt [s]	T [s]	c_f	ν_t $[m^2/s]$
0.14	0.14	0.05	20	0.011	10^{-6}

Table 4.11: Input values for the wet bed with an initial water depth of $h_0 = 50mm$.

variables	notations	values
velocity	u	1.91 m/s
averaged water depth	$h_{av.}$	0.25 m
wavefront celerity	u_c	2.755 m/s
Reynolds number	Re	89770
Hydraulic radius	R	0.047 m
friction coefficient	c_f	0.011

Table 4.12: Calculation of variables for the wet bed of impounded depth of $d_0 = 0.82m$ and initial water depth $h_0 = 50mm$.

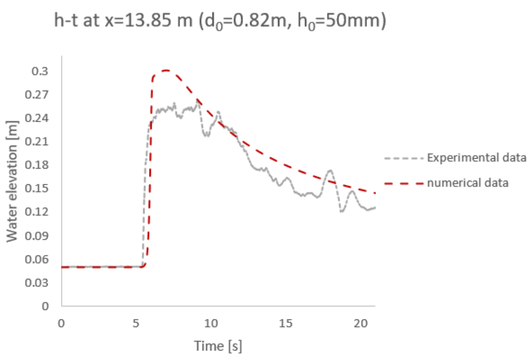

(a) height vs. time

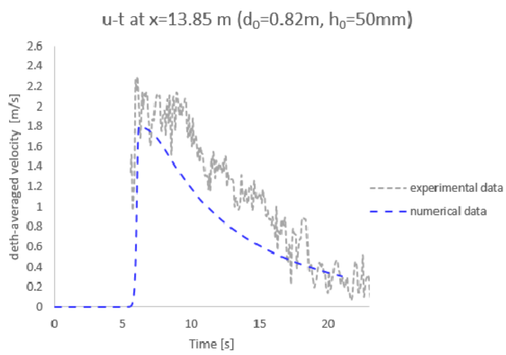

(b) velocity vs. time

Figure 4.10: Experimental data derived at the laboratory, for the case of impounded depth of $d_0 = 0.82m$ and initial water depth at the channel of $h_0 = 50mm$

4.2.3. Impoundment water depth of 0.63 m

Moreover, the case of impounded water depth of 0.63m and initial water depth of 30mm and 50mm are studied. The experimental data were derived at the measuring point D($x = 13.85$, $y = 0.7$). The wave front celerity at this point is $2.52 m/s$. The simulation is programmed to replicate these cases, as well, and the results are derived for point D. The results are presented in the upcoming Figure 4.11.

(i) **Initial water depth of 30mm in the channel**

dx [m]	dy [m]	dt [s]	T [s]	c_f	ν_t $[m^2/s]$
0.14	0.14	0.05	20	0.0127	10^{-6}

Table 4.13: Input values for the wet bed with an initial water depth of $h_0 = 50mm$.

variables	notations	values
velocity	u	1.60 m/s
averaged water depth	$h_{aver.}$	0.182 m
wavefront celerity	u_c	2.52 m/s
Reynolds number	Re	46400
hydraulic radius	R	0.029 m
friction coefficient	c_f	0.0127

Table 4.14: Calculation of variables for the wet bed of impounded depth of $d_0 = 0.82m$ and initial water depth $h_0 = 30mm$.

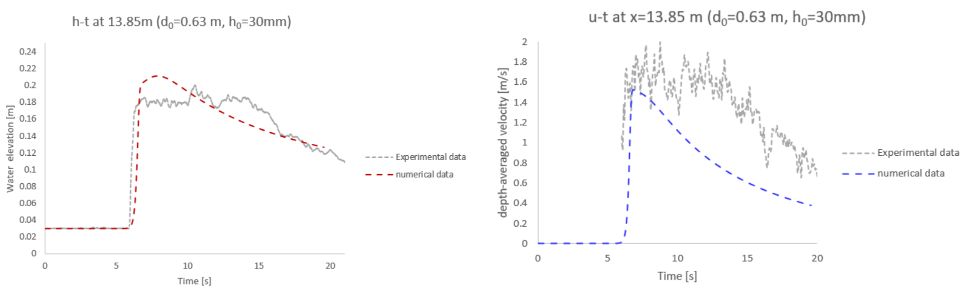

(a) height vs. time

(b) velocity vs. time

Figure 4.11: Comparison of the results, for the case of $d_0 = 0.63m$ and $h_0 = 30mm$.

(ii) **Initial water depth of 50mm in the channel**

dx [m]	dy [m]	dt [s]	T [s]	c_f	ν_t $[m^2/s]$
0.14	0.14	0.03	20	0.011	10^{-6}

Table 4.15: Input values for the wet bed with an initial water depth of $h_0 = 50mm$.

variables	notations	values
velocity	u	1.48 m/s
averaged water depth	$h_{aver.}$	0.214 m
wavefront celerity	u_c	2.44 m/s
Reynolds number	Re	69560
hydraulic radius	R	0.047 m
friction coefficient	c_f	0.011

Table 4.16: Calculation of variables for the wet bed of impounded depth of $d_0 = 0.82m$ and initial water depth $h_0 = 30mm$.

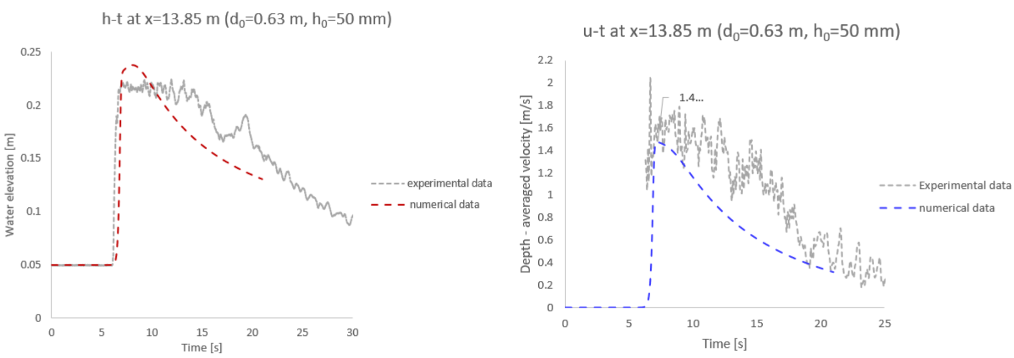

(a) height vs. time (b) velocity vs. time

Figure 4.12: Experimental data derived at the laboratory, for the case of impounded depth of $d_0 = 0.63m$ and initial water depth at the channel of $h_0 = 50mm$

4.2.4. Remark of the second validation test without a structure

More inconsistencies are noticed from the comparison between numerical and experimental results for the second experiment than from the study of Buitelaar (2022) [12]. The methods that are used for the generation of unsteady flows are different. Specifically, the physical experiment used the vertical release technique, while the numerical model simulates the dam failure technique. However, the experimental studies [87, 88] showed that the behavior of these two flows was similar. Nevertheless, the results of the assessment can be considered sufficient, regardless of the method of use. In this subsection, the results are discussed and the differences are explained. Some changes to the model setup compared to the experimental one were deemed necessary to ensure the reliability of the results.

It is noticeable that the water is depleted faster in the numerical model, while in the experiment, the sustained hydrodynamic phase lasts longer. This can be justified by the different methods of the generation of the wave. The instantaneous break of the dam leads to a more abrupt shock wave than the vertical release of the water. Another reason could be supported by the generation of the aerated front at the experimental wave. More specifically, in the experiment, there was a fully aerated wavefront, which increased the turbulence and reduce the propagation speed. Since the aerated wavefront is not reproduced by the numerical model, this could justify the faster reduction of water elevation compared to the numerical results. To deal with these discrepancies, a larger volume is required for the simulation to maintain the same loading duration between experiments and the model.

The best correlation between experimental and numerical results appeared for the case of an impounded water depth of $d_0 = 0.63m$ in the reservoir. For that reason, in the presence of the impervious structure in the domain, the initial water levels of this case were considered for achieving a higher validation level of accuracy.

4.3. Introduction of an impervious structure to the domain

In the case of considering a structure at the domain, the difference is even higher due to the hydraulic jump upstream of the structure. Therefore, a higher initial volume is used with respect to the experimental one to achieve a better correlation to the results.

In this chapter, the final numerical simulation of the dam break flow against a self-standing building is performed. The building according to the experiment [86] is located at a distance of 14m from the gate with scaled dimensions of $0.3 \times 0.3 \times 0.3$ [m]. A geometrical scale of 1:30 is assumed such that this building corresponded to residential houses of $9 \times 9 \times 9$ [m], commonly observed on coastlines subject to tsunami hazards. The structure is placed 14 m from the gate-dam and in the middle of the channel's width ($14.0 \leq x \leq 14.3$ and $0.55 \leq y \leq 0.85$). The experimental setup is depicted in Figure 4.8 and the numerical simulation is represented in the Figure 4.13.

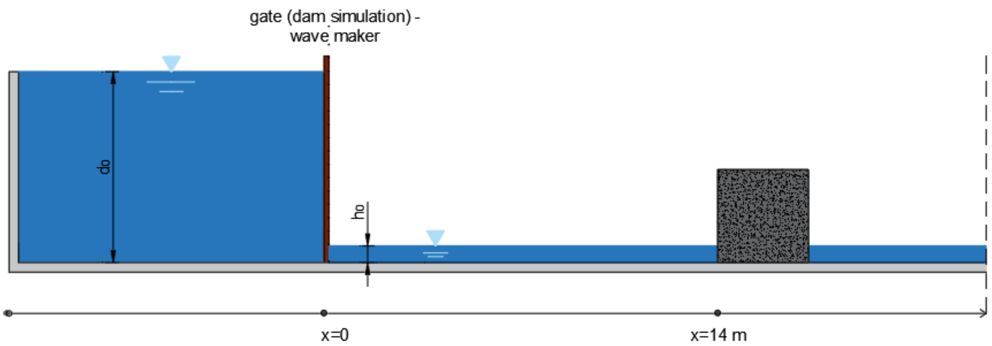

Figure 4.13: Numerical setup for the generation of tsunami-like waves, regarding the vertical release experiment. [89].

4.3.1. Model set up

For the numerical simulation, the case of impounded water depth of 0.63m (upstream of the gate) and initial water depth of 30mm in the channel downstream of the gate are studied. The experimental data were derived at the 3 points of measurement listed below, for the initial water of $d_0 = 30mm$. The gauges' locations were used for the simulation as well. Two of them, US5 and US7, are placed halfway of the width's channel and upstream of the structure, and the third one, US4, measures the data halfway between the building side and the sidewall of the channel, Figure 4.14:

a) US5(13.35, 0.7)
b) US7(13.85, 0.7)
c) US4(14.15, 1.125)

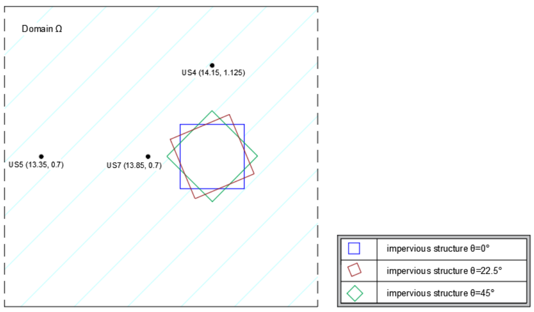

Figure 4.14: Considered cases for the validation and the location of the examined points around the structure.

- **Domain & discretization**

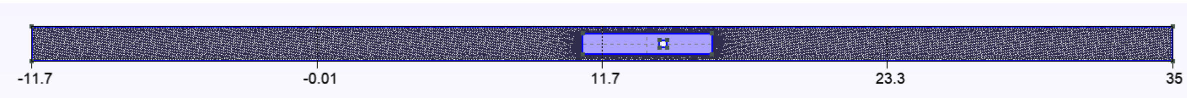

Figure 4.15: Domain discretization using GMSH. Closer to the structure the resolution is defined $n_x = n_y = 0.03m$, and at the rest of the domain is $n_x = n_y = 0.1m$

nodes	elements	dt [s]	T [s]	c_f	ν_t $[m^2/s]$
12,875	26,100	0.05	20	0.011 or 0.0127 → depending on the initial state	10^{-6}

Table 4.17: Input values for the wet bed with an initial water depth of $h_0 = 50mm$

The domain was generated using GMSH software, see Figure 4.15, and the domain's mesh characteristics are indicated in Table 4.17. The computational domain is discretized into an unstructured triangular mesh. The simulation is carried out for a mesh resolution of 0.1 m at the outer domain, and 0.03 m for the area closer to the structure to achieve higher accuracy of the represented viscous, turbulent flow around the structure. A more detailed description of the procedure of the discretization is presented in Appendix A, included in the Tutorial for the numerical simulation.

- **Initial volume of deposited water at the reservoir**

  Attention should be drawn to the initial reserved volume behind the gate since a higher value than the experimental one is used. In the experiments, there was a turbulent and fully aerated hydraulic jump on the upstream side of the building, which increased the upstream accumulation during the impact and reduce the flow through the sides. The hydraulic jump is not captured by the numerical model and using the same volume of $7m^3$ as the experiment the loading duration was not sufficient to keep the quasi-steady part of the flow long enough, and the results diverged from the experimental ones. Consequently, a larger volume is needed to maintain the same loading duration between the experiment and the model. The optimum accuracy to simulate similar flow conditions to those tested in the physical experiment was accomplished by an initial volume of $V = 10.30m^3$ at the reservoir.

4.3.2. Validation of dam break with a building and different orientations

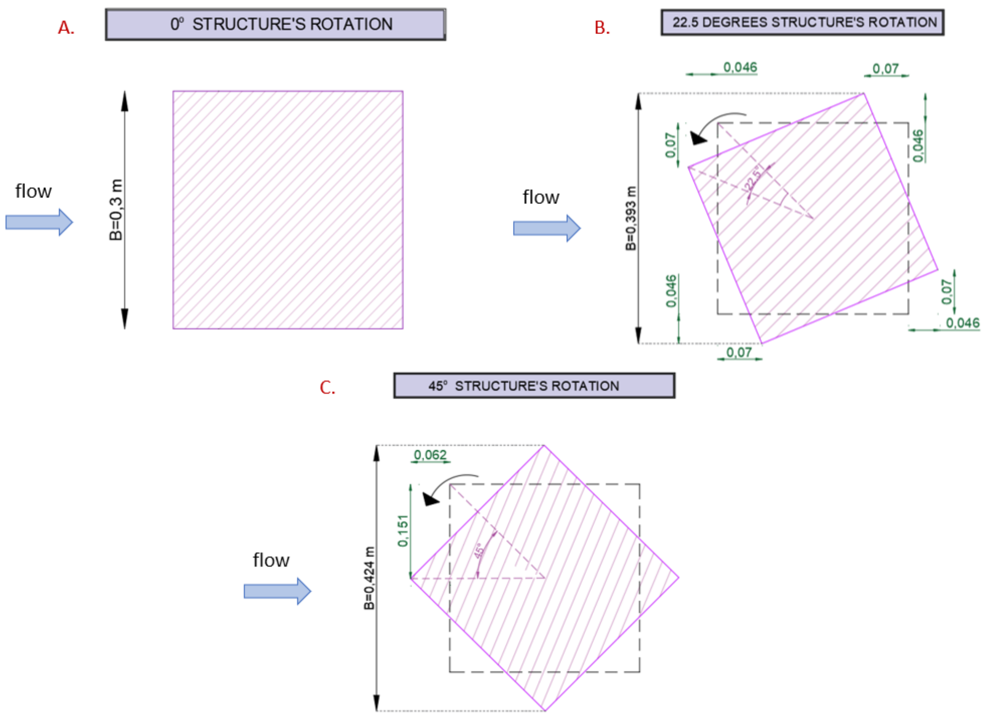

Figure 4.16: The different geometric configurations of the impervious, cubical structure which are considered for the validation of the numerical model: A. vertical front wall to the flow (θ=0°), B. θ=22.5° C. θ=45°.

A set of three different trials was used for the validation of the numerical simulation regarding the experiments [86–88, 91, 93]. Three impact orientations were tested, $\theta = 0°$, $\theta = 22.5°$, and $\theta = 45°$, Figure 4.16. In this Figure 4.16, the projected frontal width of the structure is depicted indicating that rotation increases the blockage ratio to a higher surface perpendicular to the flow. For each configuration, an initial volume of $V = 10.30m^3$ was stored at the dam's reservoir and released instantaneously at $t = 0s$. For the specific initial volume and an initial impoundment depth of 0.63m at the reservoir (upstream of the gate), the required length is set equal to 11.7m. Flow depths and velocities are computed by the simulation at three different points upstream from the structure, namely prob1(13.35, 0.7), prob2(13.85, 0.7), and prob4(14.15, 1.591) for an overall duration of 20 seconds. The points are identical to the US5, US7, and US4 of the experiment, respectively.

The rotation of the building by θ degrees results in larger projected widths and thus, larger blockage ratios. For the validity of the model, the water elevation in time is compared by the experimental data, for each tested configuration, at the 3 points of measurement, US5, US7, and US4.

However, the arrival time of the simulated wave showed a constant delay equal to 0.95s at the numerical results for all the considered orientations. A higher spatial and temporal resolution is needed to investigate whether this delay is caused by the coarse mesh generation. The constant delay is measured for all the cases and it does not affect the quality of the results.

In order to demonstrate the accuracy of the numerical model, the bore surface elevation in time was compared with the corresponding experimental results. To achieve a better agreement with the experimental results, the numerical time simulation of the water surface was shifted so that the wave arrival time coincided. The comparison is presented in Figure 4.17, and the results including the delay are presented in the Appendix D. Additionally, the model is programmed to derive the velocities at the specific points as well. The comparison with the experimental velocities is not feasible since data are not available from the experiment. Therefore, velocities were excluded from the validation.

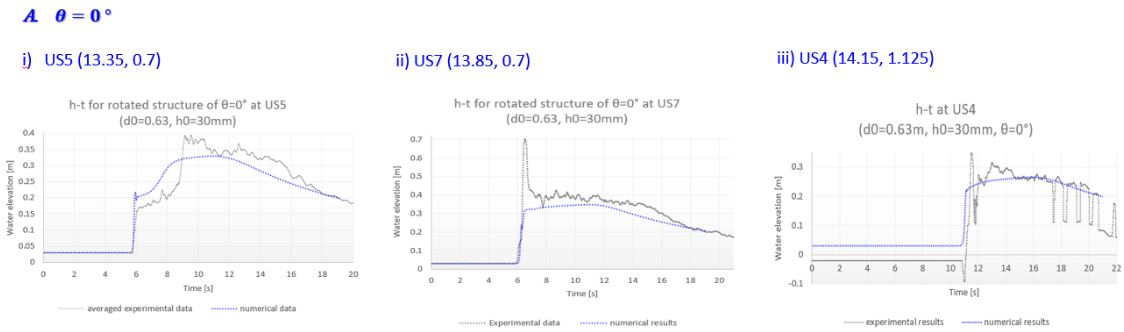

(a) time evolution of the flow depth at 13.35 m and 13.85 m for $\theta = 0°$

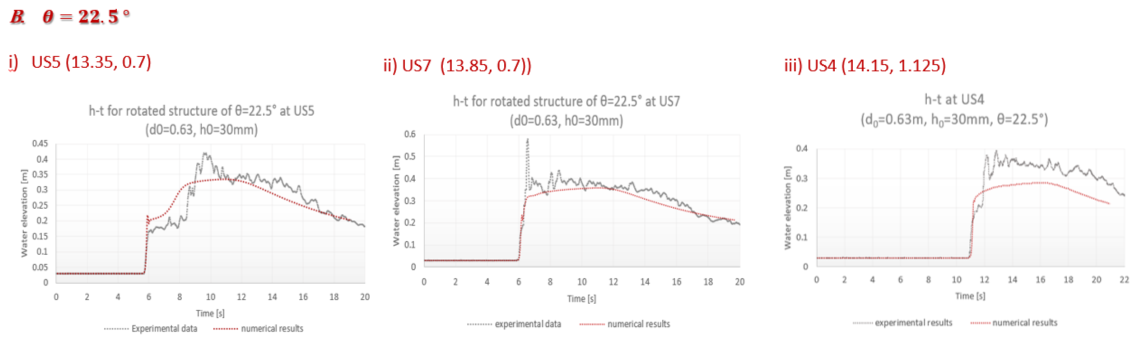

(b) time evolution of the flow depth at 13.35 m and 13.85 m for $\theta = 22.5°$

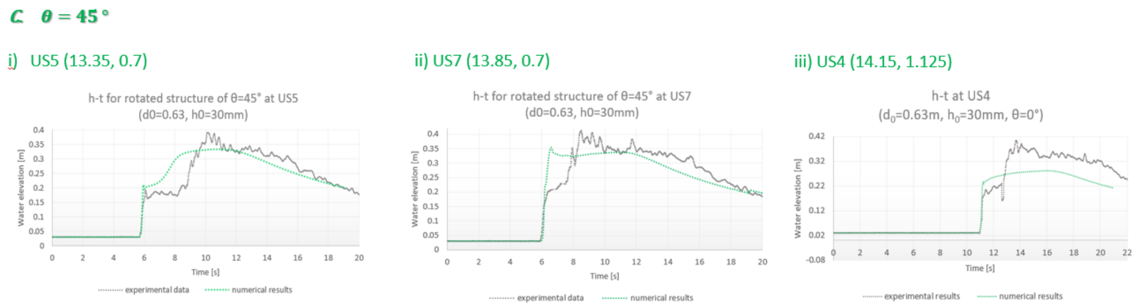

(c) time evolution of the flow depth at 13.35 m and 13.85 m for $\theta = 45°$

Figure 4.17: Comparison of numerical results, with the experimental data, for the case of $d_0 = 0.63m$ and $h_0 = 30mm$. An impervious, square building is located at a distance of 14m from the dam location and 3 different orientations are considered: 0°, 22.5°, 45°. The points of measurement for each orientation are at US5 (13.35, 0.7), US7 (13.85,0.7), both on the upstream side of the building, and US4 (14.15, 1.125), on the lateral side.

4.3.3. Remarks of the second validation test with a structure

In agreement with experimental data, the numerical simulations were able to replicate the experiments conducted, capturing, quite accurately, the main features of the flow and the interactions with the building for its configuration. In this section, the focus is mainly on the discrepancies in the compared measurements both qualitatively and quantitatively.

As already mentioned, the curves are shifted for 0.95s so that the numerical results are in line with the arrival time of the bore at the experiment. For each of the three measuring points: US5 (13.35,0.7), US7 (13.85, 0.7), and US4 (14.15, 1.125), the numerical results are derived and compared with the experimental ones, Figure 4.17. The following concluded remarks are drawn from the comparison between simulated and experimental results:

- **US5**
  During the impact phase, around t=6s, the water elevation at US5 is slightly overestimated at the initial phase when the bore reached the building. The experiment results were reproduced by vertical release from a high to a lower reservoir and the reproduction of the shock wave is not as abrupt as the numerical model, which simulates an instantaneous dam failure at t=0s. In the sustained hydrodynamic phase (plateau zone), the results are in good agreement with the experimental ones with slightly lower values.
- **US7**
  The impact of the run-up is not captured by the numerical model. Therefore an underestimation at the initial phase of the arrival of the bore was expected in the results. The run-up decreases with the angle of rotation, and the deviations are more distinct for the case where the wall of the building is vertical to the flow ($\theta = 0°$). When the angle of the edges of the building is facing the flow, then separation of the flow occurs, and the velocities are higher, leading to a drop in the water elevations and the run-up against the structure. After the impulsive phase, the hydrodynamic phase is captured more accurately with slightly lower water levels than the experimental ones.
- **US4**
  At this point, the turbulence is high, and some of the inconsistencies have to do with the experimental measurement uncertainties. The sudden drops in the experimental results were caused by water interruptions on the sensor, justifying the missing data at these moments. Apart from these external factors, the overall behavior of the water elevation was captured, and compared to the numerical results. The following remarks can be driven:
  - The agreement is accurate for the case with $\theta = 0°$.
  - When the building's rotation is considered, simulation underestimates the water depths with the following differences:
    - ◇ 24% decreased water elevation for the numerical results, for the orientation of $\theta = 22.5°$
    - ◇ 29% decreased water elevation for the numerical results, for the orientation of $\theta = 45°$

5

Results

The numerical model will be extended, using the experimental setup by Wüthrich et al. (2020) [91]. The scope of this chapter is to estimate the impact of the dam-break wave on the structure. The focus of the research targets the orientation of the impervious building around its axis, its shape, and the blockage ratio. The blockage ratio is the projected width of the structure to the flow divided by the width of the channel. Several suites of geometric configurations of the impervious structure are examined. Figure 5.1 depicts the 8 different study cases, and in Table 5.1, the analytical description is given.

Impervious buildings	**Description**	**Blockage ratio**
Square, θ=0°	The upstream edge is perpendicular to the direction of the flow.	$\frac{0.3}{1.4} = 0.214$
Square, θ=15°	The upstream edge is rotated to the direction of the flow, and the blockage ratio increases.	$\frac{0.367}{1.4} = 0.262$
Square, θ=22.5°	The upstream edge is further rotated to the flow direction and the blockage ratio increases.	$\frac{0.393}{1.4} = 0.281$
Square, θ=45°	The angle of the edges is facing the direction of the flow, and the building is symmetrically placed with respect to the wave propagation. The blockage ratio is maximum for this angle of rotation.	$\frac{0.424}{1.4} = 0.303$
The second case for θ=45°	To study more thoroughly the effect of the blockage ratio, the 45° case is tested again, using the blockage ratio of the impervious square building with $\theta = 0°$, equal to 0.214. To achieve the mentioned ratio, the width of the domain increased from 1.4m to 1.98m. The coordinates in the y direction for the building and the probs were changed accordingly, Figure 5.2.	$\frac{0.424}{1.98} = 0.214$
Square, θ=60°	The frontal edge is rotated further, to 60°. Due to symmetry around the z-axis, the blockage ratio decreases from now on.	$\frac{0.41}{1.4} = 0.293$
Square, θ=70°	The blockage ratio decreases.	$\frac{0.385}{1.4} = 0.275$
Rectangular shape	The frontal edge is vertical to the flow direction, and the blockage ratio is almost doubled from the other cases.	$\frac{0.6}{1.4} = 0.428$

Table 5.1: Description of the different tested cases.

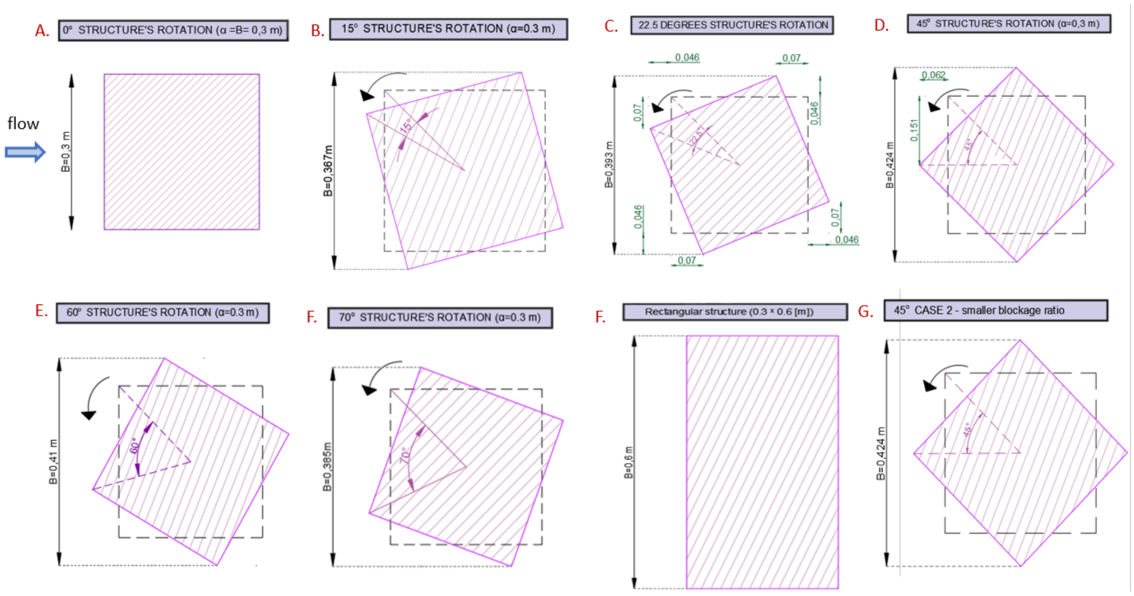

Figure 5.1: The different geometric configurations of the impervious structure.

Moreover, four different points around the considered structure are used to analyze the results. Since the main interest is focused on the area near the structure, the examined probs are located at a close distance around the structure, two points upstream (Prob1 and Prob2), one downstream (Prob3), and one at the upper side next to the building, between the wall of the channel and the side wall of the buildings, Figure 5.2. The time history of water elevation and velocities in the 4 different points were conducted by the simulation for a duration of 20 seconds and the results are compared. Lastly, the impact on the structure was computed for each case respectively, to see how the geometry and the rotation affect the loads acting on the building's boundaries, and to investigate which parameters have the highest contribution to the load impact on the buildings.

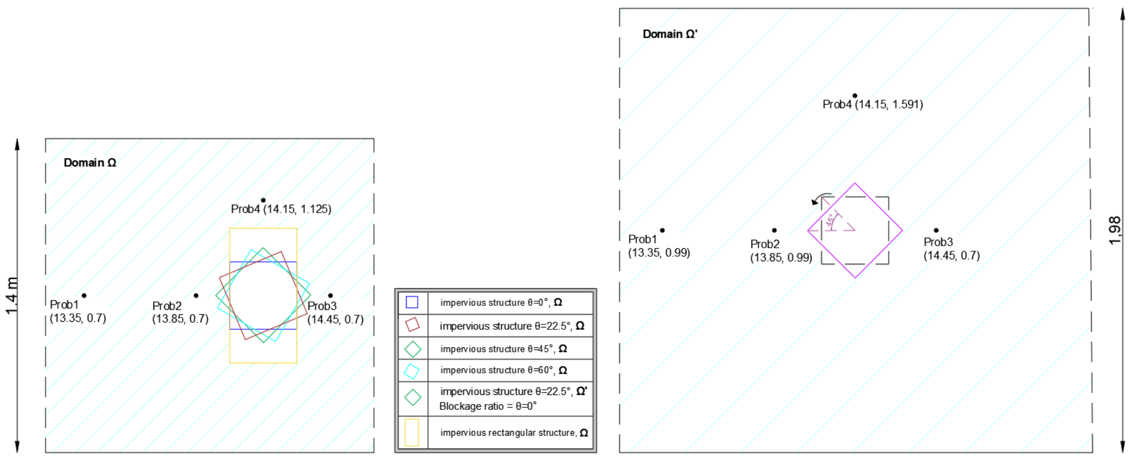

Figure 5.2: The four different measuring points that are considered for the research around the impervious structure. **(LHS)**: The domain has the same characteristics as the experiment. **(RHS)**: The width of the domain increases from 1.4m to 1.98m to keep the blockage ratio equal to 0.214. The coordinates of the probs changed for this case.

5.1. Numerical results at the fixed points

A free-standing, impervious building generates a backwater effect, resulting in a much higher water depth at the front than in the case that flow propagates in an empty channel. The flow is blocked due to the presence of the building and a buildup of water starts upstream, after the arrival of the bore. A schematization of this phenomenon is depicted in Appendix F, where a water evolution in time is simulated around the tested cases, for the different building configurations. At the measuring point Prob2(13.85, 0.7), an increase of 47% was estimated for the case of an impervious cubical structure, placed perpendicular to the flow ($\theta = 0°$), compared to the time history of the water depth, at the absence of the building, Figure 5.3.

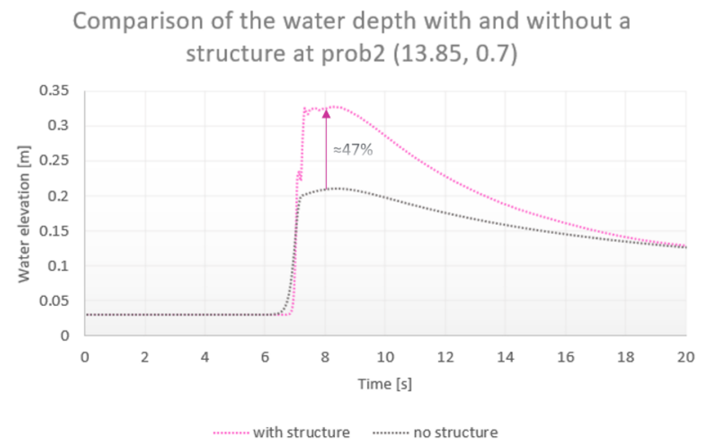

Figure 5.3: Increase of water depth in Prob2 measuring point for considering an impervious, cubical building.

In this section, the water elevations and the averaged velocities at the considered points are presented, and the results are compared for all the examined cases, Table 5.1, to evaluate the behavior of both water levels and velocities around the structure.

5.1.1. Results at prob2

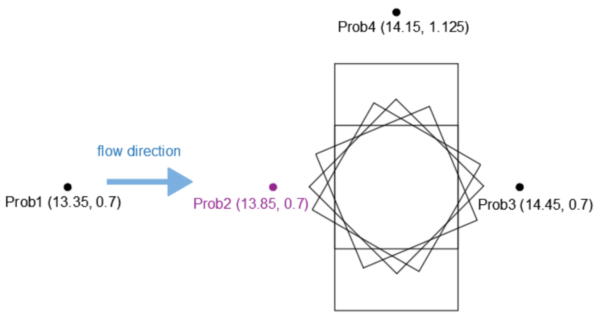

Figure 5.4: Measuring point Prob1(13.85, 0.7).

All the different cases, square, impervious structure (0.3 × 0.3 [m]) with orientations of θ= 0, 22.5°, 45° - two cases, considering different blockage ratio per time -, 60°, 70°, and rectangular with double length dimension (vertical to the flow) than width (0.6 × 0.3 [m]), were studied. The results are derived from the numerical simulation, for a duration of 20 sec, a time step of 0.05s, and a mesh discretization of 0.1m far away from the structure, and 0.03m around the structure. The time histories for both water elevation and velocities are derived at the fixed points and plotted together for all the study cases.

The first point, prob1, is located on the upstream side of the structure. It follows a similar behavior with the second upstream point, Prob2, which is placed closer to the structure, Figure 5.4. In the upcoming Figure 5.5, the behavior of both water elevations and velocities for Prob2, is zoomed into the period of [7.2s, 9.5s] to present the behavior of the results at the time that the bore arrives at the structure and beyond.

From Figure 5.5i, and ii, it is clear that the impermeable, rectangular building (light blue lines) has much more distinguished results compared to the square, impervious configurations. For this case, it can be concluded that the shape of the structure, and more specifically the blockage ratio, overrules the behavior of the results, as for this configuration, the lowest velocities and the highest water levels are observed, compared to all the tested cases. The long side of the rectangular building, which is almost doubled for the rest of the examined cases, is placed perpendicularly to the flow direction and acts as a block for the flow, causing a reduction in the velocity field which is 58% compared to the square shape. Additionally, the largest blockage of the flow results in higher water levels upstream, due to higher run-up on the building surface, and also higher

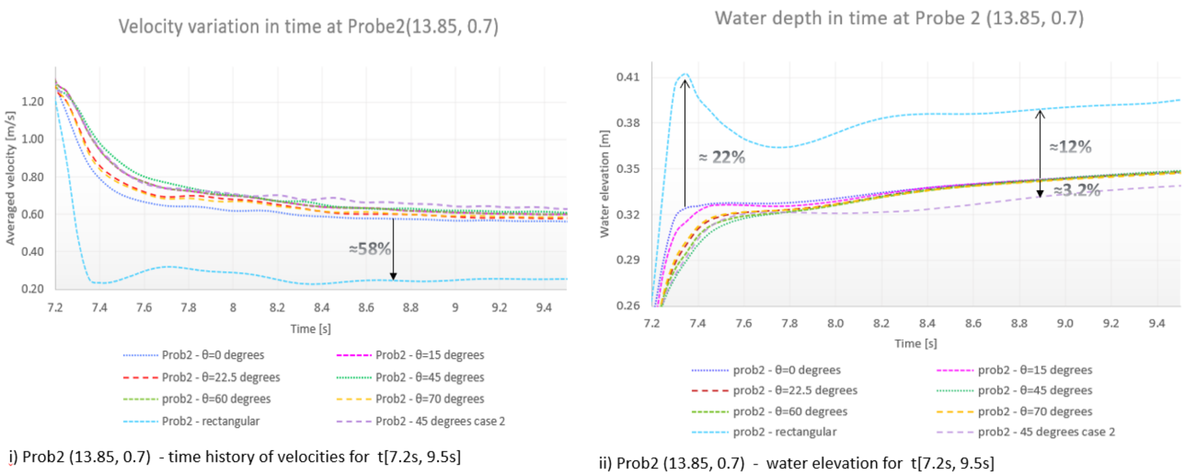

Figure 5.5: The time histories of velocity and water elevation behavior, respectively.

reflected waves. During the impulse phase, an approximately 22% rise in the water elevation compared to the frontal square building is estimated, and at the hydrodynamic phase, the increase is around 12%.

The focus should be given also to the square impervious configurations to investigate how orientation affects the behavior of the water elevation and velocity field in time at the upstream side of the buildings. From Figure 5.5i, an increase in the velocities is noticed as the angle of rotation increases until 45°. At 45° the maximum velocities are recorded and the highest values are for the second case with the smallest blockage ratio. Increasing the angle beyond 45° the velocities start reducing again, due to the symmetry (blockage ratio reduction). For the water elevation, Figure 5.5ii, the opposite behavior occurs. The increase of the angle from 0° to 45° favors the flow around the structure. The upstream sidewall of the building is not perpendicular to the flow anymore, and the corner of the edges of the walls starts facing the flow. Thus, a smoother pattern flow is observed around the buildings. The results for the rotated configurations were derived with higher velocities and lower maximum water elevations upstream of the structure. The differences in water elevations are easier to be distinguished at the impulsive phase, around 7.2s to 7.6s, where the wave arrives at the structure's upstream facade. This contributes to the reduction of the run-up on the building's surfaces, with the case of 45° rotation providing the safest shelter since the flow, which is separated symmetrically around the sides of the building, is enhanced the most, and a smoother flow is accomplished, with the lowest water elevations. A mirror effect is happening from 45° to 90° due to symmetry around the z-axis, meaning that velocities start to decrease again, and water levels increase until the building returns to the initial position, vertical to the flow, for $\theta = 90°$, this time. The symmetrical behavior has already been proved by [74]. The highest velocities and the lowest water elevations are noticed for the 45° orientation and the smallest blockage ratio. The blockage ratio is the only changed parameter and it is obvious from the results that it affects the flow around the building. By its definitions, it increases with the rotation until 45°, and this parameter acts as an obstacle to the flow, reducing the beneficial effect of the structure's orientation. Therefore, a reduction of 3.2% at the water elevation is achieved by keeping the angle of 45° for the square, impervious configuration, and equalizing the blockage ratio to the case of 0° orientation, Figure 5.2(ii) purple line. Keeping the blockage ratio the same, the only parameter that changes compared to the frontal square case is the angle of rotation, and in this way, it is even more pronounced that the rotation of the impervious building decreases the water elevation and increases the velocities at the upstream side of the building.

5.1.2. Results at prob3

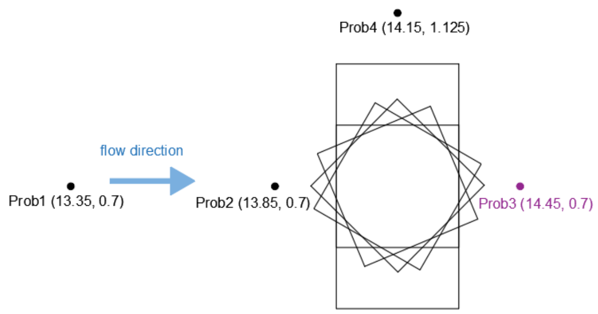

Figure 5.6: Measuring point Prob1(14.45, 0.7).

The prob3 examined point is located downstream of the building's boundary walls, at the shadow zone of the impervious structure, Figure 5.6. The point is inside the wake zone. In the case of sharp, impervious edges, as the examined shapes of the considered buildings, combined with unsteady flows (high Reynolds numbers), flow separation occurs together with a wake zone behind the structure. Flow retardation and separation increase the turbulence, and hence, the loads caused by the flow [72]. Jet flows are created downstream of the structure and combined with the accelerated flows at the sides a circulation current is schematized, leading to erosion and causing a wake vortex in a wide zone downstream of the structure. This phenomenon can cause great damage to the stability of the building and vortexes can also produce unwanted vibrations. To visualize the effect of the separation, Figure 5.8 presents the velocity field for all the tested cases at t=10.35s, using the Render View in ParaView. Different streamline patterns are noticed leading to also different schematizations of the separation zones. The separation zone is reduced significantly for the case of the 45° orientation where the symmetrical separation of the flow leads to a shorter shadow zone, hence the impact of the turbulence due to the induced vortices will be less for this orientation compared to the rest.

The results for the time history of velocities and water elevations are depicted in Figure 5.7. The irregularity and the fluctuations of the velocity curves are caused by the high turbulence due to the vortices and they do not lead to a specific pattern. But comparing both velocities and water depths with the upstream data derived at prob2, the following can be observed:

- For the velocities, a 50% reduction is noticeable which increases further with the course of time. For the rectangular shape, the flow can be characterized as stagnant at Prob3, after the time t=14s, since velocities are recorded very close to zero.

- The water elevation is also reduced significantly with respect to the upstream levels, and this increases the hydrostatic loads. Especially for the rectangular case, the drop is more than 50%. The double frontal surface results in the highest accumulation on the upstream side leading to higher reflected waves in the upstream direction. Thus, the wave is highly dissipated on the downstream side. The highest hydrostatic forces are expected as well.

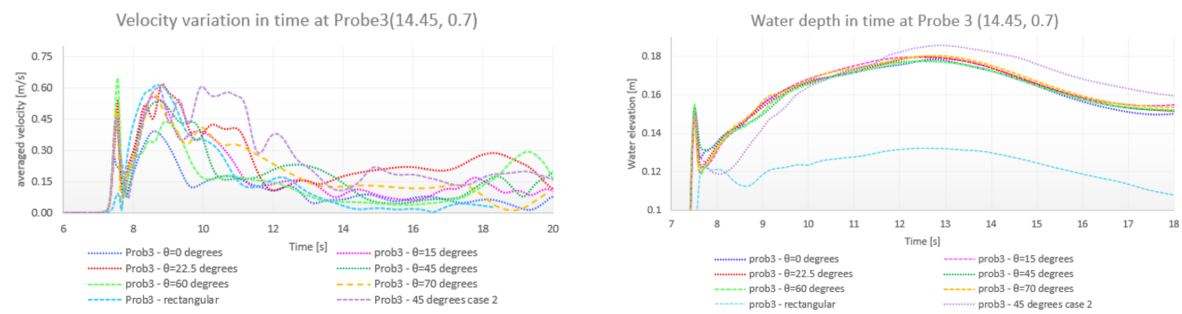

i) Prob3 (13.85, 0.7) - time history of velocities for t[7.2s, 9.5s]

ii) Prob3 (14.45, 0.7) - water elevation for t[7.0s, 18.0s]

Figure 5.7: The time histories of velocity and water elevation behavior at the measuring point behind the structure, Prob3.

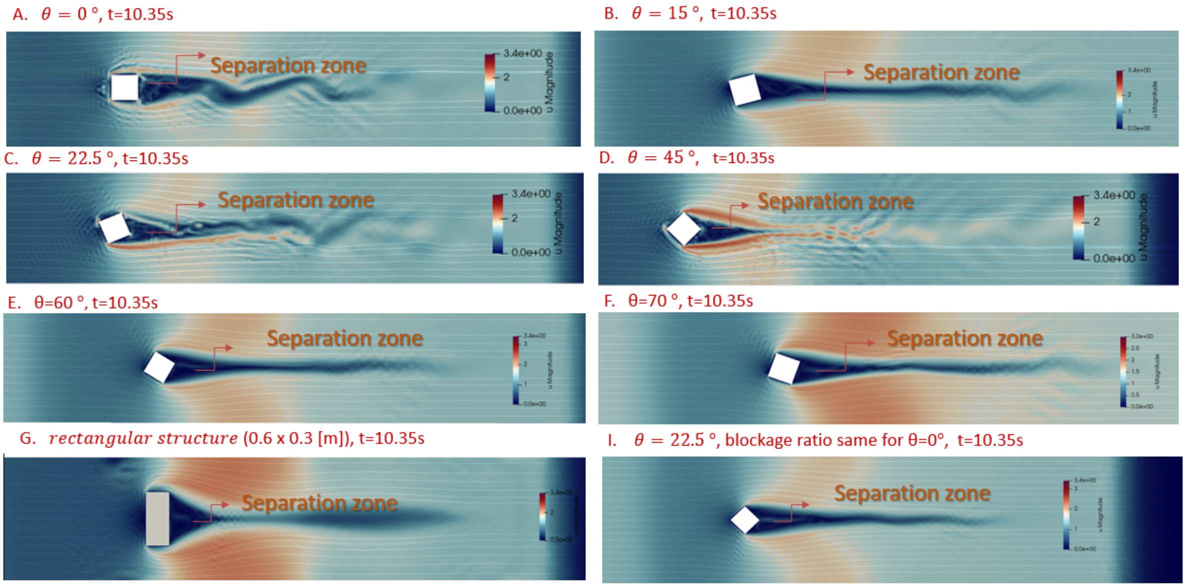

Figure 5.8: Separation zone at t=10.35s for all the considered geometric configurations.

5.1.3. Results at prob4

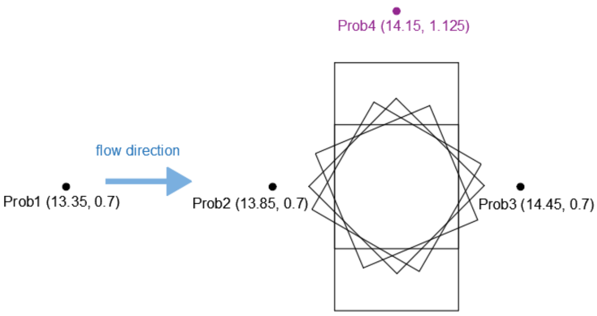

Figure 5.9: Measuring point Prob4(14.15, 1.125).

The prob4 is placed halfway between the upper lateral side of the frontal building, and the sidewall of the channel, Figure 5.9. At this part of the domain, the cross-sectional area of the width of the channel is reduced by the existence of the impervious building. Due to the conservation of the momentum, the flow rate increases for smaller cross sections, leading to a higher concentrated field of the streamlines (focusing of the flow), therefore to higher velocities. Consequently, water elevations should drop at this part of the domain. However, the increase in the blockage ratio leads also to higher water levels upstream, and hence, higher reflected waves.

From Figure 5.10, results are not only affected by the blockage area at the lateral sides of the building. The angle of rotation changes the geometrical shape that confronts the flow. More specifically, the flow against the rotated sides of the building changes the streamlined pattern because separation occurs earlier. The separated flow due to the wall turbulence causes mixing layers that influence the extracted data at the point of interest for some configurations. Any velocity difference causes the growth of a mixing layer, accelerating the fluid particles at the area with the smaller velocities, whereas the flowing mass is losing momentum [72]. At these layers, the turbulence is higher.

For orientations from 0° to 45°, since prob3 is located at the upper side of the channel together with the rotated angle, the decelerating zones of the flow affect the results. This influence causes a reduction in velocities. For $\theta > 45°$, the flow patterns cause an increase in the velocities, at the side. Moreover, for the case of 0° rotation, the streamlines remain parallel to the flow at this point, thus the turbulence flow due to the presence of the structure does not affect the flow there, since the separation starts downstream of the structure. Additionally, the blockage ratio is the lowest in this case, and smaller reflected waves are expected. Hence, the resulting velocities are high at the lateral sides for 0 ° orientation, coming after the rectangular and the 70°.

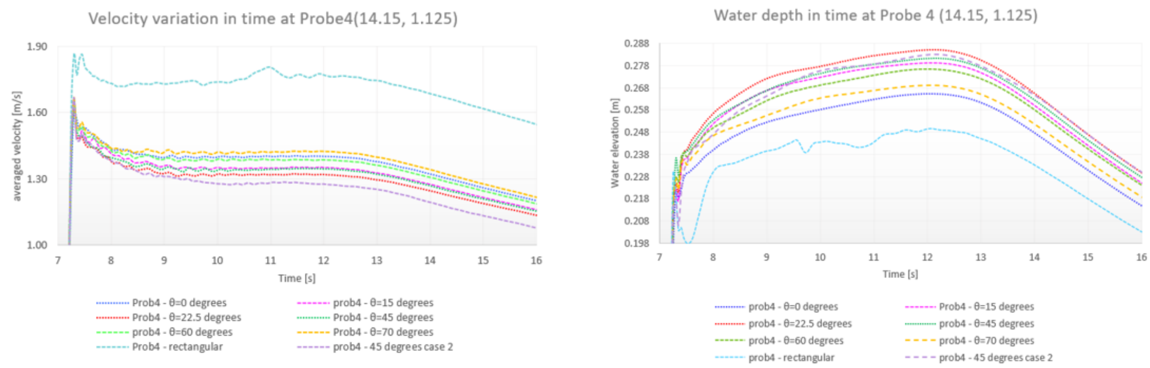

i) Prob4 (14.15, 1.125) - time history of velocities for t[7.0s, 16.0s]   ii) Prob4 (14.15, 1.125) - water elevation t[7.0s, 16.0s]

Figure 5.10: The time histories of velocity and water elevation behavior at the measuring point next to the structure, Prob4.

5.2. Horizontal forces on building

Coastal flooding, generated by highly unsteady flows, exerts significant forces that they are acting on the exposed buildings. The impact of the wet bed bores on the impervious building is quantitatively tested by calculating the forces acting on the structure. The force vector consists of two components which come from the hydrostatic and the hydrodynamic stresses exerted on each vertical wall of the structure's boundary. The generated bore for the initial conditions of $d_0 = 0.63m$ impoundment water depth behind the dam, and $h_0 = 30mm$ initial water level at the channel downstream of the dam is now used to generate the impact on the impervious free-standing building. Firstly, the forces of the three orientations, $\theta = 0°$, 22.5°, 45°, derived by the experimental measurements, are used for the comparison with the numerical horizontal forces in the x and y directions.

The most accurate way to obtain the hydrodynamic loads is via the distribution of the stresses. Integrating the stresses over the surface can provide an accurate solution for the total forces. The Cauchy stress tensor, denoted by σ, is a symmetric, 2-order Cartesian tensor. It describes the stress behavior at a point, and the diagonal elements correspond to normal stresses, while the non-diagonal ones to shear/deviatoric stresses. The force vector in the horizontal direction contains two components (longitudinal, x, and lateral, y direction), and it can be derived by integrating over the wet surface of the impervious structure. The boundary of the wet surface of the building is set as Γ_w in the numerical simulation. The equation for the resultant forces is:

$$F = \int_{\Gamma_w} \sigma \cdot \vec{n}\Gamma_w \cdot h \, d\Gamma_w \tag{5.1}$$

5.2.1. Stresses acting on the surface of the building

For an incompressible fluid, the stress tensor can be decomposed into the following equation [81]:

$$\sigma = \tau - pI \tag{5.2}$$

Where τ expresses the deviatoric stress component. When the fluid is static $\tau = 0$ and p express the static pressure. For an isotropic fluid τ can be expressed as:

$$\tau = 2 \cdot \mu \cdot \epsilon + \lambda(\nabla \cdot u)I \tag{5.3}$$

The parameters λ and μ are Lame's first and second parameters, respectively. The parameter μ is referred to the dynamic viscosity of the fluid, which can be derived by the product of the kinematic viscosity and the density of the fluid ($\mu = \nu \cdot \rho$). The λ parameter is related to the μ coefficient by $\lambda = -\frac{2}{3}\mu$ according to Stoke's hypothesis, which is valid for Newtonian fluids [61]. The relation between the symmetric term of the strain rate ϵ and the velocity gradient tensor ∇u is written as follows:

$$\epsilon(u) = \frac{1}{2}\left(\nabla(u) + \nabla(u)'\right) \tag{5.4}$$

The second term of the equation 5.2 is the diagonal matrix expressing the isotropic part of the stress tensor. I is the identity matrix, and p is a scalar, determined as the sum of the diagonal elements of the matrix σ. The hydrostatic pressure, p, is the average of normal stresses (diagonal terms of the two-dimensional stress tensor):

$$p = -\frac{tr(\sigma)}{2} = -(\sigma_{11} + \sigma_{22})/2 \tag{5.5}$$

Where $tr(\sigma)$ is the summation of the diagonal elements of the stress matrix. For a moving fluid, p denotes the dynamic pressure [81].

According to the above, the stress formulation, used for the numerical simulation, is the following:

$$\sigma(u,h) = \mu\left(\nabla(u) + \nabla(u)'\right) - \frac{2\mu}{3}(\nabla \cdot u)I - \rho \cdot g \cdot (h+H)I \tag{5.6}$$

Where the first two terms on the right-hand side (RHS) are dynamic components due to the movement of the fluid. These terms mainly control the degree of body distortion. The last term is related to the hydrostatic stress component. More analytically the terms on the RHS:

1. shear or deviatoric component → The stresses are acting parallel to the surface and depend on the spatial distribution of the velocity near the boundary. Generally, the deviatoric stresses become important when the shear is large, usually near boundaries. The entire deformation tensor is included with the asymmetric part due to the vorticity. The shear stress in fluids is greatly affected by the fluid's resistance/viscosity.
2. volumetric component → denotes the volumetric stresses, as it is proportional to the divergence of the velocity field. Attention should be given for incompressible fluids, for which the divergence of the velocity is zero, div u = $\nabla \cdot u = 0$. Hence, the second term of the volumetric stresses should be negligible for this specific study, (see Figure 5.11ii).
3. hydrostatic component → The hydrostatic force contains the normal stresses on the surface of the walls and represents the volumetric changes of the fluid. It has a negative sign indicating compressing forces. This is the state of stress that exists at any point in liquids at rest, it varies with depth, and exerts hydrostatic forces, in case of water level differences.

As it is stated before the forces will be derived by integrating the stresses over the wet area of the building's walls, equation 5.1. Subsequently, forces will contain 3 terms, the hydrostatic force, and the hydrodynamic force which consists of the shear and the volumetric components.

5.2.2. Wake zone as a force contributor

Another parameter that enhances the hydrodynamic forces acting on the impervious building is the wake zone behind the structure. Specifically, the wake formation increases the turbulence due to the vortices behind solid bodies and this leads to a significant increase in the drag force on the building. More specifically, when the fluid detaches from the body, a separation zone is induced, creating a wake of recirculating flow. To comprehend more the creation of the separation zone behind the structure, the connection with the flow rate should be explained. When flow accelerates pressure is decreasing in the direction of the flow, and this is called a favorable pressure gradient $\frac{dp}{dt} < 0$. Beyond a certain point, the flow starts to decelerate and the pressure is increasing, causing the adverse pressure gradient $\frac{dp}{dt} > 0$. If this pressure rise is large enough, the flow will tend to reverse direction but it is not possible due to the oncoming fluid, hence it detaches from the surface, resulting in the flow separation.

The separation zone is an area of low pressure behind the object structure, Figure 5.8, and results in a large drag force. The total drag of a body appears as a loss of momentum and increase of energy in this wake. The loss of momentum appears as a reduction of average flow speed, while the increase of energy is seen as violent eddying (or vorticity) in the wake [38]. In addition, vortex shedding, for high Reynolds numbers (turbulent flow) generates unwanted instabilities in the structure. In order to reduce the drag forces, the separation zone behind the structure needs to be minimized.

5.2.3. Force components

As explained above, the different force components are caused by different phenomena, and ascertaining their level of contribution to the total forces is an important step before reaching conclusions about the overall loads. In this paragraph, the different components of the force coming from deviatoric, volumetric, and hydrostatic stresses respectively, are plotted for the three orientations of the building $\theta = 0°, 22.5°, 45°$ to check the contribution to the total force in the x direction. Attention should be devoted to the range of the different scales of the plots. The volumetric term is negligible, and the shear component is also low compared to the hydrostatic load distribution, due to the low viscosity of the water.

Shear force term: The shear component of the total horizontal force in the x direction, is plotted in Figure 5.11(i). Coming from the deviatoric stresses, it increases when the flow is parallel to the surface. So, the highest values appeared for the case of $\theta = 0°$, where the two lateral sides of the structure are both parallel to the flow, enhancing the deviatoric stresses. For the rotated cases, the flow is not completely parallel to the sides and only the component parallel to the rotating walls (2 of the 4 sides of the structure, the ones that interact with the flow) contributes to the shear force. An additional observation, based on the plotted values, is the low values of the shear forces. This is explained by the high importance factor of the viscosity term. The kinematic viscosity of water is 10^{-6}, leading to a dynamic viscosity of 10^{-3}. Hence, this term contributes slightly to the total force, but it is responsible for the turbulence phenomena and the generation of the vortices downstream of the building. Last but not least, the irregular pulsations and oscillations in the shear forces in time may be justified by the initial impact and the upward-moving wave which are highly turbulent and strongly aerated, as was proved by the physical experiment and the snapshots.

Volumetric force term: Terms are almost zero since the fluid is assumed to be incompressible, and the term is proportional to the divergence of the velocity field which is zero for incompressible fluids, Figure 5.11(ii).

Hydrostatic force term: The hydrostatic component has the highest contribution to the total force, Figure 5.11(iii). It is noticeable that the impulsive load at the arrival time of the wave to the upstream side of the building reduces with the increase in the angle of rotation. While at the hydrodynamic phase, the opposite occurs: the horizontal forces increase with an increase in the angle θ.

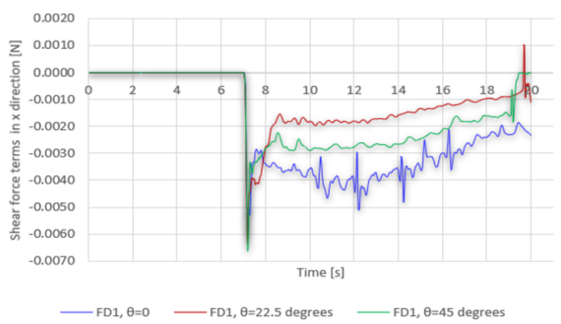

i) Shear term in x direction for θ = 0 °, 22.5 °, 45°

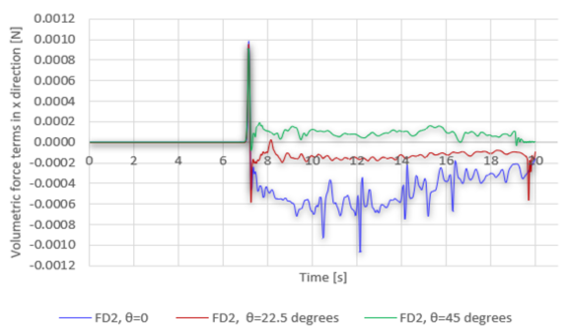

ii) Volumetric term in x direction for θ = 0 °, 22.5 °, 45°

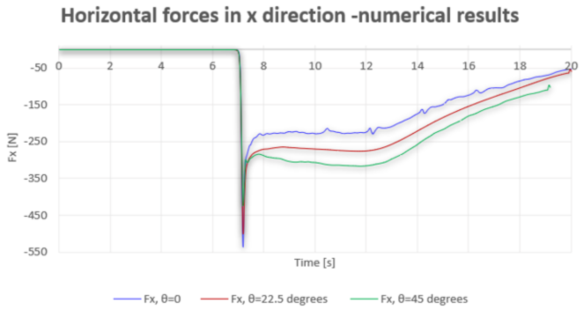

iii) Hydrostatic term in x direction for θ = 0 °, 22.5 °, 45°

Figure 5.11: Comparison of the three different force components: i)shear force, ii)volumetric forces, iii) hydrostatic forces of numerical results, for the three orientations.

5.3. Comparison of the numerical horizontal forces with the experimental results

For the three different orientations used for the validation, $\theta = 0°$, 22.5°, and 45°, experimental data of the total horizontal forces acting on the building for each case are available. In the laboratory, the buildings were installed on a force plate that recorded the time history of the impact forces and moments [87]. The raw data recorded for forces in x and y direction, for the wet bed case of impoundment water depth of $d_0 = 0.63m$ in the reservoir, and initial water depth at the channel of $h_0 = 0.03m$ are used here for the comparison of the hydrodynamic behavior with the numerical data, where the forces are produced by the integration of the total stresses in x and y direction. The results are presented in Figure 5.12.

- **Forces in x direction**
  As the rotation increases the simulated total horizontal force in x is estimated higher than the experimental. An overestimation of:
  - 5.5% for $\theta = 0°$,
  - 13.7% for $\theta = 22.5°$,
  - 31% for $\theta = 45°$.

  This overall increase is likely associated with the discrepancies in the water elevations for locations downstream of the structure. Figure 4.17 has already shown for the point US4, located at the sides of the structure, that the results are generally underestimated and the deviations increased significantly with the rotation. Unfortunately, for the points downstream of the structure, no gauges were used for the experimental research. Therefore, the results derived at Prob3 cannot be compared with the experimental ones to ensure that water elevations are underestimated, too, at this part of the domain. However, examining the setup of the physical experiment, a reasonable explanation for the lower water elevations downstream of the structure can be the different outflow conditions of the experiment. More specifically, for the wet bed conditions, an adjustable vertical sill is used for the experiment setup, placed on the downstream side, to ensure the initial water depth in the channel with a height equal to the initial water depth, Figure 4.8. In this way, the water was evacuated at the downstream end of the channel through a vertical drain, avoiding any backwater effect [87]. This vertical sill is placed close to the structure, and reflection affects the water levels downstream of the building, which causes an overall increase in them. Higher water level downstream of the structure means lower water level differences with the upstream water elevations, hence lower hydrostatic loads. On the other hand, for the numerical simulation, the domain is considered infinitely long for the duration of T=20s, to avoid the effect of reflection on the fixed points.

- **Forces in y direction**
  A similar magnitude can be seen between experimental and numerical results. The large oscillations due to the viscosity and turbulent nature of the experimental results are not captured by the model due

to the coarse temporal and spatial resolution. However, at the lower frequencies, the results fluctuate commonly.

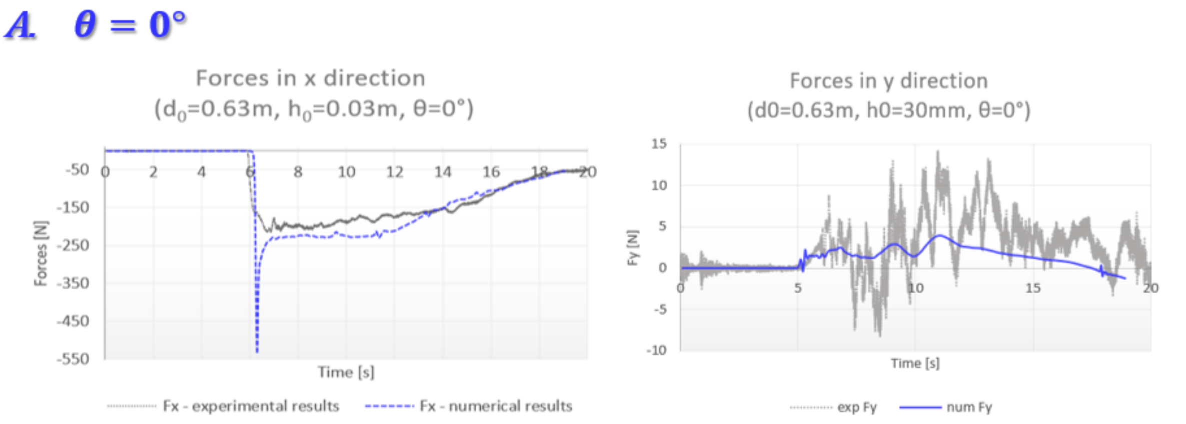

(a) Horizontal forces in x direction (LHS), and y direction (RHS)

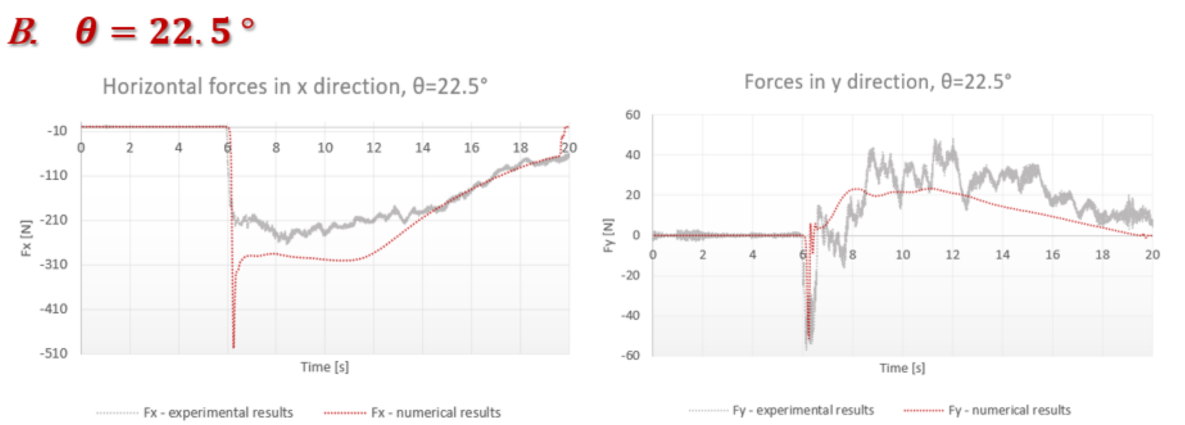

(b) Horizontal forces in x direction (LHS), and y direction (RHS)

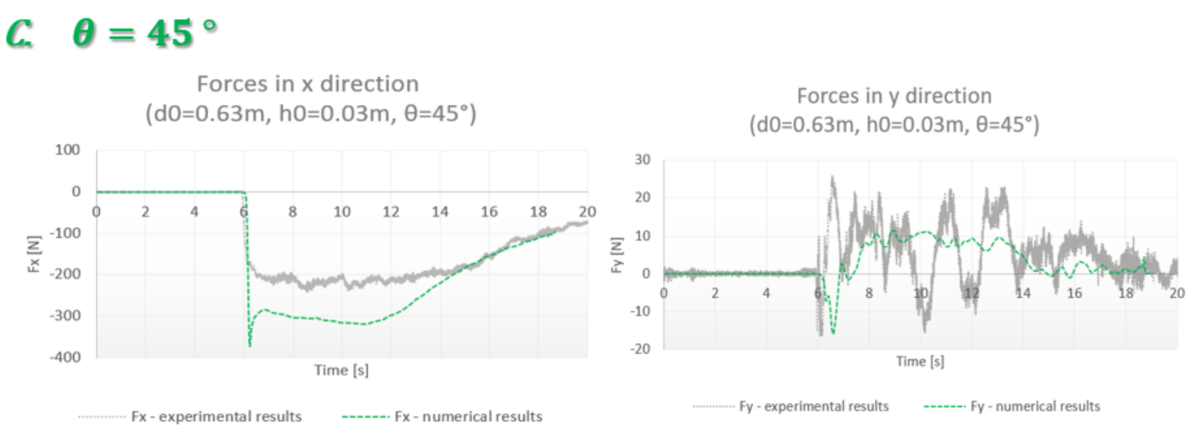

(c) Horizontal forces in x direction (LHS), and y direction (RHS)

Figure 5.12: Comparison of the time history of the total forces in the x and y direction between numerical and experimental results.

5.4. Investigation of the total force in the x direction

For the bore propagation around the impervious structure, the results showed that the orientation of the building changes the dynamics of the impact. Moreover, the forces in the x direction are at least one order of magnitude higher than the forces in the y direction. The maximum loads are relevant to the scope of this thesis, and for this reason, the force analysis will focus on the horizontal force terms only in the x direction. The total forces in x direction derived for all the eight tested cases: square impervious building with rotations around its axis, $\theta = 0°$, 15°, 22.5°, 45°, 45° - second case, 60°, 70°, and the rectangular building. The results are plotted in Figure 5.13.

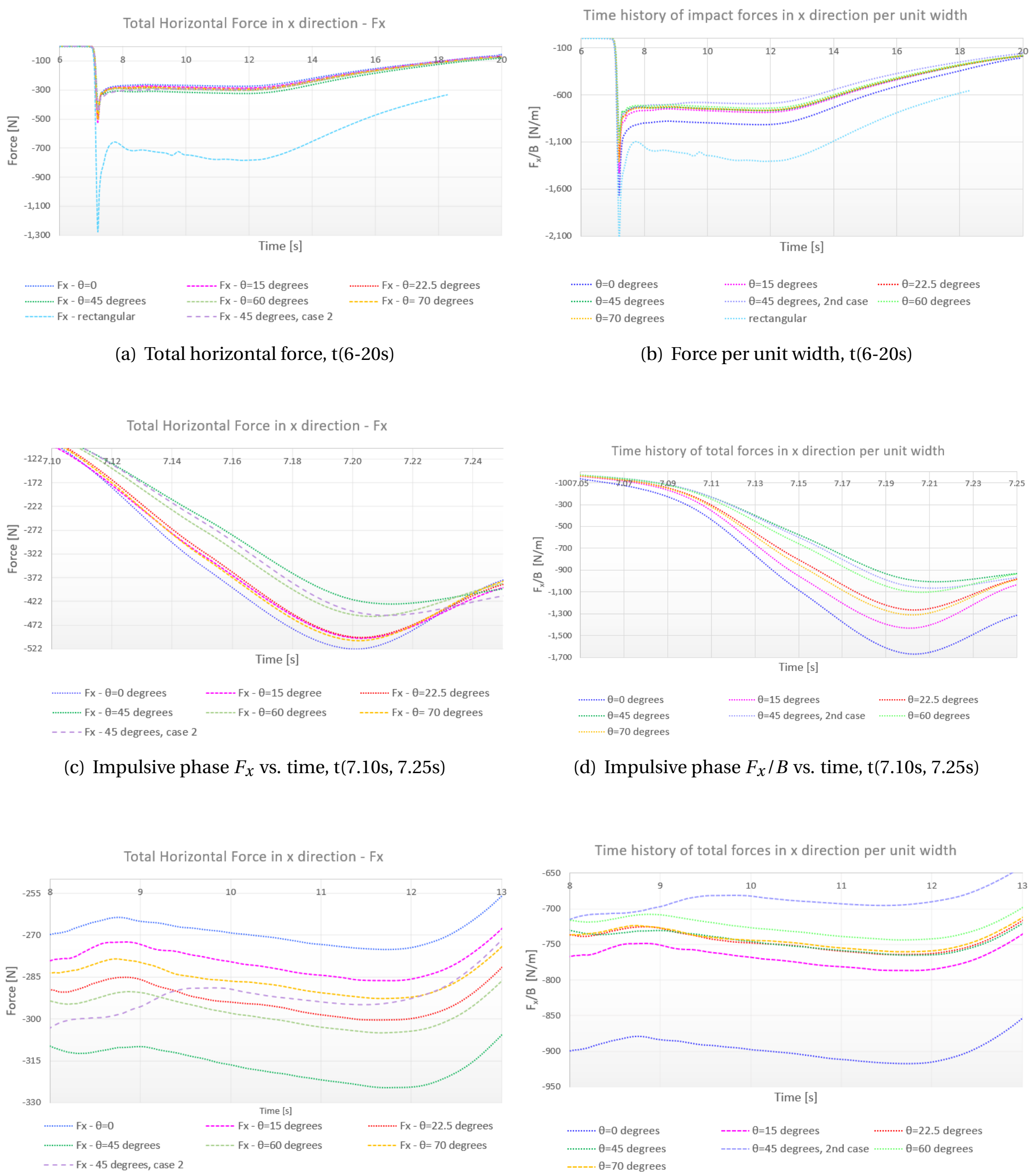

(a) Total horizontal force, t(6-20s)

(b) Force per unit width, t(6-20s)

(c) Impulsive phase F_x vs. time, t(7.10s, 7.25s)

(d) Impulsive phase F_x/B vs. time, t(7.10s, 7.25s)

(e) Hydrodynamic phase F_x vs. time, t(8s, 13s)

(f) Hydrodynamic phase F_x/B vs. time, t(8s, 13s)

Figure 5.13: **LHS**: Time history of the total forces in x direction.**RHS**: Time history of the total forces per unit width.

The sub-figure 5.13(a) leads to the conclusion that the largest horizontal forces are exerted on the rectangular shape of the impervious building. This is logical since the surface normal to the direction of the flow is almost doubled from the squared cases, increasing the hydrostatic component term. For the square building configurations, with different orientations, the results are almost identical. Since the orientation results in changes in the blockage ratios, the forces are normalized by dividing them with the projected width (the cross-section of the building frontal to the direction of the flow). Checking the force per unit width, Figure 5.13b, the load per meter is still higher for the rectangular frontal building, compared to the square frontal one. The blockage ratio is higher, which is also attributed to higher water elevations upstream and higher reflected waves, leading to lower water depths downstream, and therefore to a higher impact on the building.

For the different square, impervious buildings, the shape is the same while the rotation of the building, with respect to its axis, is changing. The differences between the time history of the total horizontal forces are not distinguishable at this time frame, not even after being normalized with the projected width. Therefore, a closer look is required at the time intervals of [7.1s, 7.25s] & [8s, 13s] to specify the observed differences regarding the orientation.

Impulsive phase of the load, t=7.10s-7.25s, Figure 5.13(c, d): The maximum absolute value of the exerted force is noticed for the case of the 0° orientation, where the walls are perpendicular to the flow and cause the highest impact on the wall. Also, the initial time of the impact load per unit width was sustained slightly longer than in the rotated cases, due to the lowest velocities and the highest reflected waves. Increasing further the orientation from 0 to 45° reduces the loads acting on the structure, for this initial phase. From 90° to 45°, results should be symmetrical, hence the forces per unit width should increase in magnitude beyond 45°, which is the observed trend from the graph. The beneficial effect of the orientation is to deviate the flow through the lateral direction when the corner of the building is facing the flow. The earlier separation of the flow leads to higher velocities and lower water elevations and run-ups, therefore lower initial bore impact. The lowest recorded one is for the case of 45°, where symmetry plays an additional role in the smoothing of the flow pattern around the building.

Hydrodynamic phase of the load - plateau, t=8s-13s, Figure 5.13(e, f): As the angle increases, the absolute value of the total force increases as well, until the angle of 45° and then, the "mirror effect", due to symmetry causes the opposite behavior. At this phase, the behavior of the total horizontal forces in the x direction follows the blockage ratio trend. As the blockage ratio increases ($0 < \theta < 45°$) or decreases ($45 < \theta < 90°$) with the orientation, the forces behave accordingly, regardless of the angle of rotation. Even more, the last observation that supports this is the case of the 45° with a smaller blockage ratio. For a blockage ratio reduction of 29.3%, a decrease of 8.5% is achieved for the total horizontal forces in the x-direction. Thus, the influence factor of the blockage ratio seems to be of high importance to the behavior of the total force.

However, the rotated configurations result in a larger projected width. Dividing the total force by the projected width of the structure to the direction of the flow for each case, additional conclusions are made:

- For the sub-figure (f) and for the two cases with the same blockage ratio of 0.214, $\theta = 0°$ and $\theta = 45°$, the maximum absolute values and the minimum in time, are recorded, respectively. The comparison emphasizes the privileging effect of the orientation of the building with respect to the flow direction. Forces divided by the column width are smaller for the diagonal orientation, and 45° presents the optimum orientation, in terms of reducing the impact on the building, due to the symmetrical separation of the flow.

- Additionally, the force per unit width is the largest for the frontal building and then decreases its magnitude with the increase of the angle, until 45°. This is an inversely proportional behavior between the total force per meter and the projected width, meaning that despite the maximum total loads in time increased with the rotation, due to higher blockage ratios, the effect of the width is such that the forces per m are smaller as the angle of rotation increases. This remark indicates that the load in the rotated buildings is distributed better to the larger available surface of the building, proving that the rotated configurations deal better with higher loads. Hence, the distribution of the stresses, and by extension forces, depends on the orientation of the structure with respect to the flow direction, providing a better shape alternative to design buildings vulnerable to unsteady flows.

5.5. Influence of the building orientation

In this subsection, a more thorough investigation is accomplished of the relation between orientation with blockage ratio, forces, and resistance coefficient.

5.5.1. Blockage ratio - angle of rotation

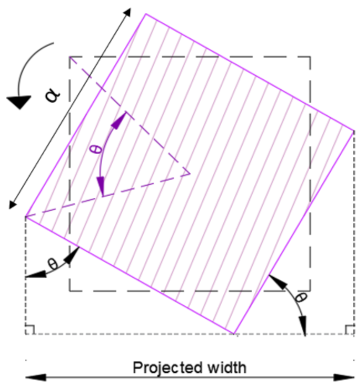

Figure 5.14: Projected width of a rotated square as a function of the angle of rotation θ.

The blockage ratio for each rotated case is plotted as a function of the angle θ. The blockage ratio plays an important role in the computation of the total force. The variable parameter of the blockage ratio is the projected width of each building configuration, and the only parameter that influences the projected width in the direction of the flow is the angle of rotation. The problem was solved geometrically, transferring the angle of rotation, as it is depicted in Figure 5.14, and the resulting relation of the projected width as a function of the angle of rotation θ is the following:

$$B_{projected}(\theta) = \alpha \cdot \left(sin\theta + cos\theta\right) \tag{5.7}$$

Where α is the side of the square, and for all the cases, it is considered equal to 0.3m. Larger projected widths to the transversal direction, result in larger blockage ratios. The blockage ratio, $\frac{B_{projected}}{B_{channel}}$, can be written as a sinusoidal function of the angle θ:

- For the channel of 1.4 m width:

$$r_1(\theta) = \frac{3}{14} \cdot \left(sin\theta + cos\theta\right) \tag{5.8}$$

- For the channel of 1.98 m width:

$$r_2(\theta) = \frac{3}{19.8} \cdot \left(sin\theta + cos\theta\right) \tag{5.9}$$

- The difference of the blockage ratio as a function of the angle of rotation is again a sinusoidal relationship:

$$dr(\theta) = \frac{29}{462} \cdot \left(sin\theta + cos\theta\right) \tag{5.10}$$

5.5.2. Normalized forces - angle of rotation

To clarify the relation between the angle of rotation on the behavior of the horizontal force, the ratios of the maximum force for each rotated configuration divided by the maximum force of the configuration with zero orientation, $\left(\frac{F_{max,\theta}}{F_{max,\theta=0}}\right)$, are plotted as a function of the angle of rotation θ, Figure 5.16. Compared to the previous research [3, 74, 86], the numerical results deviate significantly and it is noticeable an overestimation of the loads for the rotated impervious square buildings. Thus, the numerical approach gives a conservative estimation of the induced loads, compared to the previous experiments. As a result, further validation is required.

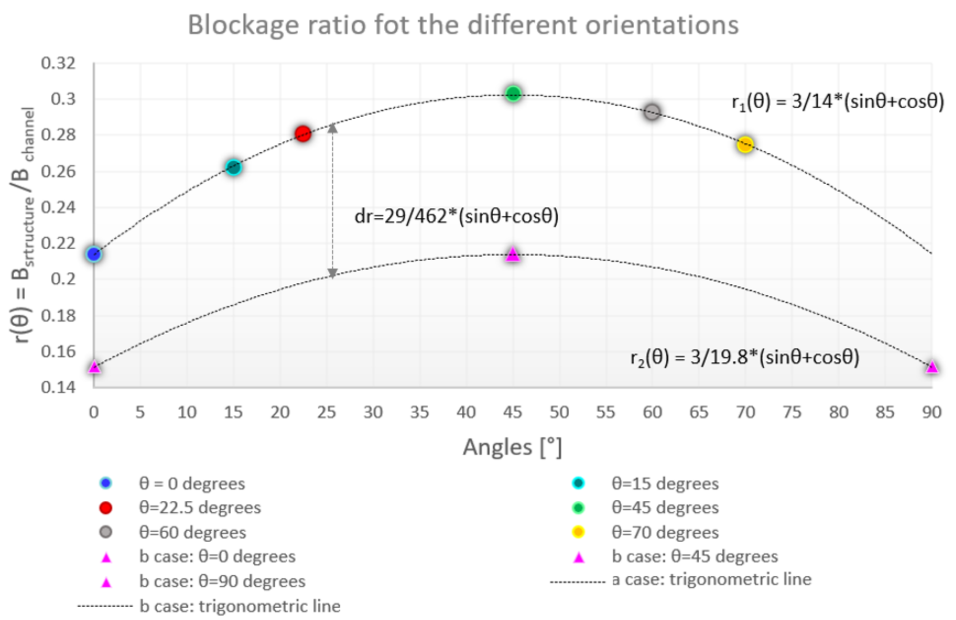

Figure 5.15: Blockage ratio as a function of the angle of rotation. The curve $r_1(\theta)$ was derived by the numerical results for a channel width of 1.4m, while the $r_2(\theta)$ curve for a channel width of 1.98m.

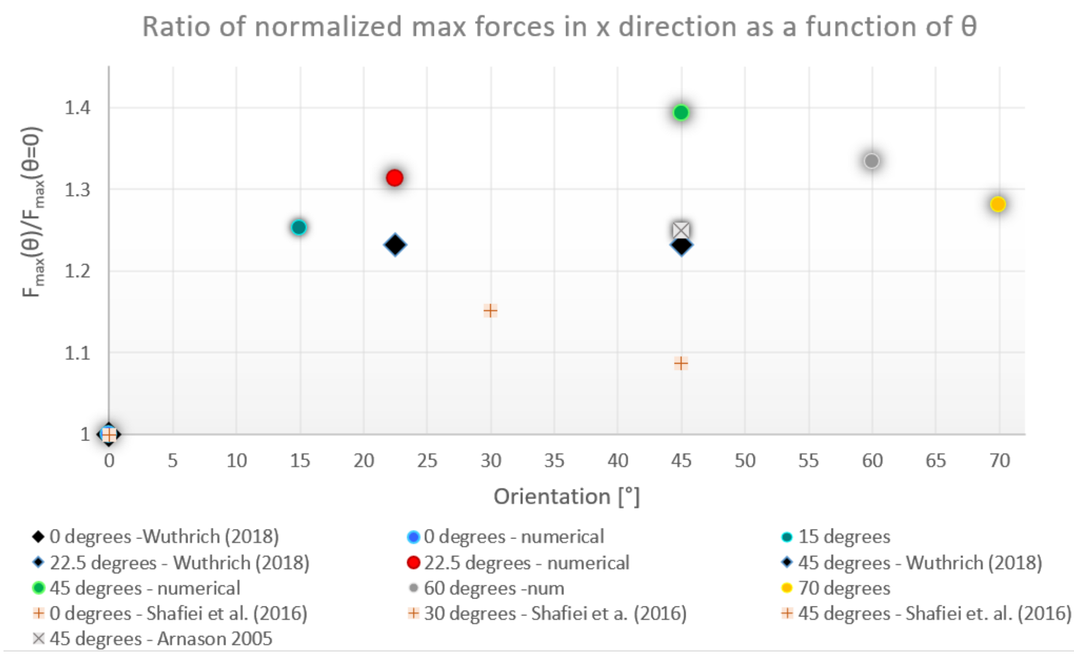

Figure 5.16: Ratio of maximum force for each rotated configuration divided by the max force for $\theta = 0°$, as a function of the angle θ.

Comparing the numerical results of the two figures, 5.16 and 5.15, the behavior between the forces and the blockage ratio, as a function of the angle of rotation, are highly correlated since the curves are following the same trend with respect to the angle of rotation of the building.

The following table collects all the results for the maximum forces for both experimental and numerical results, in the x and y directions for the hydrodynamic part therefore for $t > 8s$, Table 5.2. Collecting all the results together, the effect of the blockage ratio is again obvious. The maximum forces are recorded for the rectangular structure, where the blockage ratio is much higher due to the different shape of the building, and then follows the 45° orientation, where the maximum blockage ratio occurs between the rotates tested cases of the impervious, square building. For the second case where the angle of rotation is kept the same at 45° and the blockage ratio reduced, the total force is significantly reduced, as well. From the same table 5.2, the collected data for the maximum forces per unit width show that even though the total load increases with the angle of rotation with respect to the flow direction, the loads are distributed in larger surface, therefore per unit meter the load is maximum for the frontal square case. The forces per meter for the rotated configurations reduce due to the larger surface which faces the flow. However, for the angle variations of $15 \leq \theta \leq 70°$ the differences are not significant. Lastly, for the case of 45° and the smallest blockage ratio the force per meter drops, showing the lowest load/m. The smallest the blockage ratio, the largest the area that the water can flow around the structure, thus the accumulation of water upstream reduces, leading to generally lower forces acting on the structure.

Angles - Shapes	**Experimental results**		**Numerical results**		
	$F_{x,max}$ [N]	$F_{y,max}$ [N]	$F_{x,max}$ [N]	$\frac{F_{x,max}}{B}$ [N/m]	$F_{y,max}$ [N]
square for 0°	241.21	14.28	228.68	$\boxed{\mathbf{917.20}}$	4.10
square for 15°	-	-	286.30	786.53	19.89
square for 22.5°	264.04	56.96	300.33	765.20	50.28
square for 45°	243.09	26.16	$\boxed{318.71}$	765.38	15.97
second case: 45°	-	-	303.22	**717.22**	13.36
60°	-	-	304.88	743.62	22.52
70°	-	-	292.69	760.24	23.25
rectangular	-	-	**783.4**	**1305.67**	3.85

Table 5.2: Table presenting the maximum forces in x and y directions for both numerical and experimental results and for all the tested cases.

5.5.3. Resistance coefficient - angle of rotation

Another way of proving that the hydrodynamic load is reduced for the rotated configurations is by checking the resistance coefficient. The experimental relation for the resistance coefficient, taking into account the hydrodynamic - drag force and the hydrostatic force (total horizontal load in x direction) is defined as [87]:

$$c_R = \frac{2 \cdot F_x}{\rho \cdot B \cdot h \cdot u^2} \tag{5.11}$$

Where, F_x is the horizontal force, ρ is the density of the water, herein is equal to 1000 kg/m^3, B is the projected building's width to the direction of the flow, h is the wave height and u is the depth-averaged flow velocity.

Combining the experimental equation with the numerical results, an approximation of the resistance coefficient is achieved. Then, the maximum value of the resistance coefficient for each building configuration is normalized by the C_D of the frontal building to the direction of the flow, Figure 5.17. The frontal building has the highest resistance coefficient, and as it goes closer to 45° the drag coefficient drops. For angles close to each other, due to symmetry as well, the ratios are almost identical, θ = 15°, 22.5°, and 70°. The blockage ratio is also important for the drag coefficient. For the case in which the angle remains stable at 45° (b case, pink triangle), and the blockage ratio reduces due to the increase of the channel's width, the resistance coefficient reduces to almost 8% further than for the case of higher blockage ratio (45°, green circle), Figure 5.17).

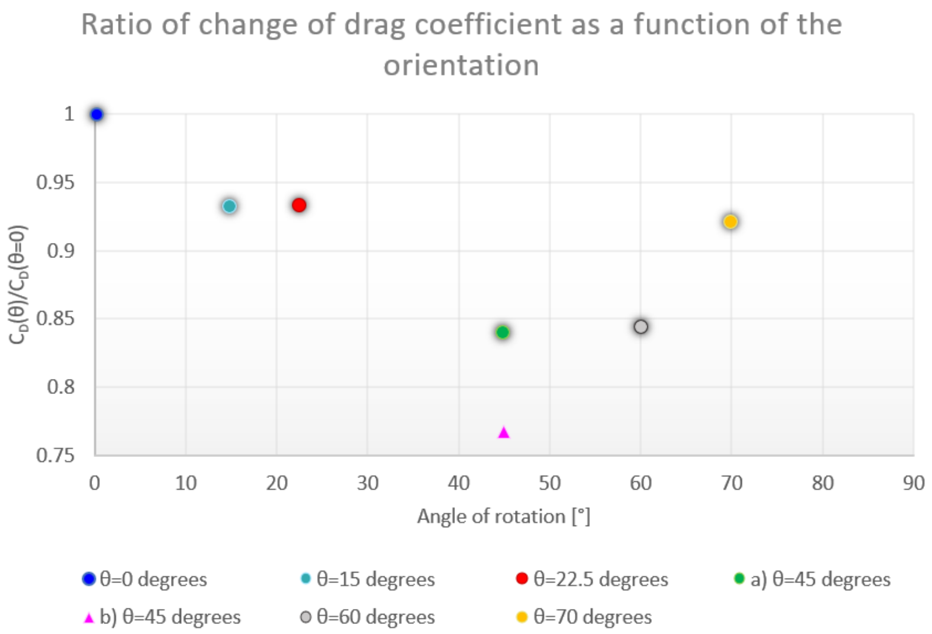

Figure 5.17: The effect of the angle of rotation on the resistance coefficient. Results are normalized by using the c_R value for the frontal impervious configuration.

6 Discussion

In this section, the derived results of the present research, which are analyzed in the previous two chapters, are discussed, addressing some observations and remarks that may affect the validity and the application of the numerical simulation. Moreover, the applied mathematical model and the effect of the assumptions on the numerical results are reviewed.

6.1. Assumptions of the Numerical Model

Unsteady flows are characterized by high complexity which is not fully understood yet. The approach of this research is to provide a practical solution that assists in analyzing and modeling the behavior of the unsteady flow around buildings. Simplifications were used for the functionality of the model, and these influenced the accuracy of the physical process. Some of the potential discrepancies are specified below.

The 2D model

An extensive literature review, for both physical and numerical studies, was accomplished to specify the gaps in the approximations and to determine the optimum way to approach the problem. From the previous research, the most popular and most common technique to simulate fluid problems is the CFD codes using Finite Volume Methods (FVM). However, finite volume methods are often inaccurate and diffusive, when dealing with wave propagation and structural elements. Furthermore, the solution to the boundaries is not well defined, and therefore, a reconstruction method is required in order to be useful. Taking the latter into account, the approach that is used in this thesis is the Discontinuous Galerkin Finite Element Method (DGFEM). The differences between the two methodologies exist mainly in the modeling approach, and FEM has proven to deal better with complex geometries and combinations of fluid-structure interactions.

The two-dimensional shallow water assumption is used for the representation of the unsteady flow in the channel. The wavelength of the generated waves is much longer than the averaged depth, and as a result, the long-period waves behave as shallow-water waves. Besides reducing computational time and cost, the results accurately replicate the flow around the building. However, among other discrepancies in the results, a delay was recorded in the arrival time, which might have been caused due to the coarse time and space resolution of the 2D domain. Furthermore, the 2D representation adds some limitations to the building configurations that can be tested, including building with openings.

Set-up of water elevation and bed surface

For the simulation, the water depth was estimated as a constant function in time, which depends on the mean free surface component, and a free surface perturbation component. The topographical height was assumed to be horizontal, although varied morphological features characterize typical coastal regions. This simplification reduces the computational time of the model but leads to inaccuracies too.

Building assumptions

Since the 2D representation is considered, the building is assumed to be free-standing, without foundation.

The structure is considered sufficiently rigid and deformations were not taken into consideration. The system is studied as a whole, and the elastic deformations and the structural response of the individual elements (for instance walls) are not examined. This assumption simplifies the analysis, by reducing the unknown parameters, and excluding local effects from the loads acting on the building.

6.2. Discussion on the Results

Validation tests
Some features have to be mentioned here, which also may limit the range of comparability. Two different experimental setups were used for the validation. In the case of the first experiment, a dam-break wave was generated for both physical and numerical simulation, and a structure was not taken into consideration. The experimental data successfully validated the numerical results, proving the numerical model's efficacy to simulate the dam-break flow, in the absence of the structure.

For the second validation test, more inconsistencies were noticeable. The laboratory set-up was generating tsunami-like waves through the vertical release technique of a specific amount of water, while the numerical simulation replicates the release of a stored volume by a dam failure, using the same volume. Due to different setups, between experiment and simulation, results deviate, especially for the duration of the hydrodynamic phase. Specifically, using the same volume of water as in the laboratory's upper reservoir, the water wasn't sufficient to retain the same duration of the quasi-steady phase. Therefore, a higher volume of water was used upstream of the dam to identify the hydrodynamic part with higher accuracy. It should be highlighted that the experimental results proved that the vertical release technique was in accordance with a dam failure [86]. The discrepancies here mean that further validation of the numerical technique should be executed. Despite these issues, the general behavior of the fluid-structure interactions (FSI) is captured well, especially upstream of the building, and insights are gained regarding the behavior of the fluid around the structure and the parameters of influence.

Water elevations & Velocities
Upstream of the building, Figure 5.5: In general, water elevations upstream of the building's location are increased by approximately 47% compared to the flow in an absence of an impervious building in the domain. Two points are considered Prob1 and Prob2, which coincide with the US5 and US7, respectively, from the experiment. At the arrival of the bore at the measuring points, the impulse water elevation is higher since the shock wave, produced by the dam-break simulation, behaves more impulsive than the vertical release technique, where the water level difference reduces with the course of time. Another difference, revealed from the comparison, is that for the numerical results at the closest upstream measuring point to the structure, the impulse phase does not capture the run-up on the building walls, and therefore, the values are recorded much lower (Prob2 fixed point). These discrepancies decreased with the rotation due to the reduction of the run-up. The rotation facilitates the flow around the building instead of blocking it, as for the 0° orientation, where the wall is placed perpendicularly to the flow direction. With an angle of 45, the run-up is minor at the upstream side of the walls. The difference in the flow pattern, caused by the rotation of the structure, reduces the water levels upstream, increases the velocities, and in general, results in a modified loading process.

Lateral side of the building, Figure 5.10: The prob4, corresponding to the experimental data captured by US4, is placed halfway between the lateral side of the frontal, square building and the side wall of the channel. The hydrodynamic phase is captured accurately for the 0° orientation of the building, but the water elevation results start to deviate significantly from the experimental ones for the rotated configurations. An underestimation of the water levels is captured, which increases significantly with the orientation of the building. Most likely, the observed differences have to do with the reflected wave that happens in the experiment at the outflow boundary. Due to higher velocities downstream of the rotated configurations a higher reflected wave is expected, and thus, a higher water level downstream of the building. On the contrary, reflection is avoided in the numerical domain.

Shadow zone - downstream of the building, Figure 5.7: Both water elevations and velocities were reduced by 50% and more on the downstream side of the buildings, throughout the course of time. The impervious building is responsible for disturbance in the flow and therefore, turbulence fluctuations. The rotated configurations of the impervious building with respect to the flow direction generated different streamline patterns compared to the impervious vertical frontal wall to the flow ($\theta = 0°$), and results showed a reduction of the turbulence at the mixing layer behind the structure. Furthermore, from Figure 5.8, a qualitative representation of the reduction of the shadow zone with the increase of the rotation from 0° to 45° is depicted. The most favorable case is the 45° as the symmetric separation of the flow contributes to the smoother flow pattern around the building. The wavefront is split in two and ejected sideways upon impact against the structure. When the angle increases further to the angle of 45°, then the separation zone behind the structure increases again, and consequently, the drag forces, caused by the turbulence. For the positioning of the building with $\theta = 0°$, the flow separates easily, amplifying the schematization of the separating area, and the pressure drag is significantly high for this specific configuration. Concluding, the angle of attack with respect to the structure has a large influence on the separation of the flow and consequently, on the dynamics of the flow pattern.

Forces

When the wave arrives at the building, lower horizontal forces in the x direction were recorded for an increase in orientation, until 45°, during the initial time of the impact. The frontal angle is facing the flow, leading to flow separation on the upstream side. The most favorable case is the 45°, where the separation follows a symmetrical pattern leading to the lowest impulse load. However, in the hydrodynamic phase of the load-plateau area in the graphs, the blockage ratio determines the behavior of the total load, leading to an increase in the forces with respect to the orientation. The higher the blockage ratio, the higher the total horizontal loads in the x direction. Plotting the time history of the forces per unit width though, the $\frac{Forces}{m}$ decreased with the angle of rotation until symmetry occurs (45). So, despite the fact that the total loads are higher for the rotated configurations, the blockage ratio is also higher, and therefore, the forces are distributed on a larger surface, leading to a better performance of the structure.

Drag coefficient

A combination of the experimental, empirical equation for estimating the resistance coefficient and the numerical results in time leads to the same conclusion: Orientation decreases the resistance coefficient meaning lower hydrodynamic loads until 45°, and then the further increase in the angle θ has a mirror effect due to the symmetry.

7 Conclusions & Recommendations

7.1. Conclusions

The computational model proposes a simplified method to deal with the complexity of the unsteady flows around impervious buildings. The time history of the water elevation and the averaged velocity field over the depth is programmed to be derived at 4 fixed points around the structure, and the stresses at the surfaces of the structure to estimate the horizontal forces acting on the building. The model was validated with data from Buitelaar (2022) [12] and the experiment of Wüthrich (2018) [86] and the results proved to be overestimated by the numerical model but generally in good agreement. Further building configurations were tested with the model to provide valuable conclusions about the orientation and the shape of the building in the impact of the unsteady flows on the structures. In this chapter, the conclusions that are drawn from the research are summarized. The thesis focused on the main research question:

"How can the numerical tools be used to model, validate, and implement our current knowledge on the loading process of unsteady flows acting on a rigid structure with different geometric configurations?"

The conclusions about the main research question are derived by answering the four supportive sub-questions, and they summarize the findings of the present project.

7.1.1. Numerical model

How can the shallow water equations be modeled to generate a dam-break wave in a domain where an impervious building is considered?

The approach that is used in this thesis is the Discontinuous Galerkin Finite Element Method (DGFEM). Finite elements have flexibility when it comes to discretization. There is no need for reconstruction or interpolation of the solution. The combination of structural elements with fluid propagation proved to be more easily applicable using FEM compared to the other techniques, such as the finite volume method (FVM).

The depth-averaged, two-dimensional shallow water equations, utilizing FEM schemes, were modeled to reproduce the hydraulic response of a dam break wave, against an isolated impermeable structure, considering different geometric configurations. According to the setup of the physical experiments, the initial and boundary conditions were defined, and the variables of the simulation were calculated to be inserted as inputs in the model. A sensitivity analysis was conducted for the optimum value of the variables, and a mesh and time refinement analysis to identify the balance between the required discretization, combined with the less computational cost.

The major challenge in the numerical simulation was to deal with the multi-scale phenomena that accompany such inflows. Discretization of time and space was not sufficient for the unsteady flow which was generated by the dam failure. Dam break waves are shock waves and they created discontinuities, especially close to the boundaries. Moreover, large-scale flows (vortices) are imposed on the main flow as a secondary flow, especially in the area behind the structure. Thus, a turbulent model is deemed necessary to deal with the complexity of the flow interactions. To fix these discontinuities in the fluid field, an LES turbulence model is constructed. The stabilization terms of the turbulence model were achieved to filter the equations, excluding the smallest scale phenomena, which are the most computationally expensive to be resolved. Large eddy phenomena are only captured, and a stable solution is ensured.

This simplified numerical model can provide the base for approaching unsteady flows acting on a built environment. However, some inaccuracies have to be resolved to achieve higher validation of the results. For instance, a significant lack of the numerical model is that it does not account for air entrainment in the solution. It was proved experimentally, that a strong aerated roller during the propagation of the bore increases the turbulence significantly and changes the dynamics of the wave. Therefore, the observed overestimation of the forces it is likely to occur due to this limitation of the simulation.

7.1.2. Validation of the numerical model

Does the comparison between numerical results and physical data ensure the accuracy, reliability, and validity of the simulated dam-break flow?

Model validation is a mandatory step to evaluate whether the obtained results are reliable or further processing of the code is required, regarding the terms of the equations, the boundary and initial conditions, or/and the input parameters. To assess the precision and stability of the numerical scheme, two physical experiments were used for validation.

The first experiment, which also models the dam-break wave in the laboratory, proved that the unsteady flow is replicated with good agreement by the numerical simulation. The second experiment used the vertical release technique for the generation of tsunami-like waves around the structure. Comparing the results of the dam failure model with the experimental ones, some deviations were observed. Considering the discrepancies in the numerical results compared to the experimental ones, that are already discussed in the previous chapter, it is concluded that three are the main reasons that trigger them:

1. The different techniques for the generation of the unsteady flow around the building. Despite the fact that the experimental research was proved to follow similar behavior to a dam-break wave, this Thesis showed more discrepancies throughout the validation process.

2. The different outflow boundary condition seems to be the main reason for the lower water levels at the downstream side of the building. In the experiment, a sill is placed at the outflow, which causes reflection and increases the water levels downstream of the impervious building. For the frontal building configuration, the water levels at the lateral sides were not so underestimated. However, as the rotation increased the recorded differences increased, too. This can be justified by the effect of orientation in lowering the run-up water levels on the upstream building surface, and increasing the flow velocities. This leads to higher reflected waves at the outflow of the experiment domain, and therefore, higher increased depths downstream of the structure, compared to the numerical results that reflection is avoided completely at the outflow boundary by the extension of the domain.

3. The air contribution due to the aerated front bore is not captured by the model, and this additional turbulence caused by the air entraintment could be another parameter that lead to the overestimation of the loads.

7.1.3. Frontal impact of dam-break flow on the buildings

How does the front face of the considered structure experience the horizontal loads that are generated by the unsteady flow of the dam-break wave?

The forces are derived by integrating the induced stresses at the wet surface of the walls of the impervious building for each configuration, and three components compose the total horizontal force in the x and y directions: the shear, the volumetric, and the hydrostatic term, with the latter one providing the highest contribution to the total load. The forces in the y direction are computed much lower than the aligned forces to the flow. Therefore, the research focused mainly on the x direction.

Regarding the precision of the results, the forces are overestimated with respect to the experimental data. And the overestimation increases with orientation. The reasoning behind these inconsistencies is triggered by the underestimation of the water elevation downstream of the building, which also increases with the orientation until 45°. Furthermore, the model is not accounting for air entraintment and this could be an additional reasoning to the overestimation of the loads. Despite the discrepancies, the code is then tested for more building configurations with different orientations and shapes to investigate the behavior of the force curves for the different building orientations and blockage ratios.

In the impulse phase, the separation of the flow determines the behavior of the forces. The highest force in the x-direction is estimated for the vertical configurations: rectangular and square shapes with 0° angle of orientation. As the angle increases, the separation of the flow occurs at the upstream side and the velocities increase, water elevations reduce, leading to a drop in the impulse load. The symmetrical case of 45° rotation is the most favorable producing the lowest total impulse force in the x direction.

At the hydrodynamic phase, the blockage ratio seems to rule the loads in the x direction. The highest the blockage ratio of the building, the highest the total force in the horizontal x direction. Another evidence of the blockage influence is the second case of the 45° that has been tested. Keeping the most favorable angle of rotation ($theta = 45°$) for the flow around the building and reducing the blockage ratio to achieve an equal ratio with the building with no rotation ($\theta = 0°$), a reduction of 8.5% is achieved for the total horizontal forces in the x-direction.

What is more, normalizing the total forces by the projected width for each orientation, the loads per meter are less for the rotated cases. In this way, the concept of building orientation can be used for better distribution of the horizontal loads, and thus, better structure behavior for interactions with highly unsteady flows.

7.1.4. Effect of structure's orientation

How does the orientation of the structure affect the loading process?

The rotation of the building, although increasing the blockage ratio, led to better hydrodynamic performance, for all configurations, and thus, safer vertical shelters. The rotation influenced the force behavior differently over time, during the phase that the wave interacted with the structure, Figure 5.13.

With oriented buildings, the process of separation of the flow is facilitated. The impact reduces when the wave arrives at the rotated configurations. Generally, the highest loads are recorded at the impulsive phase. Hence, the achieved reduction of the maximum force load at the initial phase of the loading process with the angle of rotation is significant for the building's safety. The highest reduction is achieved for the symmetrical case of the 45°, where a 19.2% reduction is achieved compared to the maximum loads for the structure with 0° orientation. Symmetry plays a crucial role in the reduction of the loads at the 45° angle of rotation, and this is the reason why this angle shows the lowest loads per meter width compared to all the testes cases. Additional to this, the results from $0° \leq \theta \leq 45°$ and from $45° \leq \theta \leq 90°$ behave the same.

Another defined effect of when the angle of the sides of the structure starts facing the flow is that the velocities are increased, and a smoother flow pattern is attained. This change in the velocity field leads to a significant reduction in the separation zone behind the structure and the turbulence on the downstream side. Additionally, the orientation around the vertical axis of the impervious building within the flow increased the blockage ratio, responsible for an increase in horizontal forces in the hydrodynamic phase. The water elevations though are reduced upstream because the loads are distributed to a larger surface (larger projected widths). Meaning two different things that lead to a better structural response to the loading process:

- The forces per meter width are lower with an increase in the angle of rotation. Thus, the structure deals better even if the total loads are higher. This increase in the total loads does not overshadow the general beneficial interactions of the rotated building with the flow.

- The cantilever arm of the forces is lower at the building wall, due to the lower derived water elevations. Forces are acting at the wet surface of the building and since these water levels reduce with the increased angle until 45° the cantilever arm is lower too, reducing the tilting moments and the danger of overturning.

Overall, the orientation of the impervious structure leads to the conclusion that can contribute to a safer and more resilient structure. Especially, the symmetrical placement to the flow $\theta = 45°$ showed the highest reduction in water elevations and loads and a smooth flow pattern. The velocities, though, increased upstream and the scour-hole evolution needs to be studied further, for the stability of the buildings.

7.2. Recommendations

Although encouraging, the results generate the need for further improvement of the numerical simulation and future work. This section includes some recommendations, based on the discussion and the conclusions derived from the current study.

- At first, it is highly recommended to improve the validation of the model by implementing the outflow boundary for the numerical simulation. If a sill is located at the same distance, instead of the infinitely long domain which was considered for the present research, this would simulate more closely the experimental data. To do so, a three-dimensional representation will be a more accurate approach to deal with the elevation change in the topography due to the existence of the sill.
- A 3D numerical representation will be also beneficial to model the increased turbulence at the frontal part of the wave, due to the aerated front. The effect of aeration remains difficult to assess and further implementations are necessary.
- The coarse time and space discretization may be responsible for the constant delay in the arrival of the bore, at each measuring point. The coarse resolution seems to lose some information and hence, a finer mesh could be assessed, or higher order for the basis functions could give a higher order of accuracy for a given mesh. Therefore, further investigation is needed to deal with the present time delay in the arrival of the bore at the fixed points around the building.
- The code should be implemented to be tested for different water depth profiles, and the morphology of the bed should be considered. Moreover, the bed surface is assumed to be smooth which is again not a realistic representation of an actual situation. A smooth bed leads to a quasi-steady response at the hydrodynamic phase, which is not the case for rough seabeds. The effect of the bottom friction in the numerical simulation is vital to be evaluated since the real tsunamis are not acting on a smooth horizontal bed surface, like the examined one in the current research. Higher roughness bed values can also be tested. In this way, the influence of the roughness on the behavior of the flow can be captured, and the degree of contribution to the increase of the drag force.
- Furthermore, the role of additional horizontal forces, such as debris, should be investigated to estimate the change of the impact on the structure.
- The change in flow pattern around the building due to the rotation generates also the query about the scour hole schematization. The scour in front of the building and at the lateral sides is not so easily predictable. The wall is not blocking the flow anymore, like in the case of the perpendicular placement of the building with respect to the flow direction, where the velocities upstream lead to settlement due to the zero-enforced velocities at the walls. For the rotated case the flow rate increases at the upstream side and research should be executed to investigate how the scour-hole schematization is developed, and what is the effect on the stability of the building.
- Finally, further research can be conducted, regarding the numerical application of the FE model. In this research, the focus was given to the influence of the orientation on the load impact on impervious structures, and the parameters that contribute to the interactions with the flow field. The simulation can be used as the foundation to extend it further with some required implementations. For instance,

complicated geometries, or openings in the surface of the building can also be investigated. Additionally, more buildings can be considered at the same time in the domain to simulate better a built environment, and then, the research can focus on how the interacted structures affect the flow. In particular, frontal buildings can provide protection for certain locations within the built environment and create shelter for adjacent structures. For the current research, the rectangular shape, with the largest length facing the flow, ensured zero velocities behind the structure and can be beneficial for buildings placed in this zone. This would be attractive research to provide an economically beneficial option for the communities of the world, prone to unsteady flows.

Bibliography

[1] V. Aizinger and C. Dawson. A discontinuous galerkin method for two-dimensional flow and transport in shallow water. *Advances in Water Resources*, 25(1):67–84, 2002.

[2] V R. Ambati and O. Bokhove. Space–time discontinuous galerkin finite element method for shallow water flows. *Journal of computational and applied mathematics*, 204(2):452–462, 2007.

[3] H. Arnason. *Interactions between an incident bore and a free-standing coastal structure.* University of Washington, 2005.

[4] N. Asadollahi, I. Nistor, and A. Mohammadian. Numerical investigation of tsunami bore effects on structures, part i: drag coefficients. *Natural Hazards*, 96(1):285–309, 2019.

[5] Cx K Batchelor and GK Batchelor. *An introduction to fluid dynamics.* Cambridge university press, 2000.

[6] J. A. Battjes and R. J. Labeur. *Unsteady flow in open channels.* Cambridge University Press, 2017.

[7] T. Belytschko, W. K. Liu, B. Moran, and K. Elkhodary. *Nonlinear finite elements for continua and structures.* John wiley & sons, 2014.

[8] J. Bezanson, S. Karpinski, V. B. Shah, and A. Edelman. Julia: A fast dynamic language for technical computing. *arXiv preprint arXiv:1209.5145*, 2012.

[9] J. Bosboom and M. JF. Stive. *Coastal dynamics I: lectures notes CIE4305.* 2012.

[10] B. Bratz. Hydrodynamic loading of dutch terraced houses due to flood actions using computational fluid dynamics. 2019.

[11] M. J. Briggs, H. Yeh, and D. T. Cox. Physical modeling of tsunami waves. In *Handbook of coastal and ocean engineering*, pages 1073–1105. World Scientific, 2010.

[12] M. Buitelaar. Effect of bed roughness on the hydrodynamic properties of dam-break waves. 2022.

[13] JM Burgerscentrum. Finite element methods for the incompressible navier-stokes equations. 2015.

[14] O. Castro-Orgaz and H. Chanson. Ritter's dry-bed dam-break flows: Positive and negative wave dynamics. *Environmental Fluid Mechanics*, 17(4):665–694, 2017.

[15] H. Chanson. *Hydraulics of open channel flow.* Elsevier, 2004.

[16] H. Chanson. Analytical solution of dam break wave with flow resistance: application to tsunami surges. In *31st IAHR Congress 2005: Water Engineering for the Future, Choices and Challenges*, pages 3341–3353. Citeseer, 2005.

[17] H. Chanson. Tsunami surges on dry coastal plains: Application of dam break wave equations. *Coastal engineering journal*, 48(04):355–370, 2006.

[18] H. Chanson. Application of the method of characteristics to the dam break wave problem. *Journal of Hydraulic Research*, 47(1):41–49, 2009.

[19] G. Chock. The asce 7 tsunami loads and effects design standard for the united states. In *Handbook of coastal disaster mitigation for engineers and planners*, pages 437–460. Elsevier, 2015.

[20] R. Codina, S. Badia, J. Baiges, and J. Principe. Variational multiscale methods in computational fluid dynamics. *Encyclopedia of computational mechanics*, pages 1–28, 2018.

[21] O. Colomés. Lecture notes: Introduction to Finite Elements, Module 4, OE44090, 2020.

[22] O. Colomés, S. Badia, R. Codina, and J. Principe. Assessment of variational multiscale models for the large eddy simulation of turbulent incompressible flows. *Computer Methods in Applied Mechanics and Engineering*, 285:32–63, 2015.

[23] O. Colomés, S. Badia, and J. Principe. Mixed finite element methods with convection stabilization for the large eddy simulation of incompressible turbulent flows. *Computer methods in applied mechanics and engineering*, 304:294–318, 2016.

[24] O. Colomés, A. Main, L. Nouveau, and G. Scovazzi. A weighted shifted boundary method for free surface flow problems. *Journal of Computational Physics*, 424:109837, 2021.

[25] J. Cotela-Dalmau, R. Rossi, and E. Oñate. A fic-based stabilized finite element formulation for turbulent flows. *Computer Methods in Applied Mechanics and Engineering*, 315:607–631, 2017.

[26] M. Alberti D. McKenzie, L. Madowo and A. Dewan. Over 300 killed after flooding washed away roads, destroyed homes in south africa, 2022. URL https://edition.cnn.com/2022/04/13/africa/south-africa-rain-floods-climate-intl/index.html.

[27] M. A. Day. The no-slip condition of fluid dynamics. *Erkenntnis*, 33(3):285–296, 1990.

[28] A. I. Delis and I. K. Nikolos. Shallow water equations in hydraulics: Modeling, numerics and applications, 2021.

[29] United States. Federal Emergency Management Agency. Mitigation Directorate. *Coastal Construction Manual: Principles and practices of planning, siting, designing, constructing, and maintaining residential buildings in coastal areas*. Federal Emergency Management Agency, Mitigation Directorate, 2000.

[30] V. Dolejší, M. Feistauer, and C. Schwab. On some aspects of the discontinuous galerkin finite element method for conservation laws. *Mathematics and Computers in Simulation*, 61(3-6):333–346, 2003.

[31] R. F. Dressler. *Hydraulic resistance effect upon the dam-break functions*, volume 49. National Bureau of Standards Washington, DC, 1952.

[32] A. Ern and JL. Guermond. *Theory and practice of finite elements*, volume 159. Springer, 2004.

[33] DW Made for minds. Brazil: Heavy rain and landslides leave 34 dead, 2022.

[34] P. Gancarski. Model evaluation protocol, Accessed: 2021-03-12. URL https://github.com/windbench/WEMEP/blob/master/mep/mep.rst.

[35] C. Geuzaine and J-F Remacle. Gmsh: A 3-d finite element mesh generator with built-in pre-and post-processing facilities. *International journal for numerical methods in engineering*, 79(11):1309–1331, 2009.

[36] V. Guinot and B. Cappelaere. Sensitivity analysis of 2d steady-state shallow water flow. application to free surface flow model calibration. *Advances in Water Resources*, 32(4):540–560, 2009.

[37] LTT Hien and N. Van Chien. Investigate impact force of dam break flow against structures by both 2d and 3d numerical simulations. water 2021, 13, 344, 2021.

[38] E. Houghton, P. Carpenter, S. H. Collicott, and D. T. Valentine. Chapter 1—basic concepts and definitions. *Aerodynamics for Engineering Students, 7th ed.; Butterworth-Heinemann: Oxford, UK*, pages 1–86, 2017.

[39] M. Ishiwatari. Climate change adaptation in flood risk management through utilizing datasets produced by supercomputer. 2010.

[40] C. T. Jacobs and M. D. Piggott. Firedrake-fluids v0. 1: numerical modelling of shallow water flows using an automated solution framework. *Geoscientific Model Development*, 8(3):533–547, 2015.

[41] Subhash C Jain. *Open-channel flow*. John Wiley & Sons, 2000.

[42] C. Jones. *Coastal Construction Manual: Principles and Practices of Planning, Siting, Designing, Constructing and Maintaining Residential Buildings in Coastal Areas*. Diane Publishing, 2001.

[43] E. J. Kubatko, S. Bunya, C. Dawson, J. J. Westerink, and C. Mirabito. A performance comparison of continuous and discontinuous finite element shallow water models. *Journal of Scientific Computing*, 40(1): 315–339, 2009.

[44] I. V. Lencina. *Comparison between 1D and 2D models to analyze the dam break wave using the FEM method and the shallow water equations.* Architecture and the Built Envornment, Royal Institute of Technology, 2007.

[45] D. Liang. Evaluating shallow water assumptions in dam-break flows. In *Proceedings of the Institution of Civil Engineers-Water Management*, volume 163, pages 227–237. Thomas Telford Ltd, 2010.

[46] L. Liu, J. Sun, B. Lin, and L. Lu. Building performance in dam-break flow–an experimental study. *Urban Water Journal*, 15(3):251–258, 2018.

[47] A. Louka. Gridap - shallow water simulation, 2022. URL https://github.com/annlouka/GridapShallowWater.jl.

[48] L. Lundgren and A. C. Jonsson. Assessment of social vulnerability: a literature review of vulnerability related to climate change and natural hazards. 2012.

[49] J. Lyons. More damaging flooding, 2022 sea level rise technical report, 2022. URL https://edition.cnn.com/2022/04/13/africa/south-africa-rain-floods-climate-intl/index.html.

[50] A. Main and G. Scovazzi. The shifted boundary method for embedded domain computations. part i: Poisson and stokes problems. *Journal of Computational Physics*, 372:972–995, 2018.

[51] C. Marschik, W. Roland, B. Loew-Baselli, and G. Steinbichler. Application of hybrid modeling in polymer processing. In *Proceedings of the ANTEC*, 2020.

[52] M. Masó, I. De-Pouplana, and E. Oñate. A fic-fem procedure for the shallow water equations over partially wet domains. *Computer Methods in Applied Mechanics and Engineering*, 389:114362, 2022.

[53] Pacific Tsunami Museum. Tsunami characteristics.

[54] Y. Nakano. Structural design requirements for tsunami evacuation buildings in japan, 2011.

[55] J. Newton, CD Paci, and A. Ogden. Climate change and natural hazards in northern canada: integrating indigenous perspectives with government policy. *Mitigation of Natural Hazards and Disasters: International Perspectives*, pages 209–239, 2005.

[56] D. Nishiura, D. Wüthrich, M. Furuichi, S. Nomura, M. Pfister, and G. De Cesare. Numerical approach in the study of tsunami-like waves and comparison with experimental data. In *The 29th International Ocean and Polar Engineering Conference*. OnePetro, 2019.

[57] Y. Nouri, I. Nistor, D. Palermo, and A. Cornett. Experimental investigation of tsunami impact on free standing structures. *Coastal Engineering Journal*, 52(1):43–70, 2010.

[58] Encyclopedia of Mathematics. Gibbs phenomenon., 2011. URL http://encyclopediaofmath.org/index.php?title=Gibbs_phenomenon&oldid=47097.

[59] Bureau of Reclammation. Teton dam history, 2020.

[60] ParaView. Unleash the power of paraview, 2022. URL https://www.paraview.org/.

[61] J. Pedlosky. The stress tensor for a fluid and the navier stokes equations. *Fluid Dynamics of the Atmosphere and Ocean*, page 32, 2014.

[62] L Pengzhi. Numerical modeling of water waves. 2008.

[63] A. Prasetyo, T. Yasuda, T. Miyashita, and N. Mori. Physical modeling and numerical analysis of tsunami inundation in a coastal city. *Frontiers in built environment*, 5:46, 2019.

[64] G. Pringgana, L. S. Cunningham, and B. D. Rogers. Influence of orientation and arrangement of structures on tsunami impact forces: numerical investigation with smoothed particle hydrodynamics. *Journal of Waterway, Port, Coastal, and Ocean Engineering*, 147(3):04021006, 2021.

[65] ZX Qi, I. Eames, and E. R. Johnson. Force acting on a square cylinder fixed in a free-surface channel flow. *Journal of Fluid Mechanics*, 756:716–727, 2014.

[66] M Quecedo, M Pastor, MI Herreros, JA F. Merodo, and Q. Zhang. Comparison of two mathematical models for solving the dam break problem using the fem method. *Computer Methods in Applied Mechanics and Engineering*, 194(36-38):3984–4005, 2005.

[67] J. N. Reddy. *Introduction to the finite element method*. McGraw-Hill Education, 2019.

[68] AJHM Reniers and JA Battjes. A laboratory study of longshore currents over barred and non-barred beaches. *Coastal Engineering*, 30(1-2):1–21, 1997.

[69] J. Rentschler, M. Salhab, and B. Jafino. Flood exposure and poverty in 188 countries. 2021.

[70] A. Ritter. Die fortpflanzung der wasserwellen. *Zeitschrift des Vereines Deutscher Ingenieure*, 36(33):947–954, 1892.

[71] DM Robb and JA Vasquez. Numerical simulation of dam-break flows using depth-averaged hydrodynamic and three-dimensional cfd models. In *Proceeding of Canadian Society for Civil Engineering 22nd Hydrotechnical Conference*, pages 27–36, 2015.

[72] G. J Schiereck. *Introduction to bed, bank and shore protection*. CRC Press, 2017.

[73] D. Schwanenberg and J. Köngeter. A discontinuous galerkin method for the shallow water equations with source terms. In *Discontinuous Galerkin Methods*, pages 419–424. Springer, 2000.

[74] S. Shafiei, B. W. Melville, and A. Y. Shamseldin. Experimental investigation of tsunami bore impact force and pressure on a square prism. *Coastal Engineering*, 110:1–16, 2016.

[75] J. Smagorinsky. General circulation experiments with the primitive equations: I. the basic experiment. *Monthly weather review*, 91(3):99–164, 1963.

[76] S. Soares-Frazão and Y. Zech. Experimental study of dam-break flow against an isolated obstacle. *Journal of Hydraulic Research*, 45(sup1):27–36, 2007.

[77] S. Soares-Frazão and Y. Zech. Dam-break flow through an idealised city. *Journal of Hydraulic Research*, 46(5):648–658, 2008.

[78] L. Souza, TP Chanekar, and GS Pandit. Case study and forensic investigation of failure of dam above kedarnath. *International society of soil*, 2019.

[79] H. Taisuke. Quality management systems-process validation guidance, January 2004. URL https://www.imdrf.org/sites/default/files/docs/ghtf/final/sg3/technical-docs/ghtf-sg3-n99-10-2004-qms-process-guidance-04010.pdf.

[80] L. Tan and V. H. Chu. Lauber and hager's dam-break wave data for numerical model validation. *Journal of hydraulic research*, 47(4):524–528, 2009.

[81] W. Tan. *Shallow water hydrodynamics: Mathematical theory and numerical solution for a two-dimensional system of shallow-water equations*. Elsevier, 1992.

[82] G. Testa, D. Zuccala, F. Alcrudo, J. Mulet, and S. Soares-Frazão. Flash flood flow experiment in a simplified urban district. *Journal of Hydraulic Research*, 45(sup1):37–44, 2007.

[83] U.S. Climate Resilience Toolkit. Disaster resilience: A national imperative.

[84] G. N. Wells. The finite element method: An introduction. *Lecture notes for CT5142*, 2011.

[85] G. B. Whitham. The effects of hydraulic resistance in the dam-break problem. *Proceedings of the Royal Society of London. Series A. Mathematical and Physical Sciences*, 227(1170):399–407, 1955.

[86] D. Wüthrich. Extreme hydrodynamic impact onto buildings. Technical report, EPFL, 2018.

[87] D. Wüthrich, M. Pfister, I. Nistor, and A. J. Schleiss. Experimental study on the hydrodynamic impact of tsunami-like waves against impervious free-standing buildings. *Coastal Engineering Journal*, 60(2): 180–199, 2018.

[88] D. Wüthrich, M. Pfister, I. Nistor, and A. J. Schleiss. Experimental study on forces exerted on buildings with openings due to extreme hydrodynamic events. *Coastal Engineering*, 140:72–86, 2018.

[89] D. Wüthrich, D. Nishiura, S. Nomura, M/ Furuichi, and G. Pfister, M.and De Cesare. Experimental and numerical study on wave-impact on buildings. In *E-proceedings of the 38th IAHR World Congress*, number CONF, pages 6047–6056, 2019.

[90] D. Wüthrich, M. Pfister, I. Nistor, and A. J. Schleiss. Effect of building overtopping on induced loads during extreme hydrodynamic events. *Journal of Hydraulic Research*, 58(2):289–304, 2020.

[91] D. Wüthrich, M. Pfister, and A. J. Schleiss. Forces on buildings with openings and orientation in a steady post-tsunami free-surface flow. *Coastal Engineering*, 161:103753, 2020.

[92] H. Yeh, A. R. Barbosa, H. Ko, and J. G. Cawley. Tsunami loadings on structures: Review and analysis. *Coastal Engineering Proceedings*, 1(34):4, 2014.

[93] C. Ylla Arbos. Influence of building orientation on the hydrodynamic impact of water waves on buildings with openings. Technical report, 2018.

[94] C. Ylla Arbos, D. Wüthrich, M. Pfister, A. Schleiss, et al. Wave impact on oriented impervious buildings. In *Proceedings of the 5th IAHR Europe Congress*, number CONF, pages 791–792. Aronne Armanini and Elena Nucci, 2018.

[95] A.l J. Zubaidah. India and bangladesh floods displace millions and kill dozens, 2022. URL https://www.bbc.com/news/world-asia-india-61670666.

A

Numerical code

- Discrete model

  The system of the continuity and momentum equations are rewritten in the weak formulation and inserted into the numerical model. Initially, the discrete model of the domain Ω is required to be constructed. The generation and the discretization of the computational domain were accomplished in the GMSH software, which generates an .msh type of file. The resolution should be high enough to obtain an accurate representation of the propagation of the dam-break wave. Specifically, the resolution is split into two different areas. The one closer to the structure area has higher resolution not only because the area of interest is located there but also because the flow is much more turbulent due to the interactions of the flow with the building's boundaries. Hence, the outer domain (far away from the structure) is divided by an element size of $0.1m$, while the inner domain (close to the structure) has a finer mesh with an element size of $0.03m$, see Figure A.1. To load the model in Julia the .msh file is converted to a .json data file by using the function "CartesianDiscreteModel".

Figure A.1: Mesh resolution of the 2D domain with the impermeable structure

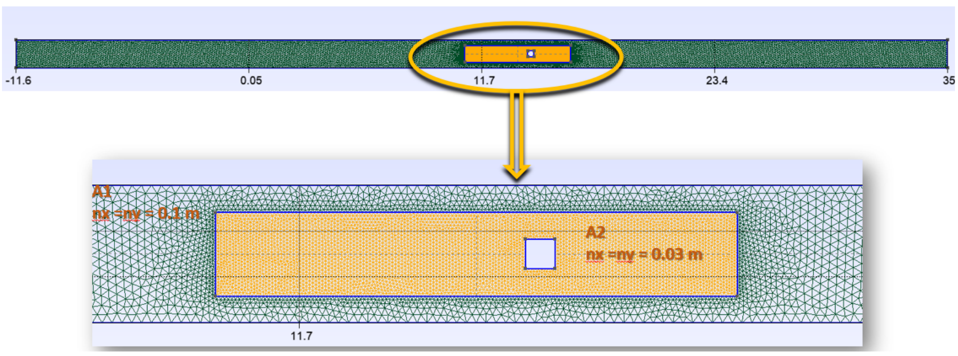


```
        #Domain
to_json_file(GmshDiscreteModel("trial_str.msh"),"trial_str.json")
T= DiscreteModelFromFile("trial_str.json")
writevtk(T,"trial_str")
```

- Triangulation and Boundaries of the domain

  Before creating the Finite Element space, the triangulations of each of the sub-domains are defined to separate the fluid and the solid parts of the domain. The corresponding boundaries are stored and labeled using the function "tags".

```
   #Triangulations
 Ω = Interior(T)
 Γ = Boundary(T,tags="outflow")
 Γw = Boundary(T,tags="walls")
 Γ = Boundary(T,tags="sides")
 Λ = Skeleton(Ω)

# Parameters & Boundaries
g = 9.81
H = 0.03
h(x,t) = (0.63-H) * (x[1]<=0)
h(t::Real) = x->h(x,t)
u(x,t) = VectorValue(0.0,0.0)
u(t::Real) = x->u(x,t)

ν = 1.0e-6 #3.225
cD = 0.0127
g = 9.81
h(x,t) = 0.001
h(t) = x -> h(x,t)
I = TensorValue(1.0,0.0,0.0,1.0)

 rho = 1000
μ_s = 1.0e-3
```

- FE spaces

  It follows the definition of the finite element space for the velocity and the water elevation fields. The velocity field reference FE is defined by a two-dimensional "VectorValue" type, Lagrangian reference FE of order 1 (linear function). The reference FE for the water elevation is a scalar value type and it is given by constant values, order of 0. For the velocity FE spaces the "TestFESpace" function and the "TransientTrialFESpace" function are used with the corresponding discrete model, using the velocity reference FE $reffe_u$ and conformity: L1, linear Lagrangian shape functions. Finally, the separated test and trial FE spaces are combined by using the "MultiFieldFESpace" and the "TransientMultiFieldFESpace", respectively.

```
    order = 1
refFE = ReferenceFE(lagrangian,VectorValue{2,Float64},order)
refFE = ReferenceFE(lagrangian,Float64,order-1)
V = TestFESpace(Ω,refFE,dirichlet_tags="walls")
V = TestFESpace(Ω,refFE;conformity=:L2)
U = TransientTrialFESpace(V,u)
U = TransientTrialFESpace(V)
Y = MultiFieldFESpace([V,V])
X = TransientMultiFieldFESpace([U,U])
```

- Numerical integration

  Once we have all the triangulations, we can generate the quadrature rules to be applied to each domain. This will be generated by calling the "Measure" function. Given a triangulation and an integration degree, it returns the Lebesgue integral measure $d\Omega$.

```
    # Measure (quadrature rules for numeric integration)
dΩ = Measure(Ω,2*order)
dΓ = Measure(Γ,2*order)
dΛ = Measure(Λ,2*order)
dΓw = Measure(Γw,2*order)
dΓ = Measure(Γ,2*order)
```

```
# Normal vectors to the boundaries
nΓ = get_normal_vector(Γ)
nΛ = get_normal_vector(Λ)
nΓw = get_normal_vector(Γw)
nΓ = get_normal_vector(Γ)
```

- Mesh

  For the mesh-size generation, the "lazy map" generic function is used for the scaling, and it represents the operation of walking over all cells and evaluating the fields, cell by cell, as a whole (cell-wise implementation), (Tutorial 13-Gridap).

```
# Mesh size
Δx = lazy_map(dx->dx^(1/2),get_cell_measure(Ω))
ΔxΛ = 0.2#get_cell_measure(Λ)
```

- Stabilized parameters
  To reduce the fictitious oscillations that are generated, the weak formulation is being processed by stabilization terms, regarding the research of Oriol (2020) [21]. For the stabilized parameters three algorithmic constants are used c_1. c_2 and c_3. The terms are considered to be the dissipative terms of τ_u and τ_h. An increase in c_1 reduces both terms leading to a less dissipation method, but increasing the c_2 value increases the dissipation. According to the analysis conducted in the paper Colomés et al. [22], the values of $c_1 = 12$, $c_2 = 2$ and $c_3 = 1$ are chosen. The constant c_2 has the largest influence in the terms and the higher its value the less dissipative the method is, hence, the energy at small scales is not properly dissipated, Colomés et al. [22].

```
# Stabilization
c = 12.0; c = 2.0; c = 1.0
global u = interpolate_everywhere(u(0.0),U(0.0))
global h = interpolate_everywhere(h(0.0),U(0.0))
#meas(u) = (uu)#meas(u)
dmeasu(u,du) = (udu)/((uu)+1e-14)
R(u,h) = t(h) + (h)'u + (h+H)*(u)
R(u,h) = t(u) + (u)'u + g*(h) + cD/(h+H)*u*(meas(u))
dR(u,h,du,dh) = (dh)u + dh*(u) + (h)du + (h+H)*(du)
dR(u,h,du,dh) = (du)'u + + (u)'du + g*(dh)
                + cD/(h+H)*du*(meas(u)) + cD/(h+H)*u*(dmeasu(u,du))
                - cD/(h*h+1e-14)*u*dh*(meas(u))
L(v,w) = - (v)'u - g*(w)
L(v,w) = - (w)u - H*(v)
τ(a,h) = 1.0 / (c*ν/(Δx.^2) + c*a/Δx + c*cD*g*a/(h+1e-14))
τ(a,h) = Δx.^2/(c*τ(a,h))
dτdu(a,h,da) = - τ(a,h)*τ(a,h) * (c/Δx + c*cD*g/(h+1e-14))*da
dτdh(a,h,dh) = τ(a,h)*τ(a,h) * c*cD*g*a/(h*h+1e-14)*dh
dτdu(a,h,da) = τ(a,h)/τ(a,h)*dτdu(a,h,da)
dτdh(a,h,dh) = τ(a,h)/τ(a,h)*dτdh(a,h,dh)
γ = 1.0/ΔxΛ
```

- Governing equations

  At this point, the weak residual and its corresponding Jacobian is presented. Function res(t,(u,h),(v,w) is the one representing the integrand of the weak residual. The argument in the residual (u, h) stands for the unknown field of the velocity and the water elevation, while the part of (v,w) stands for the test functions. The same holds for the jacobian function. In the end, the nonlinear FE problem is constructed by the "FEoperator", which is the type that represents a general nonlinear FE problem in Gridap. The constructor takes the functions representing the weak residual and Jacobian, and the test and trial spaces.

```
     # Weak form
  # Residual
  res(t,(u,h),(v,w)) = (
    t(h)*w - (h+H)*u(w) +
    (t(u) + (u)'u + cD*((meas(u))/(h+H))*u)  v - g*h*(v) +
    ν*( ((u)+(u)') - 2/3*(u)*I )  (v) -
    R(u,h) * ((τ(measu,h))*L(v,w)) -
    R(u,h)  ((τ(measu,h))*L(v,w)) )dΩ +
    ( g*(h(t)*(vnΓ)) + h(t)*(unΓ)*w + H*(unΓ)*w )dΓ +
   #  ( g*h*(vnΓw) )dΓw +
    ( g*h*(vnΓ) )dΓ+
    ( mean((h+H)*u)jump(w*nΛ) + γ*jump(h*nΛ)jump(w*nΛ) +
       mean(g*h)*jump(vnΛ) )dΛ

    # Jacobian
  jac(t,(u,h),(du,dh),(v,w)) = (
    - ((h+H)*du + dh*u)(w) +
    ((du)'u + (u)'du + cD*((meas(u))/(h+H))*du
    + cD/(h+H)*u*(dmeasu(u,du)) - cD*((meas(u))/(h+H))*u*dh )  v - g*dh*(v) +
    ν*( ((du)+(du)') - 2/3*(du)*I )  (v) -
    dR(u,h,du,dh) * ((τ(measu,h))*L(v,w)) -
    dR(u,h,du,dh)  ((τ(measu,h))*L(v,w)) -
    R(u,h) * ((dτdu(measu,h,dmeasu(u,du)) + dτdh(measu,h,dh))*L(v,w)) -
    R(u,h)  ((dτdu(measu,h,dmeasu(u,du)) + dτdh(measu,h,dh))*L(v,w)) )dΩ +
    ( h(t)*(dunΓ)*w + H*(dunΓ)*w )dΓ +
   #  ( g*dh*(vnΓw) )dΓw +
    ( g*dh*(vnΓ) )dΓ +
    ( mean(dh*u)jump(w*nΛ) + mean((h+H)*du)jump(w*nΛ) +
       γ*jump(dh*nΛ)jump(w*nΛ) +
       mean(g*dh)*jump(vnΛ) )dΛ

  jac_t(t,(u,h),(dut,dht),(v,w)) = (
    dht * w +
    dut  v -
    dht * (τ(measu,h)*L(v,w)) -
    dut  (τ(measu,h)*L(v,w)) )dΩ

  op = TransientFEOperator(res,jac,jac_t,X,Y)

#Cauchy stress tensor
 sigma(u,h) = μ_s* ((u)+(u)') - μ_s*2/3*(u)*I - g*rho*(h+H)*I
```

- Nonlinear Solver

  The final phase is to find the approximated solution of the system for the unknown fields of velocity and water elevation. In Gridap, nonlinear FE problems can be solved by the function of "FESolver". Note that the NLSolver function used above internally calls the nlsolve function of the NLsolve package with the provided keyword arguments. Thus, one can use any of the nonlinear methods available via the function nlsolve to solve the nonlinear FE problem. Here, we have selected a "ThetaMethod" method with a back-tracking line-search from the LineSearches package. The set of water elevations, velocities, and time steps is called in the form of CVS file, and additionally, the visualization is accomplished by writing the computed solution "writevtk". Also, the stresses at the boundary of the impervious building are derived and integrated for the computation of the total horizontal forces and each of the force terms separately.

```
    # Solver
nls = NLSolver(show_trace=true,linesearch=BackTracking(),iterations=10)
```

```
t = 0.0
T = 20
Δt= 0.04
ode_scheme = ThetaMethod(nls, Δt, 0.5)
x = interpolate_everywhere([u(0.0),h(0.0)],X(0.0))
x = solve(ode_scheme,op,x,t,T)

probe1 = VectorValue(13.35,0.99)
u_probe1 = Float64[]
h_probe1 = Float64[]
t_probe1 = Float64[]

probe2 = VectorValue(13.85,0.99)
u_probe2 = Float64[]
h_probe2 = Float64[]

probe3 = VectorValue(14.45,0.99)
u_probe3 = Float64[]
h_probe3 = Float64[]

probe4 = VectorValue(14.15,1.591)
u_probe4 = Float64[]
h_probe4 = Float64[]

sigma_prob1 = Float64[]
FD_t = Float64[]
FL_t = Float64[]

FD1_t = Float64[]
FL1_t = Float64[]

FD2_t = Float64[]
FL2_t = Float64[]

FD3_t = Float64[]
FL3_t = Float64[]


output_files = paraview_collection("rotation45", append=false) do pvd
 for (x,t) in x
   println("Time: $t")
   u, h = x

#Horizontal forces (hydrodynamic & hydrostatic part)
  FD, FL =  sum( ( nΓw   sigma(u,h)  (h))dΓw  )

push!(u_probe1,meas(u(probe1)))
   push!(h_probe1,h(probe1)+H)
   push!(t_probe1,t)

   push!(u_probe2,meas(u(probe2)))
   push!(h_probe2,h(probe2)+H)

   push!(u_probe3,meas(u(probe3)))
   push!(h_probe3,h(probe3)+H)
```

```
    push!(u_probe4,meas(u(probe4)))
    push!(h_probe4,h(probe4)+H)

    FD1,FL1 = sum((nΓw  (μ_s* ((u)+(u)’) ) * h )dΓw )
    FD2,FL2 = sum((nΓw   (- μ_s*2/3*(u)*I ) * h )dΓw )
    FD3,FL3 = sum((nΓw  ( - g*rho*(h+H)*I ) * h )dΓw )

    pvd[t] = createvtk(Ω,"name of each tested case_$t.vtu",cellfields=["u"=>u,"h"=>h])
    global u, h
    interpolate_everywhere!(u,get_free_dof_values(u),get_dirichlet_dof_values(U(t)),U(t))
    interpolate_everywhere!(h,get_free_dof_values(h),get_dirichlet_dof_values(U(t)),U(t))

  push!(FD_t,FD)
    push!(FL_t,FL)

    push!(FD1_t,FD1)
    push!(FL1_t,FL1)

    push!(FD2_t,FD2)
    push!(FL2_t,FL2)

    push!(FD3_t,FD3)
    push!(FL3_t,FL3)

  end
end

filename_FD = "data_FD"*"_$Δt.csv"
filename_FL = "data_FL"*"_$Δt.csv"

CSV.write(filename_FD,Tables.table(FD_t))
CSV.write(filename_FL,Tables.table(FL_t))

filename_FD1 = "data_FD1"*"_$Δt.csv"
filename_FL1 = "data_FL1"*"_$Δt.csv"

CSV.write(filename_FD1,Tables.table(FD1_t))
CSV.write(filename_FL1,Tables.table(FL1_t))

filename_FD2 = "data_FD2"*"_$Δt.csv"
filename_FL2 = "data_FL2"*"_$Δt.csv"

CSV.write(filename_FD2,Tables.table(FD2_t))
CSV.write(filename_FL2,Tables.table(FL2_t))

filename_FD3 = "data_FD3"*"_$Δt.csv"
filename_FL3 = "data_FL3"*"_$Δt.csv"

CSV.write(filename_FD3,Tables.table(FD3_t))
CSV.write(filename_FL3,Tables.table(FL3_t))

filename_t1 = "data_t1"*"_$Δt.csv"
filename_u1 = "data_u1"*"_$Δt.csv"
filename_h1 = "data_h1"*"_$Δt.csv"
CSV.write(filename_t1,Tables.table(t_probe1))
CSV.write(filename_u1,Tables.table(u_probe1))
```

```
CSV.write(filename_h1,Tables.table(h_probe1))

filename_u2 = "data_u2"*"_$Δt.csv"
filename_h2 = "data_h2"*"_$Δt.csv"
CSV.write(filename_u2,Tables.table(u_probe2))
CSV.write(filename_h2,Tables.table(h_probe2))

filename_u3 = "data_u3"*"_$Δt.csv"
filename_h3 = "data_h3"*"_$Δt.csv"
CSV.write(filename_u3,Tables.table(u_probe3))
CSV.write(filename_h3,Tables.table(h_probe3))

filename_u4 = "data_u4"*"_$Δt.csv"
filename_h4 = "data_h4"*"_$Δt.csv"
CSV.write(filename_u4,Tables.table(u_probe4))
CSV.write(filename_h4,Tables.table(h_probe4))


end
```

B

Mesh & time refinement

Mesh refinement

For the grid discretization, the grid size needs to be specified in order to achieve valid results with the smallest possible computational effort. To achieve this, a time and mesh refinement is carried out. The discretization of the domain is set as follows at the code script. Where α denotes the ratio of $\frac{\text{length of the domain}}{\text{width of the domain}}$ and it is used to specify the grid size.

```
#Domain
x = -8.094
x = 30.0
α = ceil((x-x)/0.4)
 = CartesianDiscreteModel((x,x,0.0,0.4),(α*nx,nx))
labels = get_face_labeling()
add_tag_from_tags!(labels,"outflow",[2,4,8])
add_tag_from_tags!(labels,"walls",[1,3,5,6,7])
```

The x direction (length of the domain) is divided by $\alpha \cdot n_y$ and y direction (width of the domain) by n_y. The values of $n_y = 2,4,8$ are tested, and a first glance at the results shows that the discretization is adequate accurately even for a value of 2 which corresponds to a grid size of 0.2 in the two horizontal directions. Zooming in the different time steps small inconsistencies are denoted at the first seconds that the water elevation increases rapidly with the arrival of the wavefront for $0 < t < 0.5$. Between $n_y = 4$ and $n_y = 8$ differences are not significant, Figure B.1. Thus, $n_y = 4$ is considered sufficient to reduce the computational effort.

n_y	**Grid size**		**Time step**
	Δx [m]	Δy [m]	dt [s]
2	0.2	0.2	0.05
4	0.1	0.1	0.05
8	0.05	0.05	0.05

Table B.1: Numerical spatial and temporal resolution

Figure B.1: Comparison of 3 different mesh sizes for the optimal 2D space resolution.

Time refinement

Time discretization is well-aligned with the spatial grid size. An empirical way to estimate the time step is by using the follow relation:

$$\Delta t = \frac{\Delta x}{u_{max}}$$

Where Δx is the mesh resolution and u_{max} is the maximum velocity. For a grid size of $\Delta x = \Delta y = 0.1m$ the time resolution is computed equal to 0.06s. However, using this time step of 0.06s, slight oscillations are observed at the moment that the water elevation and the averaged velocity peak when it reaches the upstream surface of the building. To avoid these oscillations a time step of 0.05s is used and the time refinement is proven enough to smoothen the response, Figure B.2. Thus, a time step of 0.05s is used and a grid size of $\Delta x = \Delta y = 0.1m$ to derive the numerical results of the 1^{st} experiment.

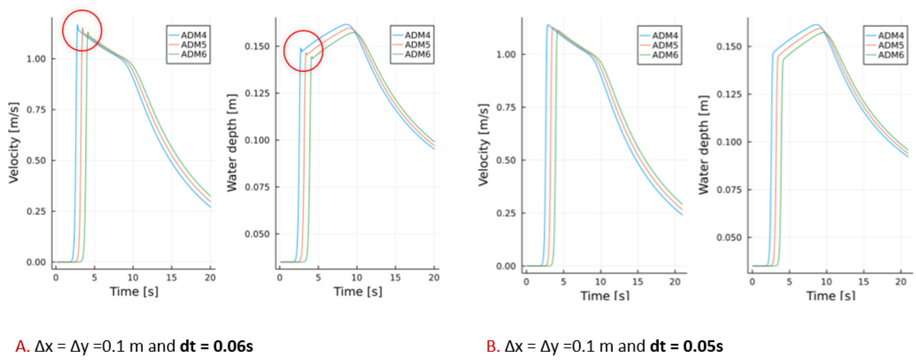

Figure B.2: Time refinement regarding a grid size of 0.1m

C

Sensitivity analysis

Sensitivity analysis is taking place for the optimization of the parameters of friction coefficient, related to the bed material, and kinematic viscosity of the fluid. The purpose of this analysis is to determine their influence on the flow and specify the best fit for the data of the physical experiment.

For the sensitivity analysis of the **friction parameter**, the case with the initial depth of $35mm$ in the channel was used, and five trials of different values and order of magnitude of the friction coefficient are tested to capture the influence of the parameter on the behavior of the water elevation. The trials were accomplished from the following values:

(i) $c_f = 0.0071$, the calculated value of friction for the initial test,

(ii) $c_f = 0.0045$,

(iii) $c_f = 0.001$,

(iv) $c_f = 0.022$,

(v) $c_f = 0.2$,

(vi) $c_f = 0.2$.

Water elevation numerical trials are executed for the different values of friction coefficient. The results are presented below:

(a) Wave propagation at ADM4:

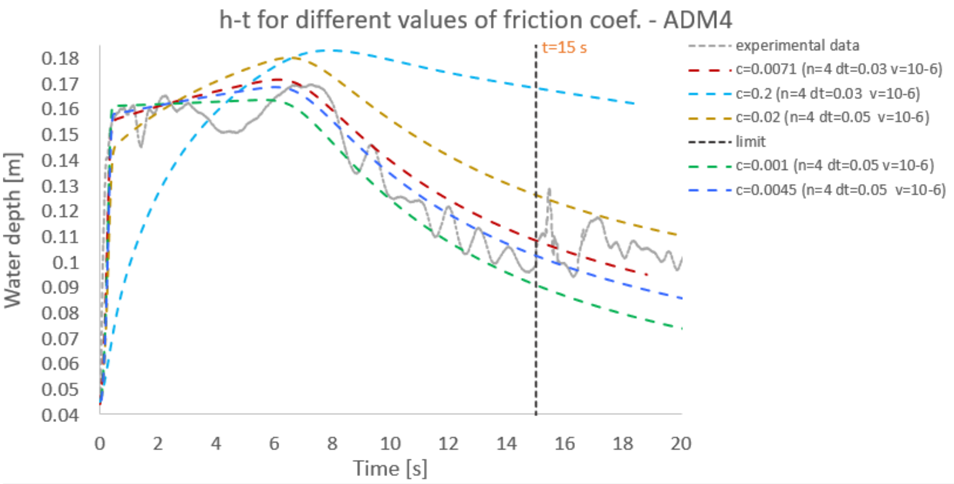

Figure C.1: Sensitivity analysis of friction coefficient at the ADM4 gauge

(b) Wave propagation at ADM5:

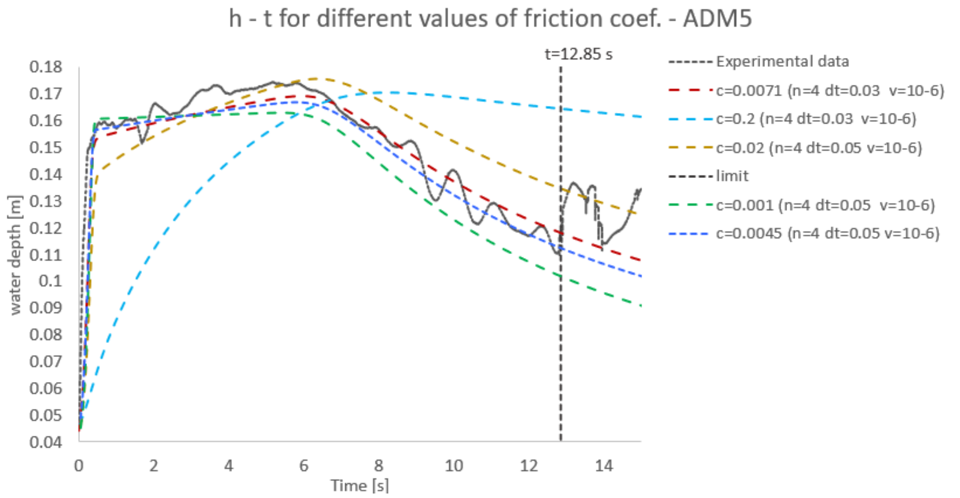

Figure C.2: Sensitivity analysis of friction coefficient at the ADM5 gauge

(c) Wave propagation at ADM6:

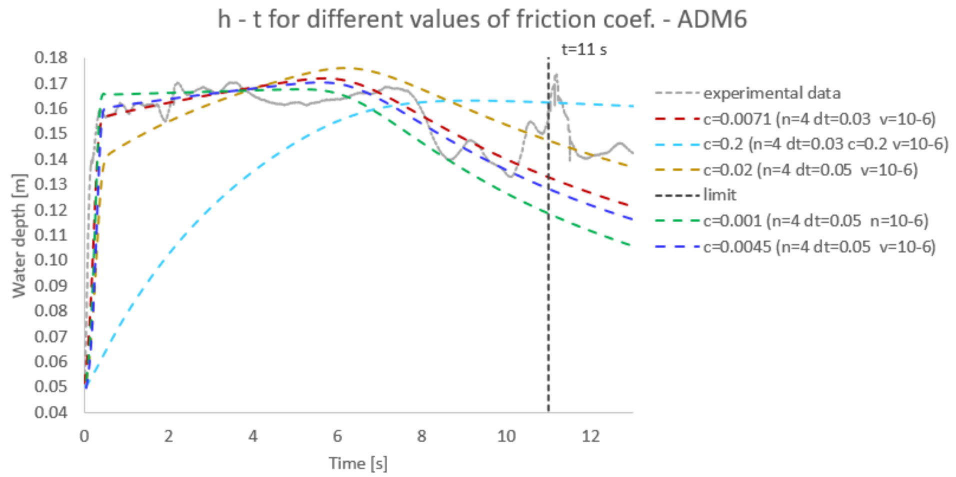

Figure C.3: Sensitivity analysis of friction coefficient at the ADM6 gauge

The results showed that the higher the friction coefficient, the more resistance in the flow, and therefore, a delay is introduced in the initial shock. For very high friction, $c_f = 0.2$, the water depth is lower than the experimental ones, and the results deviate completely from the experimental data, due to the fact that a smooth bed is used for the model, which leads to a friction coefficient of 2 orders of magnitude smaller than this specific, tested value.

For 1^{st} order of magnitude higher friction coefficient ($c_f = 0.02$), than the calculated one for the smooth bed, the water depth is lower in the beginning due to the higher dissipation in the flow. After approximately 4s, the depth value increases even more than the experimental one, due to the conservation of mass.

For lower values of friction coefficient than the computed one, $c_f \leq 0.0071$, the bed is smoother leading to a plateau area, where the values of the water elevation show little or no change with respect to time, for a duration of approximately $6s$. At this time frame, both velocities and water elevation are constant in time, and the assumption of the quasi-steady-state response is valid for this time frame. For higher resistance at the bottom, the solution deviates from the steady-state approach.

The optimum value for the friction term is the computed value, which showed the best agreement with the experimental curve.

To study the behavior of the fluid, regarding the **kinematic viscosity**, 3 different values of viscosity were checked, and the plots with the resulting water elevation compared to the experimental ones are introduced in the Appendix C, for the three different measuring points ADM4, ADM5, and ADM6.

(i) $\nu_t = 10^{-6} \rightarrow$ Kinematic viscosity of water at 20 degrees

(ii) $\nu_t = 1.5 \cdot 10^{-5} \rightarrow$ Kinematic viscosity of air at 20 degrees

(iii) $\nu_t = 3.12 \cdot 10^{-6} \rightarrow$ A slight increase in the kinematic viscosity of water in an effort to consider the air contribution due to the aerated front, which is not included in the simulation. A trial of an increased kinematic viscosity was carried out to check whether the reductions have a positive effect on the results compared to the experimental ones.

Water elevation numerical trials for the different values of kinematic viscosity at the three measuring points:

(a) Wave propagation at ADM4:

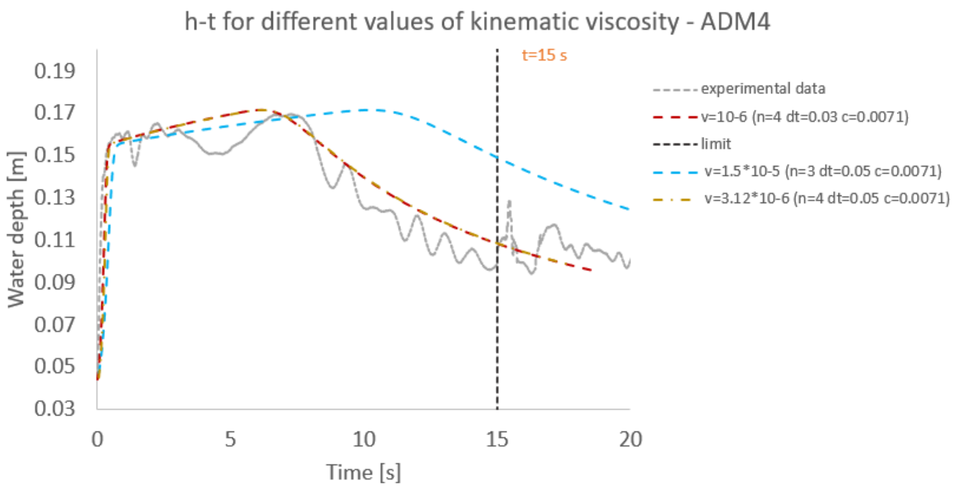

Figure C.4: Sensitivity analysis of kinematic viscosity parameter at the ADM4 gauge.

(b) Wave propagation at ADM5:

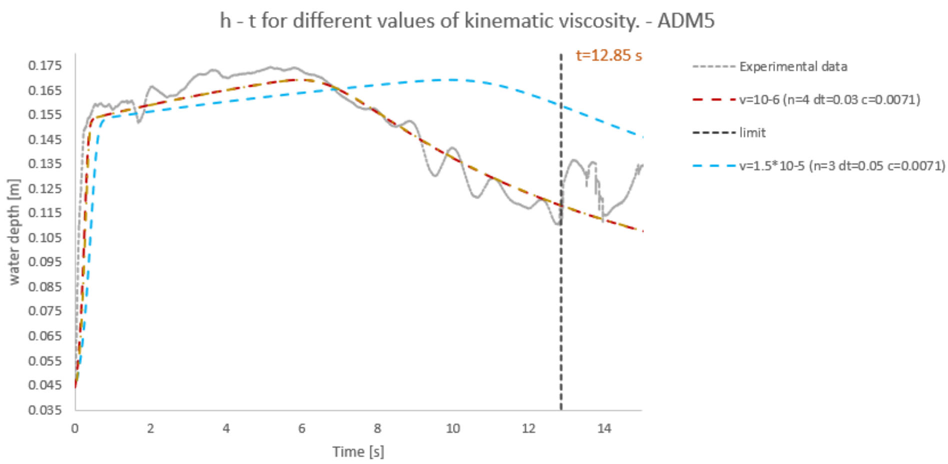

Figure C.5: Sensitivity analysis of kinematic viscosity parameter at the ADM5 gauge.

(c) Wave propagation at ADM6:

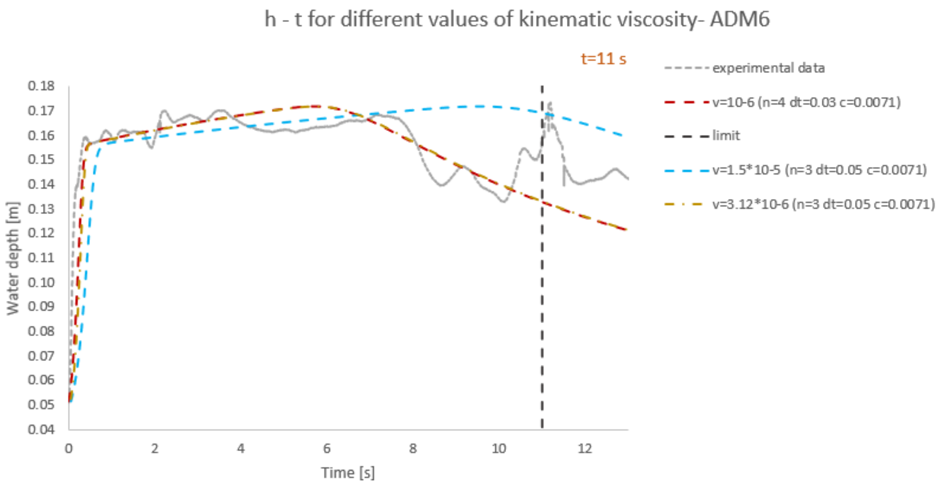

Figure C.6: Sensitivity analysis of kinematic viscosity parameter at the ADM6 gauge

According to the numerical results, the higher kinematic viscosity of the air is also visual in the behavior of the wave height throughout the course of time. The plateau is reached slower due to the higher viscosity and the maximum wave height is some millimeters lower than the ones recorded from the kinematic viscosity of water.

The tested value of $3.12 \cdot 10^{-6} m^2/s$ was used to consider the air entrainment due to the aerated front of the wave that is significant for the wet bed bores. However, the assumption is not an accurate representation of the reality, since the aerated front is a local phenomenon at the front part of the wave and the viscosity term is applied to the general flow conditions. From the graphs of a duration of $20s$, the differences are not noticeable, although zooming into smaller time steps the initial shock is reached slower for the higher viscosity. However, the differences seem to be negligible in the scale of interest. Therefore, the calculations for the simulated results will be continued using the kinematic viscosity of water.

D

Numerical results including a structure for the validation

The derived results include a delay of 0.95 sec compared to the experimental ones.

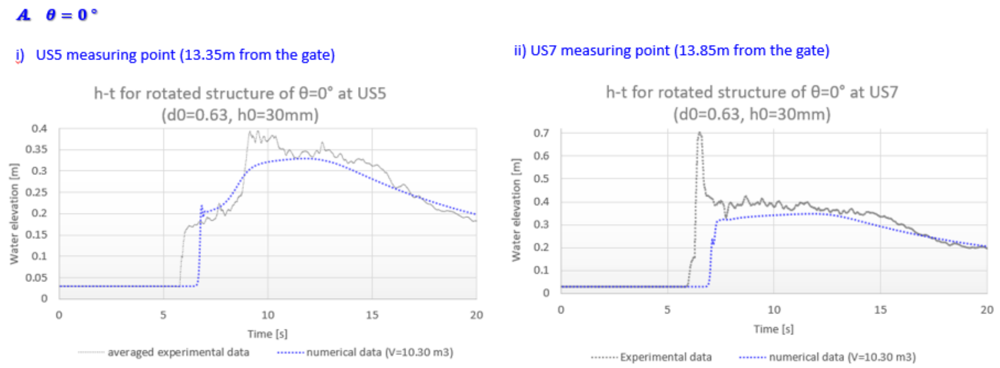

(a) h-t at 13.35 m and 13.85 m for $\theta = 0°$

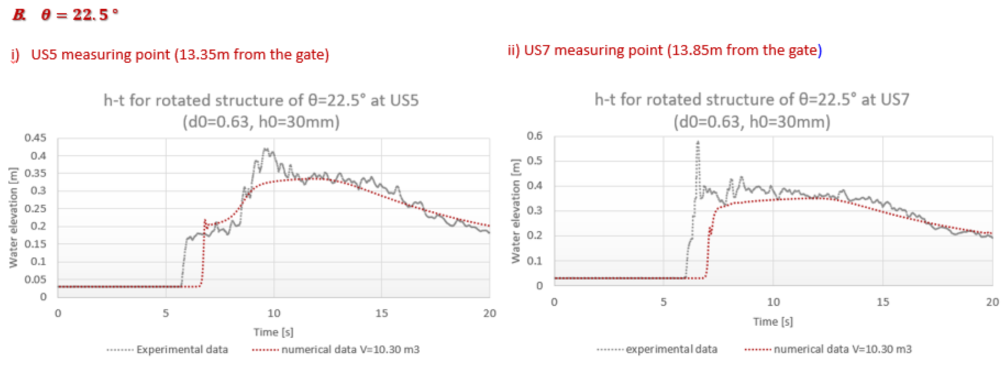

(b) h-t at 13.35 m and 13.85 m for $\theta = 22.5°$

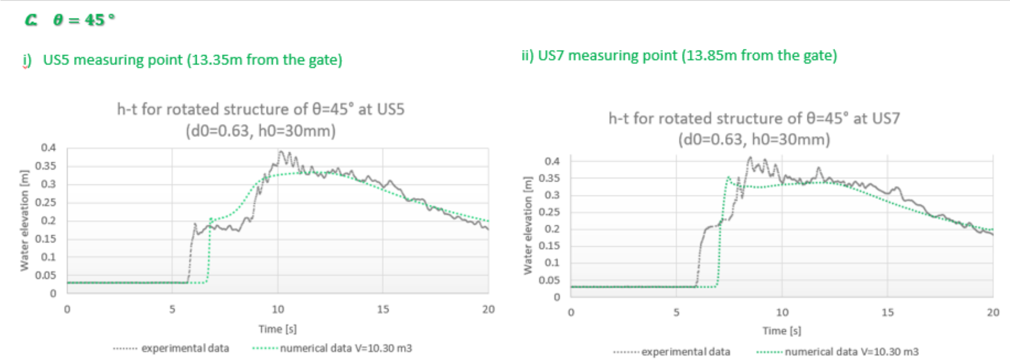

(c) h-t at 13.35 m and 13.85 m for $\theta = 45°$

Figure D.1: Comparison of numerical results with the experimental data derived at the laboratory, for the case of impounded depth of $d_0 = 0.63m$ and initial water depth at the channel of $h_0 = 30mm$, including a building at a distance of 14 m from the dam location. The points of measurement for each orientation are at US5 (13.35m) and at US7 (13.85m), at the upstream side of the building.

E

Roughness values for bottom materials

Material	**Manning value, n** $[m^{-1/3}s]$
PVC, plexiglass	0.01
Glass	0.01
Asbestos cement	0.011
Asphalt	0.016
Concrete - steel forms	0.011
Concrete cement - finished	0.012
Concrete - wooden forms	0.015
Concrete centrifugally spun	0.013
Wood	0.012 - 0.02
Earth smooth	0.018
Earth channel - clean	0.02
Earth channel - gravelly	0.025
Earth channel - weedy	0.030
Earth channel - stony, cobbles	0.035
Galvanized iron	0.016
Gravel, firm	0.023
Natural streams - clean and straight	0.030
Natural streams - major rivers	0.035
Natural streams - slugging with deep pools	0.04
Natural streams - stones and vegetation	0.05 - 0.06
Natural streams - stones and vegetation	0.09
Meadows and pastures	0.035
Meadows and pastures	0.05 - 0.07
Dense forest	0.10

Table E.1: Compiled table from Reniers and Battjes (1997)

F

3D visualization of the water elevation for the tested cases

Meshing 2D	0°	15°	22.5°	i. 45°	ii. 45°	60°	70°	Rectangular
Elements	23422	25666	25726	25054	34838	25850	25688	26274
Nodes	11536	12658	12688	12352	17244	12750	12669	12962

Table F.1: Number of element and nodes of the discretized domain for all the tested cases

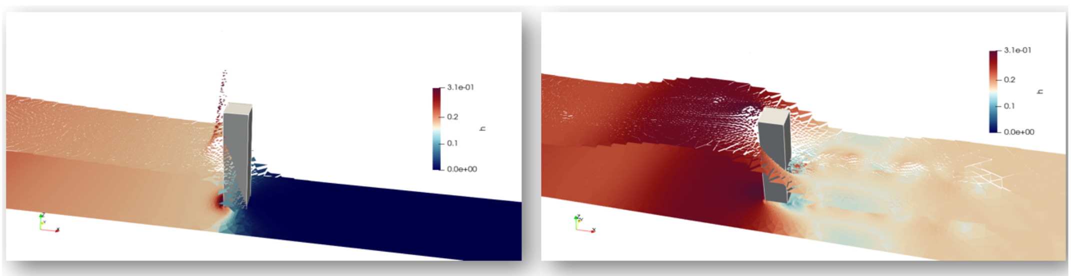

a) θ=0°, t=7.1 s   t=10.6 s

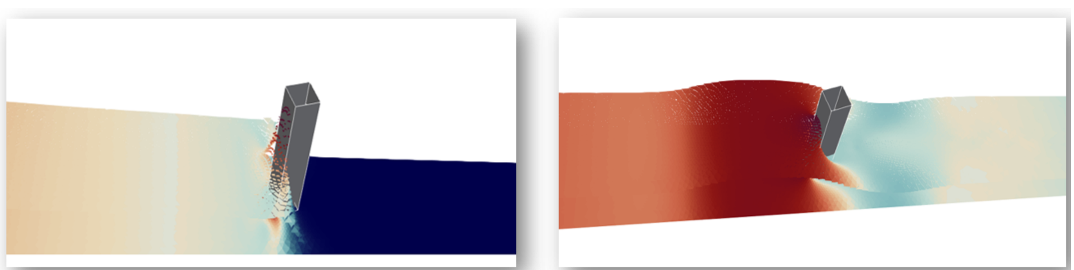

b) θ=15°, t=7.15 s   t=10.6 s

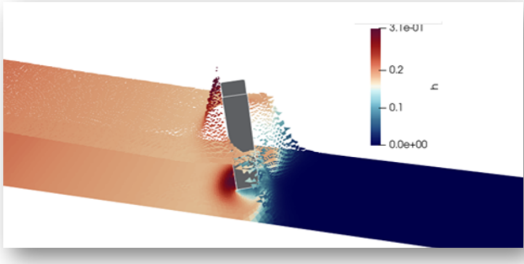

c) θ=22.5°, t=7.367s

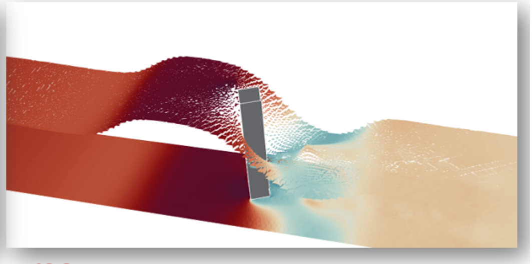

t=10.6 s

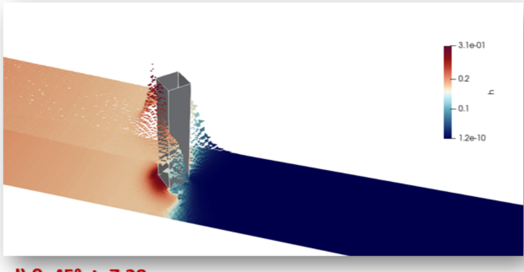

d) θ=45°, t=7.28 s

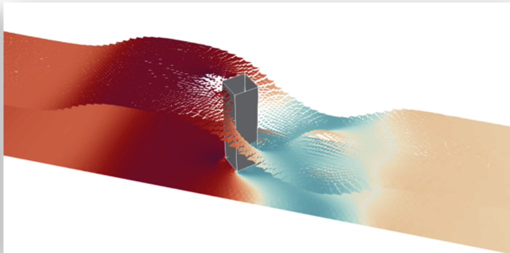

t=10.6 s

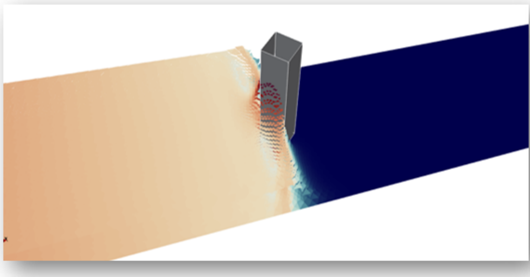

e) θ=45°, case 2, t=7.16 s

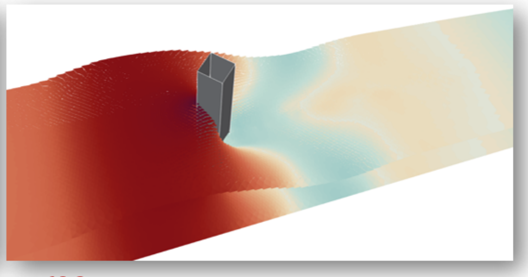

t=10.6 s

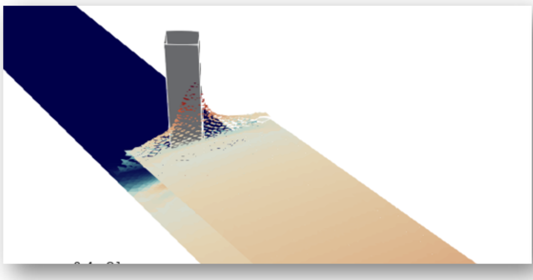

f) θ=60°, t=7.14 s

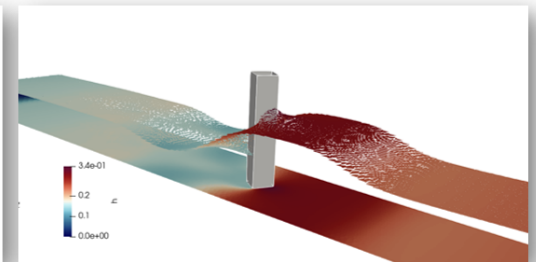

t=10.6 s

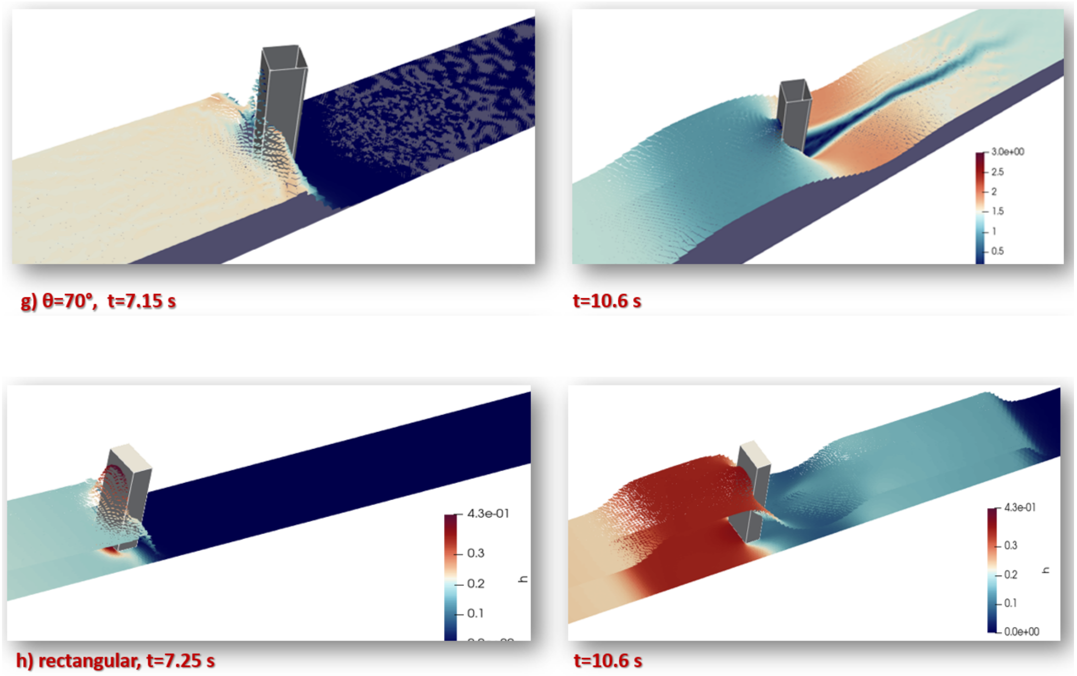

Figure F.1: Visualization of water elevation around the impervious building configurations. Run up reduction with the increase of the blockage ratio.